ABSTRACT

High-Fidelity Simulation of Liquid Atomization in Quiescent Environment and Supersonic Flows

Bo Zhang, Ph.D.

Advisor: Yue Ling, Ph.D.

The atomization of liquid fuel in both quiescent environment and supersonic flows is essential to a wide variety of applications. Since it is challenging to obtain high-level details of the time-dependent, 3D, and chaotic multiphase flow features in experiment, high-fidelity simulation is an important alternative to reveal the complex flow physics involved, such as liquid breakup and shock-interface interaction. The goal of this dissertation is to develop rigorous numerical methods for both incompressible and compressible interfacial multiphase flows, and to investigate liquid jet atomization in both quiescent environment and high-speed gas flows through high-fidelity simulations.

To achieve this goal, simulation is first performed for the breakup and oscillation of a dripping water droplet in quiescent air. The drop formation and dynamics are essential elements of the more complex counterpart, liquid jet atomization. The pinching process plays an important role in initiating the shape oscillation of the drop. The interplay between the shape oscillation and the falling motion induces a complex transient flow inside and outside of the drop. Furthermore, modeling and simulation are conducted to investigate the injection and breakup of a cylindrical gasoline surrogate jet in a quiescent gas under the Engine Combustion Network spray

G conditions. The spray G benchmark was developed to advance the study of gasoline direct injection engines. A momentum-conserving volume-of-fluid (VOF) method is used. To account for the effect of the internal flow in the injector, in particular that the liquid flow at the nozzle inlet is not aligned with the nozzle axis, a finite injection angle is invoked at the inlet. The injection angle is found to have a strong impact on the breakup dynamics and the statistics of the droplets generated. Finally, the study is extended to developing numerical methods for simulation of liquid breakup in a supersonic flow. An All-Mach approach is employed and the advection of conservative variables are conducted consistently with the VOF. To suppress numerical oscillations near discontinuities in the flow, numerical diffusion is introduced based on the Kurganov-Tadmor method. The new method is tested by different compressible multiphase flow problems. The numerical results are validated against theory and experiments and a good agreement is achieved.

High-Fidelity Simulation of Liquid Atomization in Quiescent Environment and Supersonic Flows

by

Bo Zhang, B.E., M.E., M.A.

A Dissertation

Approved by the Department of Mechanical Engineering

_____

Paul Ro, Ph.D., Chairperson

Submitted to the Graduate Faculty of
Baylor University in Partial Fulfillment of the
Requirements for the Degree
of
Doctor of Philosophy

Approved by the Dissertation Committee

_____

Yue Ling, Ph.D., Chairperson

_____

Paul Ro, Ph.D.

_____

Stephen T. McClain, Ph.D.

_____

Jill Klentzman, Ph.D.

_____

Anzhong Wang, Ph.D.

Accepted by the Graduate School
December 2020

_____

J. Larry Lyon, Ph.D., Dean

*Page bearing signatures is kept on file in the Graduate School.*

TABLE OF CONTENTS

LIST OF FIGURES

LIST OF TABLES

# ACKNOWLEDGMENTS

First and foremost the greatest person I would like to express my heartful gratitude to is my insightful and tactful advisor Dr. Yue Ling, without whom I cannot accomplish any research work in my Ph.D. pursuit. He is indeed an expert and genius in instructing, edifying, and encouraging me to conquer the tough times at Baylor. I deeply appreciate all the energy and time he has spent on me. The professional knowledge and the enlightening ideas he has granted to me are the most precious resources I could rely on in my future life. He is not only a wise supervisor but also my spiritual mentor, who sheds light on me during my dark time. In my mind, he is a giant in both knowledge and personality. He is my lifetime close collaborator and precious friend.

I am pretty grateful to Dr. Anzhong Wang for his patience to answer my academic questions and his wisdom to show me how to become a successful scientist. I am extremely obliged to him for teaching me the course Quantum Mechanics for my first year at Baylor, and he showed me how to think logically and critically.

I appreciate the tremendous help I received from my collaborators Dr. Stephάne Zaleski, Dr. Stephάne Popinet, Dr. Guillaume Legros, Dr. An-Bang Wang, and Dr. Pei-Hsun Tsai.

I appreciate the great help I get from Dr. McClain, who taught me Intermediate Fluid Mechanics and Intermediate Heat Transfer. He is a very smart, knowledgeable and humorous professor.

I am pretty grateful to Dr. Jill Klentzman and Dr. Paul Ro for investing so much energy and time as my defense committee members. In particular, Dr. Ro is one of my spiritual mentors.

Many thanks go to the excellent and smart professors Dr. Liang Dong, Dr. Min Pack, Dr. Lulin Jiang, Dr. Yang Li, Dr. Jonathan Hu, and Dr, Xin Wang, who share

their research experiences with me and show me how to make first-class research. I owe Dr. Liang Dong for teaching me Deep Learning.

I would like to thank Dr. Douglas Smith, Dr. David Jack, Dr. Julie A. King, Ms. Julie Williams, Ms. Sara Baker, and Ms. Jodi Branch for their great help in my graduate study.

I own my great thanks to Dr. Faming Gao, Dr. Bo Xu and Dr. Yongjun Tian, who are my great supervisors showing me how to accomplish high-quality research.

I am extremely obliged to my fellow graduate and undergraduate students, Jordon Sakakeeny, Delin Jiang, Taofiqhasan Mahmood, Xiangzhou Jian, Xinxiao Li, Patrick Jaeckle, Thomas Kava, Chris Helms, Bradley Nelson and Armand Shams, with whom I communicate and share ideas.

I appreciate the support and encouragement from my family, relatives and close friends. Especially, I would like to deeply thank my wife, Grace Huang, who loves me so much and accompanies me in those happy and tough times.

# DEDICATION

To my proud and generous motherland P. R. China, from which I developed and matured

To the great U.S., where I received the high-quality graduate study and financial support

To Grace, my virtuous, brilliant, courteous, and pulchritudinous wife, who keeps on encouraging, pacifying, inspiring, and leading me through the darkness

To Amy, Annie, and Ashley, my cherished kids, who bring the fun and sunshine to me

To Genshen and Shuzhen, my beloved parents, who take me to the world and show me the right ways to live and behave

To Jenny, my lovely sister, who teaches me how to play and share

To my supportive relatives and caring friends, without whom my life will not flourish

# CHAPTER ONE

# Introduction

## *1.1 Liquid Atomization*

Atomization is usually referred to as the process for bulk liquids to disintegrate into small droplets. Effective atomization is important to many applications, such as spray cooling, spray painting, agricultural spray, and internal combustion engines.

### *1.1.1 Liquid Atomization in Quiescent Environment*

Atomization can be achieved by injecting liquid into a quiescent environment, such as fuel injection in an internal combustion engine. Effective atomization in quiescent environment typically requires high injection velocity and pressure. For example, in typical diesel engines, the liquid diesel fuel is injected into the quiescent air through an orifice of size about $O(\sim 0.1mm)$ with a high velocity about 489-516 m/s. To push the liquid through the injection nozzle and to reach such a high speed, the upstream pressure can be as high as 1500 bar as specified in the Engine Combustion Network (ECN) Spray A operating condition (Yang *et al.*, 2020).

The atomization of a liquid jet in a quiescent gas environment is driven by the liquid inertia. When the surface tension or the viscous forces are not sufficient to resist the liquid inertia, (for large Reynolds and Weber numbers), the jet will break into liquid sheets, ligaments, and droplets. The primary breakup is often initiated by interfacial instabilities. As the jet penetrates into the gas, the shear instabilities on the jet surfaces develop and form interfacial waves, which subsequently break into ligaments and droplets. Large drops may break into smaller ones, which is often referred to as secondary atomization (Guildenbecher *et al.*, 2009).

### *1.1.2 Liquid Atomization in High-Speed Flows*

The injection pressure can be reduced if atomization is assisted by air flows. Air-blast atomization is the process in which the breakup of a slow-moving liquid jet is assisted by a parallel high-speed gas stream (Lefebvre, 1980). Air-blast atomization contributes to the efficient mixing of air and fuel, which is a critical process in internal combustion engines and propulsion systems. The air-blast atomization in planar and cylindrical geometries have been studied (Ling *et al.*, 2017, 2019; Agbaglah *et al.*, 2017; Lasheras *et al.*, 1998; Marmottant and Villermaux, 2004).

Jet in a crossflow (JICF) refers to a transverse jet exhausting into a fluid flowing across the orifice (Schetz *et al.*, 1980; Sallam *et al.*, 2004). Liquid jet atomization in a crossflow is used in a wide range of applications, such as gas-turbine engines and scramjets. The transversely injected jet interacts with the crossflow, leaving the jet bent over and the cross-stream deflected (Andreopoulos and Rodi, 1984). A thorough characterization of the flow dynamics of a transverse jet issuing perpendicularly into a supersonic crossflow has received considerable attentions of researchers studying fuel injection in scramjet engines (Wu *et al.*, 2015; Xiao *et al.*, 2016; Li *et al.*, 2017; Zhu *et al.*, 2019; Li *et al.*, 2019). Jet atomization in supersonic crossflows involves complex flow physics, such as shock waves, turbulence, and interfacial dynamics. The underlying physics are still not fully understood.

## *1.2 Interfacial Instability*

The atomization of bulk liquids is typically initiated by the instability at the gas-liquid interface. Furthermore, the dominant droplet size in the spray formed is often related to the wavenumber of the most unstable mode (Lefebvre and McDonell, 2017). There are several classical instability mechanisms that are important to atomization, such as Rayleigh-Plateau instability, Kelvin-Helmholtz instability, Rayleigh-Taylor instability and Richtmyer-Meshkov instability.

Rayleigh-Plateau instability refers to the instability occurring on the surface of a liquid filament driven by surface tension. The pinch-off of a droplet from an orifice and

the breakup of a liquid ligament in atomization are both governed by Rayleigh-Plateau instability. Kelvin-Helmholtz instability on the interface is triggered by the velocity difference between the two immiscible fluids. Rayleigh-Taylor instability is excited by the accelerating motion of the lighter fluid towards the heavier fluid. The formation of the mushroom-shape head of a cylindrical liquid jet in quiescent environment is attributed to the Rayleigh-Taylor instability. As for supersonic gas flows, Richtmyer-Meshkov instability occurs as a shock wave interacts with an interface between two different fluids, as seen in the shock-induced breakup of a liquid droplet.

The interfacial instability can also be absolute and convective (Lin, 2003). When an instability is absolute, local perturbations that grow in time dominate. In contrast, when an instability is convective, the perturbation will grow in space as they move away from its initial location. For a liquid jet in a quiescent environment, if the Weber number of the liquid jet, a measure of the ratio between liquid inertia and surface tension, is above the critical value, the Kelvin-Helmholtz instability is convective, otherwise the instability will be absolute (Leib and Goldstein, 1986; Chauhan *et al.*, 2006). For air-assisted atomization such as airblast atomization, the dynamic pressure ratio between the gas and liquid flows is the key parameter to determine whether the shear-induced viscous instability is convective or absolute (Fuster *et al.*, 2013).

### *1.3 Turbulence*

If the liquid is injected with a high velocity or the air flow velocity around the bulk liquid is high, the flow will eventually become turbulent. Turbulence is a phenomenon that involves coherent structures in a wide range of scales. The kinetic energy is transferred from larger eddies to smaller ones and eventually dissipated by viscosity. The length scales in turbulent flows are divided into three ranges, i.e., energy-containing range, inertial subrange, and dissipation range (Pope, 2000). The Kolmogorov length, velocity, and time scales represent the smallest scales in turbulent flows.

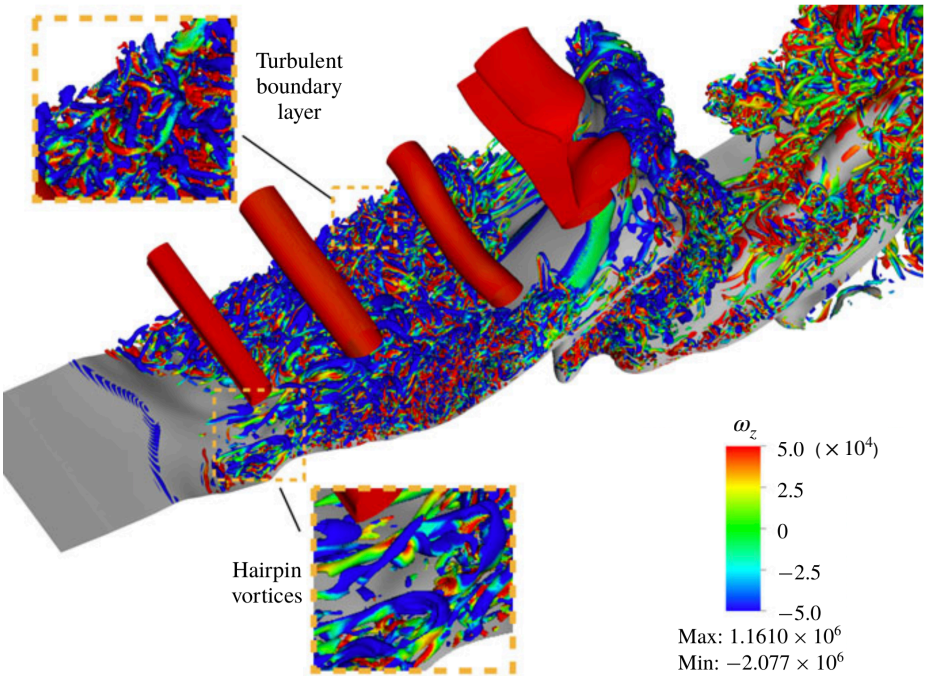


Figure 1.1. Vortical structures identified by the $\lambda_2$ criterion near the interface colored by $z$-component vorticity (Ling *et al.*, 2019).

Conventionally, turbulence research is focused on homogeneous isotropic turbulence. Homogeneous turbulence refers to turbulent flows where the flow statistics are invariant under the translations of reference frames. Likewise, isotropic turbulence refers to cases for which the flow statistics are invariant under the reflections or rotations of the axis. Nevertheless, the turbulence seen in an atomization process is often neither homogeneous nor isotropic, which makes the investigation challenging. Ling *et al.* (Ling *et al.*, 2019) studied the turbulent multiphase flows through simulating the two-phase mixing layer formed between parallel gas and liquid streams. They found that the interfacial wave plays a crucial part in turbulence transition and development. As can be seen in Fig. 1.1, vortical structures are observed for the upstream of the interfacial wave. Hairpin vortices are observed in the transition region and a turbulent wake is formed as the gas flow splits at the downstream of the wave due to the blocking of the gas flow by the large-amplitude interfacial wave.

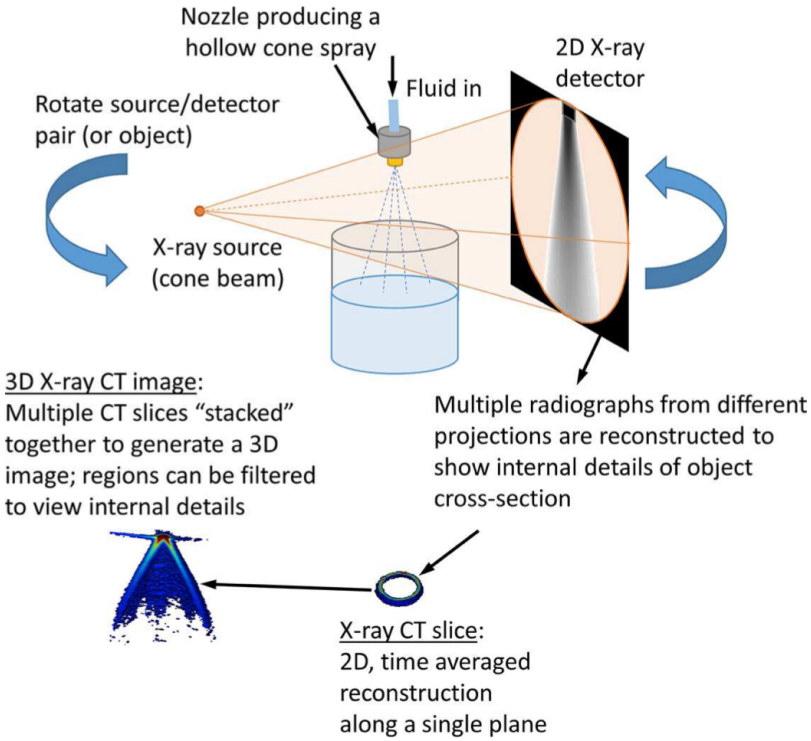


Figure 1.2. X-ray tomography setup (Heindel, 2018).

## *1.4 Approaches for Atomization Investigation*

### *1.4.1 Experimental Diagnostics*

High-speed photography and X-ray diagnostics are two popular experimental techniques to diagnose liquid jet atomization beyond the common measurement methods for single-phase flows. Whereas it is not easy to use visible light imaging to measure dense sprays in the near-field due to multiple scattering, X-rays are capable of penetrating the dense sprays (Duke *et al.*, 2017). Fig. 1.2 illustrates how the rendering of a hollow cone spray can be generated by stacking multiple X-ray computed tomography (CT) slices (Heindel, 2018).

Keshavarz *et al.* experimentally studied the ligament-mediated fragmentation dynamics of viscoelastic fluids using high-speed video imaging (Keshavarz *et al.*, 2016). They found that though the large scale features remain unchanged after adding a polymer to the liquid, thin viscoelastic ligaments are formed and connected to the core jet, see Fig. 1.3 (a) and (b). Figure 1.3 (c) shows the surface instability characterized by longitudinal and transversal surface waves (Hoyt and Taylor, 1977).

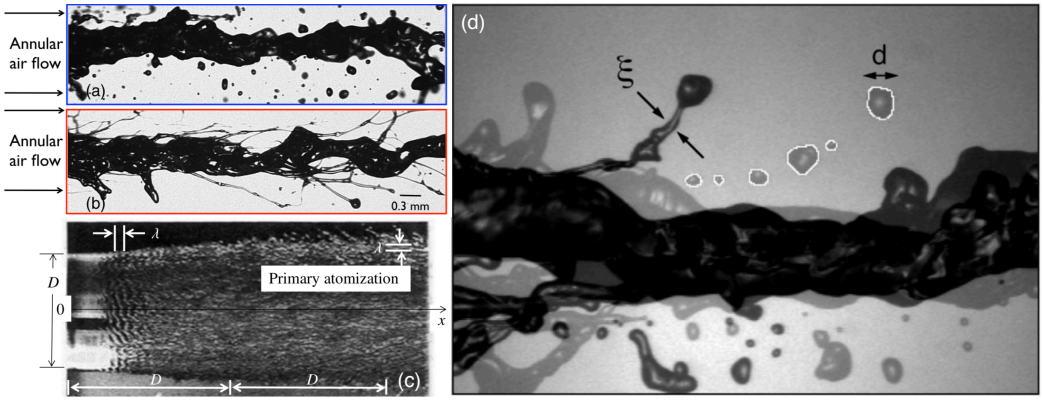


Figure 1.3. Snapshot of the liquid jet in the air-assisted atomization for (a) the Newtonian solvent and (b) the viscoelastic solution (Keshavarz *et al.*, 2016). Primary atomization of a water jet near the nozzle exit (c) (Hoyt and Taylor, 1977) and double flash exposure of a ligament just before and after breakup (d) (Villermaux *et al.*, 2004).

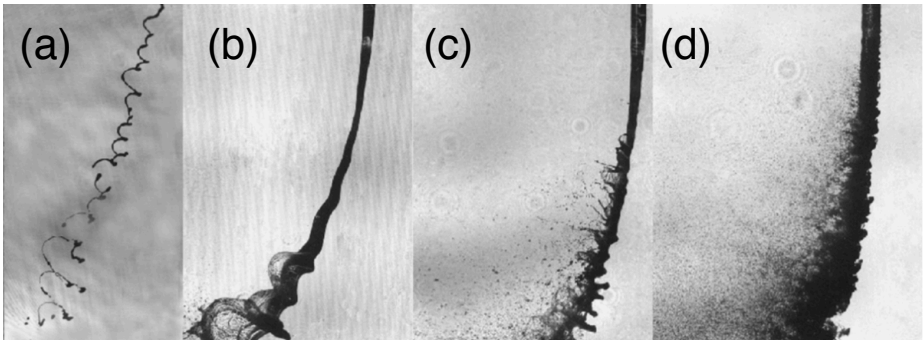


Figure 1.4. Visualization of primary breakup of liquid jets in gaseous crossflow with (a) $We = 3$, column breakup; (b) $We = 8$, bag breakup; (c) $We = 30$, multimode breakup; and (d) $We = 220$, shear breakup (Sallam *et al.*, 2004).

The axisymmetric surface waves later become asymmetric and form liquid filaments aligned with the streamwise direction, which eventually break up into droplets (Hoyt and Taylor, 1977; Umemura, 2014).

Fig. 1.4 (a-d) shows the shadowgraphs of four primary breakup regimes in JICF, i.e., the column breakup, the bag breakup, the multimode breakup, and the shear breakup (Sallam *et al.*, 2004).

1.4.1.1 *Numerical simulation.* Although experimental diagnostics is able to capture the liquid topology and flow structures, high-fidelity simulation supplements the experimental techniques and is capable of resolving small liquid structures and fine flow features.

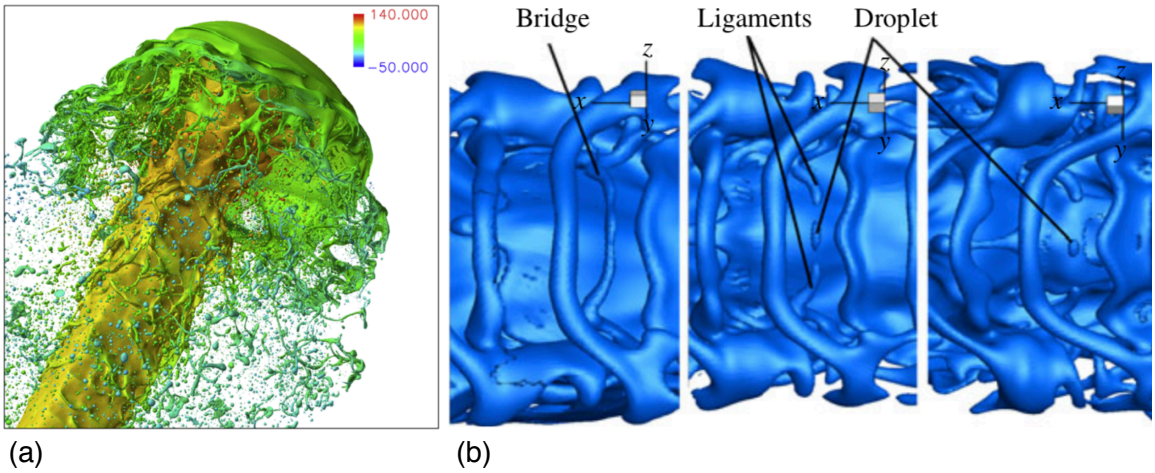


Figure 1.5. The overall flow structure of a penetrating jet with the volume of fraction colored by axial velocity in m/s (a) (Shinjo and Umemura, 2010) and sequence of bridge formation and its breakup to form an elliptical droplet at $t = 50$, 52 and 54 $\mu$s (Jarrahbashi *et al.*, 2016).

For example, the head dynamics of a cylindrical liquid jet into a quiescent environment is fully captured by the high-fidelity simulation of Shinjo and Umemura (Shinjo and Umemura, 2010). The liquid jet head region is shown in Fig. 1.5 (a) with the color representing the streamwise velocity. The collision of the jet head with the stagnant gas induces the lateral liquid spread creating a mushroom-shape tip. The liquid head is rolled up due to the Rayleigh-Taylor instability and the ligaments are generated from both the edge of the rolled-up head and the liquid column region. The droplets are pinched off from the ligament tips and a spray is formed.

Jarrahbashi *et al.* (Jarrahbashi *et al.*, 2016) studied the three-dimensional temporal instabilities of a round liquid jet segment with coaxial gas flow using a level-set method. They found that the hole formation is dominated by inertia rather than capillary forces and is related to hairpin and helical vortices. The lobes, holes, ligaments and bridges, that determine the droplet size distribution, are investigated in detail. The temporal evolution of the breakup of a liquid bridge with the formation of two ligaments and a droplet detaching from the middle bridge is shown in Fig. 1.5 (b).

Recent high-fidelity simulations showed that vortex dynamics plays a crucial role in surface deformation and atomization of a liquid jet or sheet(Zandian *et al.*, 2018). As seen in Fig. 1.6 (a), the motion of the Kelvin-Helmholtz vortex roller

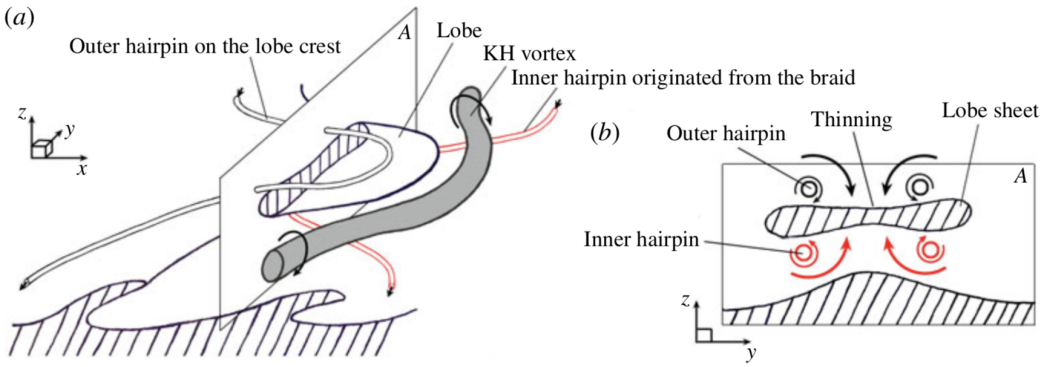


Figure 1.6. Sketch illustrating the overlapping of two hairpin vortices (a) and a plane view (b) illustrating the vortical motions in plane A (Zandian *et al.*, 2018).

induces the spanwise alignment and overlapping of the upstream hairpin vortex from the lobe crest and the downstream vortex from the braid. The opposite rotating directions of the two hairpin vortices in this cross-sectional plane cause the upward and downward motions of the lower and upper surfaces, which make the lobe easily puncture in the thinning region, see Fig. 1.6 (b).

While small-scale disturbances on the JICF lateral sides induce the near-nozzle surface disintegration, large-scale waves are formed due to the disturbances on the windward surface of the jet (Behzad *et al.*, 2016). See Fig. 1.7 (a,b). Windward disturbances lead to regular surface corrugations, see Fig. 1.7 (c). The aerodynamic force pulls the wave crests towards the leeward side, creating irregularities due to the complex flow in this low pressure region (Behzad *et al.*, 2016). See Fig. 1.7 (d).

1.4.1.2 *Theorectical analysis.* Stability analysis is oftentimes taken as an analysis tool contributing to better understanding the simulation results. In linear stability analysis, small disturbances are superposed on the undisturbed basic state (Reed *et al.*, 1996). It is crucial to determine the growth and decay of the perturbations. A flow is stable if all the perturbations decay. The normal mode approach assumes the growth of the perturbation is exponential. For inviscid parallel flows, the linearized Euler equations lead to the Rayleigh equation, while for viscous parallel flows, the linearized Navier-Stokes equations reduce to the Orr-Sommerfeld equations. An important outcome of the stability analysis is the dispersion relation between the

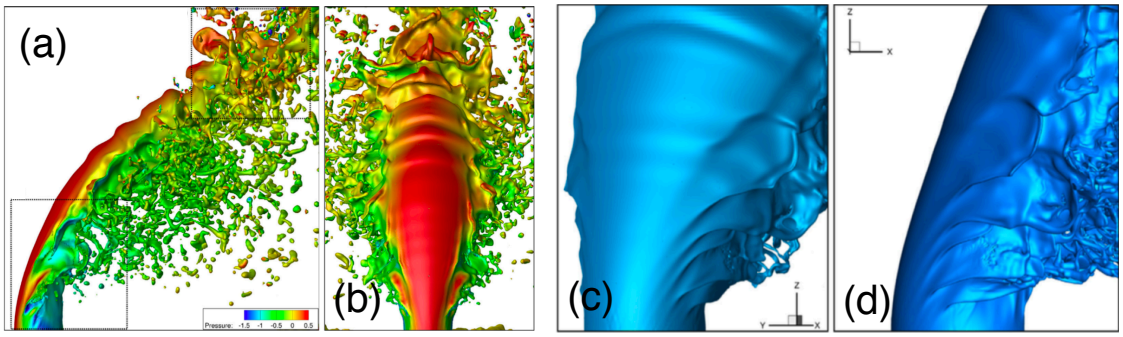


Figure 1.7. Pressure-colored jet surface snapshot of the jet side view (a) and back view (b) illustrating the breakup processes with the two boxes enclosing the near-nozzle and far-field regions (Behzad *et al.*, 2016). Close-up of the jet windward surface (c) and (d) (Behzad *et al.*, 2016).

growth rate and the frequency for temporal instability or the wave number for spatial instability. Due to the stabilizing mechanisms, such as viscosity and surface tension, the dispersion relation typically indicates the most unstable frequency or wave number in the instability, for which the growth rate is maximum. The most unstable modes are usually related to the size of droplets and filaments formed in atomization (Lin, 2003; Rangel and Sirignano, 1988; Lasheras and Hopfinger, 2000; Boeck and Zaleski, 2005; Otto *et al.*, 2013; Fuster *et al.*, 2013).

## *1.5 Numerical Methods for Compressible Interfacial Multiphase Flows*

It is computationally challenging to capture both the sharp interface and shock waves. Robust numerical methods are required to deal with interfaces and shocks discontinuities in a compressible flow. In the following, we will briefly introduce the common numerical methods for resolving the interfaces and shock waves.

### *1.5.1 Interface-Capturing Methods*

Different numerical methods have been developed to track the interface in multiphase flows. The lattice Boltzmann method (Lee and Liu, 2010; Leclaire *et al.*, 2013; Liu *et al.*, 2014), the arbitrary Lagrangian-Eulerian method (Corot *et al.*, 2020; Hu *et al.*, 2001; Luo *et al.*, 2004), the front-tracking method (Unverdi and Tryggvason, 1992; Tryggvason *et al.*, 2001; Bo *et al.*, 2011), the level-set method (Osher and Sethian, 1988; Osher and Fedkiw, 2001; Sethian and Smereka, 2003), and the

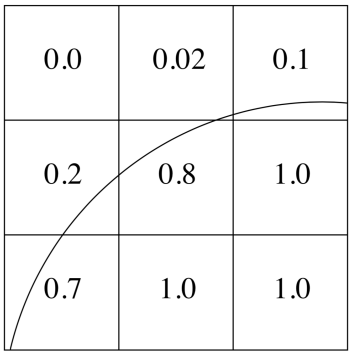


Figure 1.8. A portion of the interface with the color function value specified in each cell (Tryggvason *et al.*, 2011).

volume-of-fluid method (Hirt and Nichols, 1981; Lafaurie *et al.*, 1994; Scardovelli and Zaleski, 1999) are the most popular numerical schemes in capturing and resolving the interface motion. In the front tracking method, the interface is represented by connected marker points, which are advected in the Lagrangian framework (Unverdi and Tryggvason, 1992). The different fluids are described with a smooth level-set function and the interface is represented by a zero level-set curve in the level-set method (Osher and Sethian, 1988). In the volume of fluid (VOF) method, a color function $C$ is used to identify the liquid and gas with $C = 0$ and 1 in the computational cell describing the gas and liquid phase, respectively (Hirt and Nichols, 1981). A fractional value of $C$ denotes the interface between the two fluids, see Fig. 1.8. Whereas the level-set method is capable of easy calculation of the interface normal vector and curvature, the mass is not well conserved. In contrast, the mass is well conserved by the volume-of-fluid method, which is important to simulation of atomization and sprays.

### *1.5.2 Shock-Capturing Methods*

A number of shock-capturing methods have been developed to resolve sharp discontinuities such as shocks and contact surfaces in supersonic flows. The shock-capturing methods aim to eliminate the spurious oscillations near the shocks and other discontinuities without influencing the smooth regions. In order to decrease the computational cost in the exact Riemann solvers, approximate Riemann solvers

have been developed (Harten and Lax, 1981; Roe, 1981). To simulate compressible multiphase flows, Johnsen and Colonius (Johnsen and Colonius, 2006) incorporated the Mie-Gruneisen equation of state in the Harten Lax van Leer Contact (HLLC) approximate Riemann solver and used weighted essentially non-oscillatory (WENO) scheme in the reconstruction of the flow properties in a cell (Liu *et al.*, 1994). Capillary effect plays a crucial role in atomization in supersonic flows. As yet, only a few studies consider capillary effect in compressible multiphase flow simulations. Garrick *et al.* (Garrick *et al.*, 2017) employed the HLLC solver to simulate the compressible multiphase flow with capillary forces and used the Tangent of Hyperbola for Interface Capturing (THINC) interface reconstruction scheme for interface capturing. This method is used to simulate a liquid jet penetrating into a compressible crossflow at various Weber numbers. An all-Mach method for simulation of compressible multiphase flows with surface tension were proposed by Fuster and Popinet (Fuster *et al.*, 2018), where the conservative variables and volume-fraction are consistently advected. The method was employed to simulate the collapse of an air bubble in liquid and the simulation results agree well with the experiment.

### *1.6 Goal of this Dissertation*

The goal of this dissertation is to investigate the atomization of bulk liquid in both a quiescent environment and in a supersonic flow. The *Gerris* and *Basilisk* flow solvers will be used for the simulations. For the simulation of liquid atomization in supersonic flows, new numerical methods will be developed and implemented in the *Basilisk* code.

The specific objectives of this dissertation include:

- To investigate the formation, falling and oscillation dynamics of a dripping water drop in quiescent environment;
- To simulate the injection and atomization of a cylindrical gasoline surrogate jet in a quiescent environment under ECN spray G operating condition;

- To develop numerical methods to simulate the liquid atomization in a supersonic flow.

Detailed discussions of these three subjects are to be presented in sequence in Chapters two to four. Summary of the key findings of the whole dissertation and expected future work will be provided in Chapter five.

# CHAPTER TWO

## Short-Term Oscillation and Falling Dynamics for a Water Drop Dripping in Quiescent Air

### *2.1 Introduction*

The falling dynamics of an oscillating drop is essential to many natural phenomena and industrial applications, such as rain drops (Feng and Beard, 1991) and inkjet printing (Basaran *et al.*, 2013). For drops that are formed by a nozzle, the drop characteristics can be controlled through the inflow rate. When the inflow rate is large, the injected liquid inertia dominates and the drop formation is in the jetting regime; when the inflow rate is small, then gravity plays the dominant role, placing the drop formation in the dripping regime (Clanet and Lasheras, 1999). In the present study, we focus on one specific case in the dripping regime. The purpose of the study here is to provide a comprehensive description of the short-term oscillation and falling dynamics for the dripping drop.

The initial conditions for the drop fall are determined by the drop formation process. Since the shape oscillation of the falling drop is triggered by the non-equilibrium shape and the velocity field when the drop is just formed, the shape oscillation will in turn impact the falling dynamics of the drop and the development of the transient flow around the drop. Nevertheless, despite its importance, the effect of drop formation on the subsequent oscillation and falling dynamics have not received enough attention in former studies. Instead of using the precise post-drop-formation state, *ad hoc* initial conditions (such as a simple spheroid shape), are often used in simulations (Lalanne *et al.*, 2013; Agrawal *et al.*, 2017; Bergeles *et al.*, 2018). To fully incorporate the effect of drop formation, the whole process starting from drop growth, continuing with detachment, and eventually fall, is considered in the present simulation. Another important advantage of simulating the whole process is that an experiment

with exact conditions can be done to validate the simulation results. This is hard to achieve if *ad hoc* initial conditions are specified like in former simulations.

### *2.1.1 Drop Formation*

The dripping drop first develops as a pendant drop, hanging at the nozzle exit. When the drop volume is smaller than the critical volume, the surface tension is strong enough to resist gravity and to keep the drop stably attached to the nozzle (Padday and Pitt, 1973; Sumesh and Govindarajan, 2010). As the volume of the pendant drop reaches the critical value, the drop becomes unstable and a neck is formed between the nozzle and the main body of the drop (Schulkes, 1994; Coullet *et al.*, 2005). The minimum radius of the neck rapidly decreases, giving rise to an increasingly large capillary pressure in the neck. This high pressure drives the liquid away from the neck toward the nozzle and the main body of the drop, further accelerating the pinching process.

The pinching of the liquid neck will eventually detach the drop from the nozzle and the pinching dynamics has been studied extensively in the past. The overall pinching process is dictated by surface tension, inertial, and viscous forces (Castrejón-Pita *et al.*, 2015). The pinching process exhibits a finite-time singularity and a universal self-similar behavior near the singularity (Eggers, 1993; Eggers and Dupont, 1994; Papageorgiou, 1995; Day *et al.*, 1998; Zeff *et al.*, 2000; Chen *et al.*, 2002; Doshi *et al.*, 2003; Castrejón-Pita *et al.*, 2012). For low-viscosity liquids like water, inertia of the liquid flow toward the main body of the drop results in the shift of the local minimum of bridge radius toward the top of the drop, where the interface overturns before pinching eventually occurs.

To obtain details of the flow field in the drop formation process, advanced experimental diagnostics and high-resolution simulations are required (Wilkes *et al.*, 1999; van der Bos *et al.*, 2014; Borthakur *et al.*, 2017). By recording two consecutive images of the same drop with a small time delay, van Der Bos *et al.* (van der Bos *et al.*, 2014) extracted the longitudinal velocity profile during drop formation.

For the present problem, the viscosity and density of the surrounding air are small compared to those for water, and the effect of the surrounding air on drop formation is small. When the surrounding fluid has similar density or viscosity as the drop fluid, the surrounding fluid can have a significant impact on the drop formation dynamics (Zhang, 1999a).

### *2.1.2 Oscillation of a Free Drop*

Following the formation, the drop falls under the action of gravity. Since the shape of the drop just after detachment is out of equilibrium, the capillary force will cause the drop to oscillate when it falls. Drop oscillation is a classic fluid mechanics problem, and the early investigation on the oscillation of a free drop can be traced back to the pioneering work of Rayleigh (Rayleigh, 1879). (A free drop here refers to a drop that is located in an unbounded domain without gravity and falling motion.) For the infinitesimal amplitude oscillation of a free and inviscid liquid drop, Rayleigh decomposed the shape of the drop into spherical harmonic modes and calculated the corresponding frequency for each mode (Rayleigh, 1879). The original work of Rayleigh is based on a free-surface approximation. The extension to incorporate the effect of ambient fluid and the viscous effect was made by Lamb (Lamb, 1932), and later followed by others (Reid, 1960; Miller and Scriven, 1968; Prosperetti, 1980).

Lamb's theory is generally valid for low-viscosity fluids. Yet Miller and Scriven (Miller and Scriven, 1968) showed that even if the viscosities of the drop and surrounding fluid are both small, the viscous effect cannot be ignored since the oscillation damping rate is controlled by the boundary layer developed near the interface. The transient effect on the oscillation frequency and the damping rate was investigated by Prosperetti (Prosperetti, 1980) and it is shown that the predictions based on normal mode analysis by Lamb (Lamb, 1932) are strictly valid only asymptotically. When the oscillation amplitude is finite, the nonlinear effect on drop oscillation becomes important. Typical nonlinear effects include decrease of oscillation frequency with oscillation amplitude, asymmetry in oscillation amplitude, and coupling between dif-

ferent oscillation modes (Tsamopoulos and Brown, 1983; Natarajan and Brown, 1987; Becker *et al.*, 1991; Basaran, 1992; Becker *et al.*, 1994).

### *2.1.3 Dynamics of a Falling Drop*

For a falling drop, the oscillation dynamics and the transient flow around the drop become more complicated. Extensive numerical and experimental studies have been performed to understand the long-term falling dynamics of liquid drops after the terminal velocity is reached (see for example (Gunn, 1978; Feng and Beard, 1991; Helenbrook and Edwards, 2002; Feng, 2010)). Those research efforts were usually motivated by the interest in rain drops in atmospheric science. The present study has a different focus, that is, on the short-term dynamics of the falling drop. Here, the short-term and long-term are defined with respect to the response time required for the drop to reach the terminal velocity. The interest on the short-term behavior is motivated by the fact that, for many applications of falling drops, such as inkjet printing, the drop will reach a substrate or a liquid film far before reaching the quasi-steady state. Furthermore, the oscillation dynamics of a falling drop in the short term has also lead to new technology to measure liquid properties, *e.g.*, Staat *et al.* (Staat *et al.*, 2017) recently proposed new methods to measure surface tension and drop viscosity based on the short-term oscillation frequency and damping rate.

In the short term, the drop velocity and Reynolds number increase over time and the viscous flow around the drop is transient. Furthermore, due to the falling motion and the induced shear stress, the equilibrium shape of the oscillating drop is not spherical in general (Feng, 2010). Because of these additional complexities, there is no general analytical solution for the problem and numerical approaches are required to solve the governing equations (Lalanne *et al.*, 2013; Tripathi *et al.*, 2014; Agrawal *et al.*, 2017; Bergeles *et al.*, 2018). Owing to the similar dynamics between a falling drop and a rising bubble, these two cases are often discussed together (see for example (Ern *et al.*, 2012)), although a fundamental difference between these two cases exists (Tripathi *et al.*, 2014). It is challenging to accurately measure the three-dimensional

flow inside a small drop in experiments. By seeding tracer particles of an average size of 10 µm, Chung and Trinh (Chung and Trinh, 2000) obtained instantaneous velocity maps inside an oscillating drop which is electrostatically levitated.

### *2.1.4 Numerical Simulation*

Thanks to the development of advanced interface capturing techniques in the past decades, direct numerical simulation is now capable of capturing interfacial flows that exhibit topology changes (Tryggvason *et al.*, 2011) and can also provide high-level details of the flow field that are difficult to measure in experiments. Extensive numerical studies have been conducted to simulate the drop formation process by the volume-of-fluid (VOF) method, see for example, (Zhang, 1999b) and (Gueyffier *et al.*, 1999). The recent simulations by Agrawal *et al.* (Agrawal *et al.*, 2017) have used the VOF method to resolve the oscillation of a falling drop with a non-spherical initial shape. It is shown that the oscillation only arises in the longitudinal direction and no azimuthal variation was observed even when vortex shedding occurs in the wake of the drop. Another recent work by Bergeles *et al.* (Bergeles *et al.*, 2018) presented high-resolution three-dimensional simulation results for a falling drop of millimeter class. The detailed flow structure was well captured and in particular, the roller vortex that is required to link the circulation in the wake of the drop with a Hill vortex inside the drop was clearly unveiled. For a similar problem, Lalanne *et al.* (Lalanne *et al.*, 2013) have performed axisymmetric simulations using the level-set method for the oscillation of rising drops and bubbles. It was found that the oscillation frequency decreases slightly with the rising velocity while the damping rate of the drop oscillation is significantly magnified due to the rising motion.

### *2.1.5 Goal of this Study*

In spite of of the extensive studies discussed above, a comprehensive understanding of the short-term oscillation and falling dynamics for a dripping drop remains to be established. In particular, the effect of drop formation on the oscillation dynamics

and the transient flow around the falling drop are still not fully understood. To the knowledge of the authors, there is no previous study that considers the effect of the drop formation on the oscillation dynamics of a falling drop. The oscillation of a drop is dictated by the initial conditions which are in turn set by the drop formation process. Former numerical studies generally assumed the initial drop shape to be ellipsoidal or spherical with a constant initial velocity within the drop (Lalanne *et al.*, 2013; Agrawal *et al.*, 2017; Bergeles *et al.*, 2018). However, the shape of the drop when it is just formed is far more complex than an ellipsoid, and furthermore, the velocity field in the just-formed drop is highly non-uniform due to the pinching dynamics. The former simulations with simplified initial conditions are useful to understand the general physics of oscillation of a falling drop. Nevertheless, in order to precisely predict the shape and dynamics of the falling drop, which are critical to many applications of drops, *e.g.*, the impact of a falling drop on a deep pool (Deka *et al.*, 2017), the effect of drop formation on the subsequent drop oscillation and falling dynamics must be faithfully incorporated.

The goal of the present study is therefore to investigate the dynamics of a water drop dripping in quiescent air through simulation and experiment. Particular focus will be placed on the drop oscillation dynamics and the development of the transient flow around the drop. To achieve this goal, one specific case is considered in the present study. The flow rate at the nozzle inlet is chosen to be sufficiently small, so that the drop formation is in the dripping regime and the drop growth is quasi-static. Furthermore, we focus on only the short term of the drop fall, during which the drop shape and the flow remain axisymmetric. The key questions that the present study aims to address include:

- Are the "initial conditions" set by the drop formation process important to the drop oscillation and falling dynamics?
- How do the nonlinear dynamics and falling motion influence the drop oscillation dynamics, such as the oscillation frequency and damping rate?

- How do the drop oscillation and the falling motion contribute to the development of the transient flow around the drop? Is the flow structure within the drop similar to the classic Hill vortex?

To address these questions, axisymmetric simulations are carried out with the adaptive multiphase flow solver, *Gerris*. An experiment with the same conditions has also been conducted to validate the simulation results. The simulation and experimental approaches are described in section 2.2. The results for drop formation, shape oscillation, and transient flow around the drop, will be presented and discussed in sequence in sections 2.3, 2.4 and 2.5, respectively. Finally, concluding remarks will be given in section 4.5.

## *2.2 Methodology*

### *2.2.1 Key Parameters*

The process of drop formation is controlled by physical parameters listed in Table 2.1, including the liquid and gas properties, the nozzle radius, the gravity acceleration, and the inlet flow rate. The mean inflow velocity, $u_0 = Q/\pi R_0^2 = 0.265$ mm/s can serve as an alternative for the inflow rate $Q$. The key dimensionless parameters can be derived and the values are given in Table 2.2. Since the gas-to-liquid density and viscosity ratios, $r$ and $m$, are both very small, the effect of the gas phase on drop formation is small. The Weber, Ohnesorge, and Bond numbers are measures of the relative importance of the fluid inertia, liquid viscosity, and gravity with respect to surface tension. For the small $Q$ used in the present problem, the drop formation process is quasi-static and $We = 8.17 \times 10^{-7} \ll 1$. The effect of inflow inertia is thus negligible. The variation of $We$ does not influence the drop formation (Wilkes *et al.*, 1999) and the value of $Q$ is immaterial to the results to be presented, as long as $Q$ remains to be small. Due to the relatively low viscosity of water, $Oh = 0.00426$, is also very small, suggesting that the viscous effect is generally small in the drop formation process. Finally, the Bond number is the primary dimensionless parameter to determine the sizes of the detached primary and secondary drop.

Table 2.1. Physical parameters for the formation of a dripping drop.

| $\rho_l$ (kg/m$^3$) | $\rho_g$ (kg/m$^3$) | $\mu_l$ (Pa s) | $\mu_g$ (Pa s) | $\sigma$ (N m) | $R_0$ (m) | $g$ (m/s$^2$) | $Q$ ($\mu$L/min) |
|---|---|---|---|---|---|---|---|
| 1000 | 1.2 | $0.85 \times 10^{-3}$ | $1.8 \times 10^{-5}$ | 0.0688 | $8 \times 10^{-4}$ | 9.81 | 32 |

After the drop detaches from the nozzle, the drop radius is measured to be $R_d = 1.86$ mm. The oscillation and falling dynamics of the drop can be fully determined by the Reynolds and Weber numbers based on the drop diameter ($D_d = 2R_d$), namely $Re_d \equiv D_d u_d \rho_g / \mu_g$ and $We_d \equiv D_d u_d^2 \rho_g / \sigma$, along with the post-formation state of the drop as the initial conditions. As the drop velocity, $u_d$, increases over time, $Re_d$ and $We_d$ rise accordingly. In the time range considered in the present study, the drop velocity increases from 0.07 m/s (just after detachment) to about 1.70 m/s. The corresponding range of drop Reynolds and Weber numbers are $25.9 \lesssim Re_d \lesssim 633$ and $2.62 \times 10^{-4} \lesssim We_d \lesssim 0.156$. For this range of $Re_d$, the flow was observed to remain approximately axisymmetric in the experiment. It was measured that the deviation of the drop centroid from the nozzle axis is smaller than 0.3% of the falling distance in the time range considered. Furthermore, as $We_d$ is small, the surface tension will be sufficient to avoid an aerobreakup. According to the experiment of Gunn and Kinzer (Gunn and Kinzer, 1949), the terminal velocity for this drop size is about 6.2 m/s. The Reynolds and Weber numbers corresponding to the terminal falling velocity will then be about $Re_{d,t=\infty} \approx 1600$ and $We_{d,t=\infty} \approx 2.4$. It is clear that the drop velocity in the present study remains far from the terminal state. The drop oscillation Ohnesorge number, $Oh_{osc} = \mu_l / (\rho_l \sigma R_d)^{1/2}$, is often used to characterize the viscous effect on the oscillation of a free drop, which can be expressed as $Oh_{osc} = \sqrt{2We_d}/(mRe_d)$. (Alternatively, the oscillation Reynolds number, $Re_{osc} = 1/Oh_{osc}$, can be used.) Here $Oh_{osc} = 0.00278$, is very small, therefore, it is expected that the viscous effect on the drop oscillation is small.

Due to the rich flow physics involved in the present problem, we have focused on only one specific case, instead of a parametric study. If the key dimensionless parameters listed in Table 2.2 vary, the specific values in the results to be shown

Table 2.2. Key dimensionless parameters for the drop formation.

| $r$ | $m$ | $We$ | $Oh$ | $Bo$ |
|---|---|---|---|---|
| $\rho_g/\rho_l$ | $\mu_g/\mu_l$ | $\rho_l u_0^2 R_0/\sigma$ | $\mu_l/\sqrt{\rho_l \sigma R_0}$ | $\rho_l g R_0^2/\sigma$ |
| 0.0012 | 0.021 | $8.17 \times 10^{-7}$ | 0.00426 | 0.091 |

later will change. However, the case selected here well represents millimeter-size low-viscosity droplets in the dripping regime. The conclusions with regard to the droplet formation, oscillation, and falling dynamics will remain valid as long as both of the Ohnesorge and Bond numbers are significantly smaller than unity. Parametric study for wider ranges of $Oh$ and $Bo$ is of interest but will be relegated to future work.

### *2.2.2 Modeling and Simulation*

2.2.2.1 *Governing equations.* The one-fluid approach is employed to resolve the two-phase flow, where the phases corresponding to the water drop and the ambient air are treated as one fluid with material properties that change abruptly across the interface. The incompressible Navier-Stokes equations with surface tension can be written as

$$\rho(\partial_t \boldsymbol{u} + \boldsymbol{u} \cdot \nabla \boldsymbol{u}) = -\nabla p + \nabla \cdot (2\mu \boldsymbol{D}) + \sigma \kappa \delta_s \boldsymbol{n}\,, \tag{2.1}$$

$$\nabla \cdot \boldsymbol{u} = 0\,, \tag{2.2}$$

where $\rho$, $\mu$, $\boldsymbol{u}$, and $p$ represent density, viscosity, velocity and pressure, respectively. The strain-rate tensor is denoted by $\boldsymbol{D}$ with components $D_{ij} = (\partial_i u_j + \partial_j u_i)/2$. The third term on the right hand side of Eq. (4.2) is a singular term, with a Dirac distribution function $\delta_s$ localized on the interface, and it represents the surface tension. The surface tension coefficient is $\sigma$, and $\kappa$ and $\boldsymbol{n}$ are the local curvature and unit normal of the interface.

The liquid volume fraction $C$ is introduced to distinguish the different phases, in particular $C = 0$ in the computational cells with only air (respectively $C = 1$ in

cells containing only water), and its time evolution satisfies the advection equation

$$\partial_t C + \boldsymbol{u} \cdot \nabla C = 0\,. \tag{2.3}$$

The fluid density and viscosity are then determined by

$$\rho = C\rho_l + (1 - C)\rho_g\,, \tag{2.4}$$

$$\mu = C\mu_l + (1 - C)\mu_g\,, \tag{2.5}$$

where the subscripts $g$ and $l$ represent the gas phase (air) and the liquid phase (water), respectively.

2.2.2.2 *Numerical methods.* The Navier-Stokes equations (Eqs. (2.1) and (2.2)) are solved by the open-source solver *Gerris* (Popinet, 2003, 2009). In *Gerris*, a finite-volume approach based on a projection method is employed. A staggered-in-time discretization of the volume-fraction/density and pressure leads to a formally second-order accurate time discretization. The interface between the different fluids are tracked by solving the advection equation (Eq. (2.3)) using a Volume-of-Fluid (VOF) method (Scardovelli and Zaleski, 1999). A quadtree spatial discretization is used, which gives a very important flexibility allowing dynamic grid refinement into user-defined regions. Finally the height-function (HF) method is used to calculate the local interface curvature, and a balanced-force surface tension discretization is used (Francois *et al.*, 2006; Popinet, 2009).

2.2.2.3 *Simulation setup.* In the numerical model, the flow is assumed to be axisymmetric. The 2D computational domain is shown in Fig. 2.1. The gravitational acceleration is along the $z$ direction. The water is injected into the domain from the left and the inlet flow rate $Q$ is kept the same as in the experiment. The thickness of the nozzle wall is ignored in the model. The ratio between the inner and outer radii of the nozzle in the experiment is 0.75. It has been shown by Ambravaneswaran *et al.* (Ambravaneswaran *et al.*, 2002) that the nozzle wall thickness can affect the drop

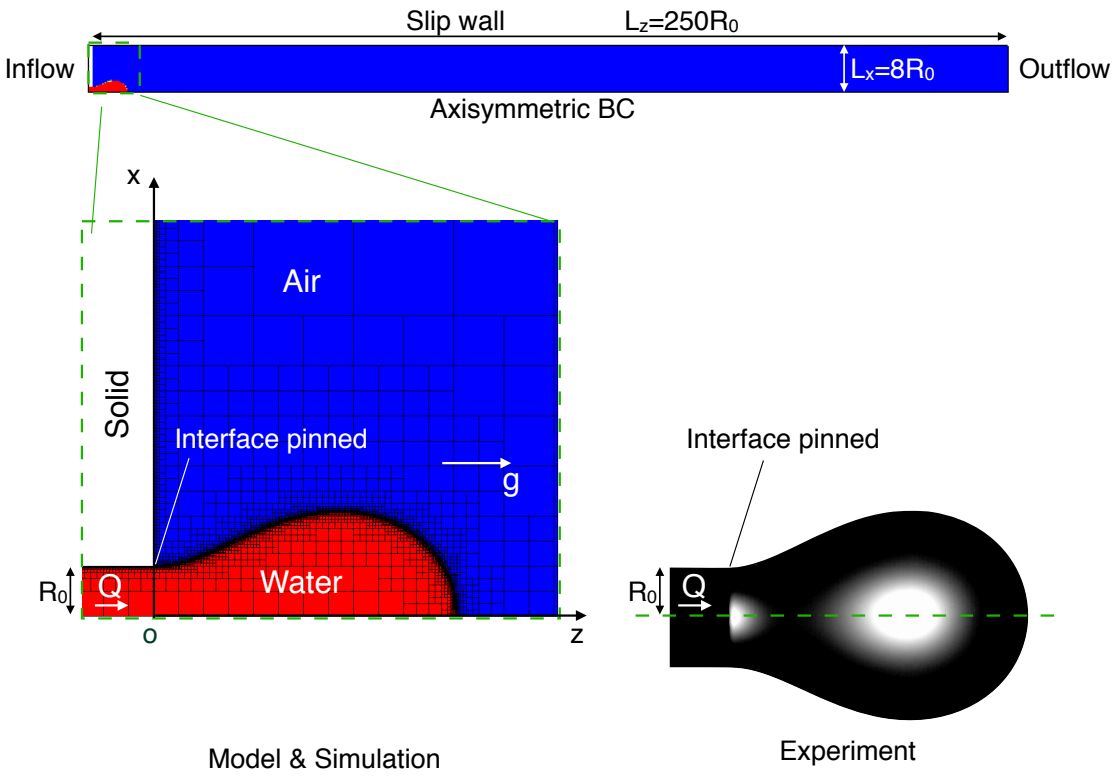


Figure 2.1. Simulation setup.

formation dynamics when the flow rate is high. For the present problem, a very small flow rate has been used. According to the experimental results of Zhang and Basaran (Zhang and Basaran, 1995) for similar small flow rates, the effect of the wall thickness becomes negligible if the ratio of the inner to the outer radii of the nozzle exceeds 0.2. The ratio in the present experiment is significantly larger than the critical value and thus the effect of nozzle wall thickness on the drop formation can be ignored.

Furthermore, a solid block is added above the nozzle, see Fig. 2.1. The boundary condition of the volume fraction $C$ at the solid boundary is $\partial C/\partial n = 0$. The reason for adding the solid block is to pin the contact line, where water, air, and solid meet, at the block corner. In the experiment, the interface is pinned at the outer perimeter of the nozzle. By setting the distance between this pinned point to the $z$–axis as $R_0$, the model and the experiment exhibit the same $Bo$. In both experiment and simulation, the contact angle varies slightly when pinching occurs, and the contact line remains pinned during the drop formation process.

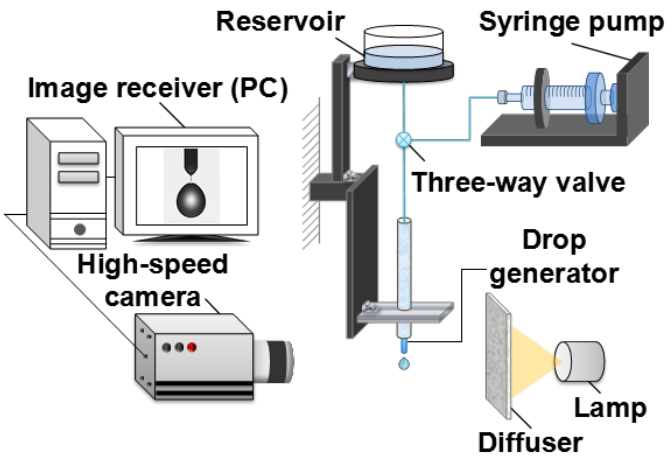


Figure 2.2. Experimental setup.

Thanks to the adaptive mesh, a computational domain that is significantly larger than the drop size can be used. As a result, the effect of boundaries on the drop can be eliminated. The length of the domain is $L_z = 200$ mm $= 250R_0$ and the height is $L_x = 6.4$ mm $= 8R_0$. The axisymmetric boundary condition is invoked at the bottom of the domain. The inflow (Dirichlet velocity and Neumann pressure conditions) and outflow (Dirichlet pressure and Neumann velocity conditions) BC's are applied to the left and the right of the domain. The top boundary is considered as a slip wall. The minimum cell size used in the simulation is determined by the maximum mesh refinement level, $L$, namely $\Delta_{\min} = L_x/2^L$. Different refinement levels have been tested and the grid-refinement results are to be shown in the next section. The time step is computed based on the restriction from the advection, viscous, and surface tension terms in the governing equations. For the present problem, the time step restriction is mainly from the surface tension due to the small capillary number (Ling *et al.*, 2016).

### *2.2.3 Experiment*

Fig. 2.2 shows the experimental setup to investigate the formation and the fall of the water drop using high-speed imaging. A stainless steel nozzle with sharp-edged exit surface was used, and its inner and outer radii are 0.6 mm and 0.8 mm, respec-

tively. Water drops were then generated from the nozzle either by the pressure from a constant-height reservoir, or by the pressure from a syringe pump (KDS210, KD Scientific). A high-speed camera (NAC Memrecam GX-1) with frame rates varying from 100 to 5,000 fps (frame per second) have been used to capture the shape of the drop. The spatial resolution and exposure time varies in the range of 20-70 $\mu$m/pixel and 20-200 $\mu$s, respectively. To minimize the influence of vibrational disturbances and temperature variations in the pinching of the drop, all experiments were conducted on an anti-vibration table in the isolated corner of a basement with air-conditioning. For better visualization, uniform illumination was achieved by placing a diffuser in front of the 100W white light LED lamp. To avoid the heating effect, the LED light was placed 1.5 meter away from the observation area and the LED light was turned on only during recording. The images obtained by high-speed camera were post-processed by Matlab code to measure the geometric properties of the drop before and after detachment, such as the volume and height of the pendant drop, the radius of the neck, the eccentricity of the falling drop.

Surface tension was measured by the Du Noüy ring method. Temperature (25 °C) and density of the test liquid were measured by a temperature recording device (Chino AH3760 with Pt100 sensor) and a mass-volume method, respectively. Liquid viscosity was determined using a rotational viscometer (Brookfield DV-II).

## *2.3 Results for Drop Formation*

The focus of the present study is on the oscillation and falling dynamics after the drop is detached from the nozzle. Nevertheless, since we aim at unveiling the effect of drop formation on the subsequent shape oscillation, the results for the drop formation will be first presented and validated against theory and experiment.

### *2.3.1 General Process and Time Scales*

A sequence of images of the drop obtained from high-speed imaging are shown in Fig. 2.3 to depict the process of drop formation and subsequent fall in quiescent

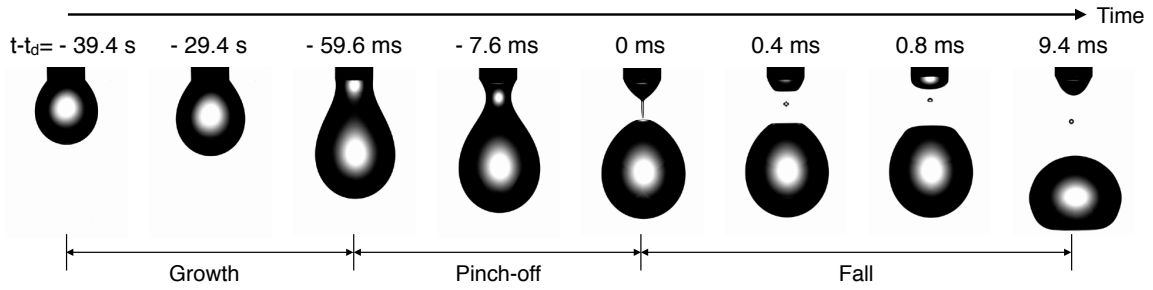


Figure 2.3. Overall process of a drop dripping from a nozzle: growth, pinch-off, and fall shown by high-speed camera images.

air. The overall process can be generally divided into three phases: growth, pinch-off, and fall. When the drop falls, it deforms in an oscillatory manner.

It should be noted that the time scales for different phases in the process are different. (The time differences between the images shown in Fig. 2.3 are not even.) The growth of the drop is very slow compared to the other two phases, simply due to small flow rate at the nozzle inlet. It takes about one minute for the pendant drop to grow to the critical volume. In contrast, when the drop volume reaches the critical volume, the developing and pinching of the neck of the pendant drop evolve at a very fast speed, taking about a millisecond. When the detached drop falls in air, the dominant oscillation period is about $\tau_{osc} = 21.5$ ms. This multiple time-scale nature makes the investigation challenging for both experiment and simulation if one aims at capturing the whole process from drop formation to fall.

To overcome this challenge, multiple experiments with different frame rates were conducted to capture different phases. For the growth of the drop, a low frame rate, 100 fps was used. For the pinching and oscillation, a high frame rate, 5000 fps was used. The theoretical solution of a static pendant drop that is close to the critical volume is used to initialize the simulation. The initial velocity throughout the domain is taken to be zero since the pendant drop is quasi-static. For the most refined simulation ($L = 11$), the simulation starts at the time that is 394 ms before the drop detaches, namely $t_d - t = 394$ ms.

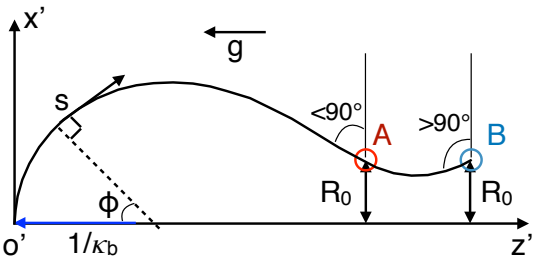


Figure 2.4. Sketch of the axisymmetric quasi-static pendant drop profile.

### *2.3.2 Drop Growth as a Pendant Drop*

Due to the small Weber and Ohnesorge numbers in the present problem, the effects of liquid inertia and viscosity on the drop formation are negligible compared to that of the surface tension. As a consequence, the drop grows quasi-statically and follows the static pendant drop theory (Padday and Pitt, 1973). For a static pendant drop, its shape is axisymmetric and the surface tension and the gravitational force are in equilibrium. The shape of the drop can then be obtained by solving a set of ordinary differential equations, which are given in Appendix A. The integration of the equations is from the bottom of the pendant drop as shown in Fig. 2.4, (a new coordinate $(x', z')$ is used,) with the curvature at the drop bottom $\kappa_b$ as the boundary condition. For each $\kappa_b$, there are multiple solutions that satisfy a given Bond number (Coullet *et al.*, 2005). Here only the two solutions which give drop volumes which are close to the critical volume are relevant. The two solutions are schematically shown in figure 2.4. While for solution A the angle between the interface and the nozzle exit is less than 90°, for solution B the angle is larger than 90°.

The volume ($V$) and the height ($Z_{\max}$) of the pendant drop can be measured from the experimental and numerical results, which are shown along with the pendant-drop theoretical predictions in Fig. 2.5(a). It can be observed that the experimental and theoretical results agree very well before the drop volume reaches the critical volume. The critical volumes measured from the experiment and simulation are both about 27.10 mm$^3$, which is very close to the value predicted by the pendant-drop theory, *i.e.*, $V_{crit} = 27.05$ mm$^3$. The $V$-$Z_{max}$ curves obtained in the experiment and

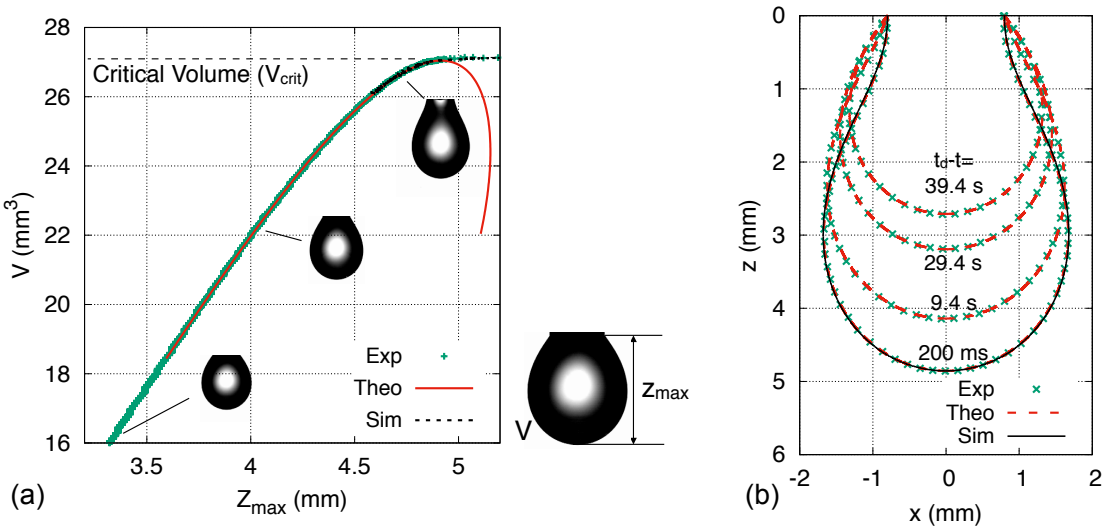


Figure 2.5. Comparison of static pendant drop theory with experimental and simulation results: ($a$) drop volume $V$ versus drop height $Z_{\max}$; ($b$) drop contours at different times. The critical volume shown in (a) is $V_{crit} = 27.05$ mm$^3$.

simulation appear to be flat when pinching occurs. During the pinching process, the rapid increase of $Z_{max}$ is due to the redistribution of volume within the drop; as a result, the drop volume increase in the fast pinching process is negligibly small. The initial conditions for the simulation are taken from the theoretical result for $V = 26$ mm$^3$. At the time, the angle between the interface and the nozzle exit is less than 90° (case A in Fig. 2.4). If the inflow at the nozzle is stopped, the pendant drop will remain stable. The simulation results of the $V$-$Z_{\max}$ curve at later times match very well with both the experiment and theory, see Fig. 2.5(a). This validates the present simulation setup in capturing the drop growth. The experimental and numerical results deviate from the theoretical solution beyond the critical $z_{\max}$, since the latter represents an unstable static solution which will not be observed in reality.

The excellent agreement between the experimental and theoretical results are also achieved in the contours of the drop at different times, as shown in Fig. 2.5(b). The experimental results are shown to match very well with the theoretical predictions at 39.4s, 29.4s and 9.4s before pinching occurs. The simulation is started at $t_d - t =$ 394 ms ($V = 26$ mm$^3$). The simulation result at $t_d - t = 200$ ms (after the simulation

has been run for a physical time of 194 ms) is compared to the theoretical and experimental results. The theoretical, numerical and experiment curves all collapse perfectly, which again validates the present experimental and simulation approaches.

### *2.3.3 Pinching and Drop Detachment*

As the pendant drop reaches the critical volume, it becomes unstable. The interface evolution during the pinching process for both simulation and experiment is shown in Fig. 2.6. The numerical and experimental results generally agree very well for the formation of the neck and the liquid bridge, the detachment of the primary drop, and finally the formation of the secondary drop. In Figs. 2.6(c)–(d), there exists a small discrepancy in the drop contours between experiment and simulation. This is due to the concave shape at the top of the drop, which cannot be seen from the experimental images taken from the lateral side.

To better elucidate the pinching dynamics and the formations of the primary and secondary drops, temporal evolutions of the pressure and velocity fields are plotted in Fig. 2.7. As the drop reaches the critical volume, a "neck" develops between the nozzle and the pendant drop. The minimum radius of the neck ($x_{\min}$) decreases rapidly over time. As a consequence, the pressure in the neck, which is inversely proportional to the neck radius, also increases rapidly. The pressure difference between the neck and the regions above and below the neck expels the liquid away from the neck with increasing velocity, see Figs. 2.7(a)–(d). The thinning process of the neck contributes to the elongation of the pendant drop and the neck turns into a thin liquid bridge. The minimum radius is initially located at about the center of the liquid bridge. The stagnation point is slightly higher than the location for the minimum neck radius. As the liquid accelerates from the stagnation point toward the attached liquid and the primary drop, see *e.g.*, Fig. 2.7(c), the radius near the top and bottom of the bridge decreases faster than that near the center. The local radius minimum then shifts from the center to the bottom of the liquid bridge, see Fig. 2.7(d). Pinching first occurs at the location for the new minimum radius near

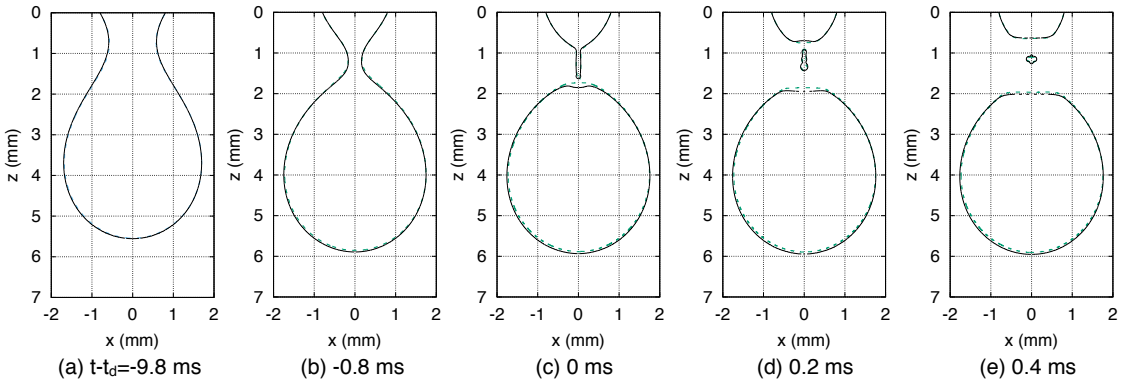


Figure 2.6. Comparison between the numerical (solid lines) and experimental (dashed lines) results for the process of drop detachment.

the bottom of the bridge, detaching the primary drop. After the pinch-off, the liquid filament rapidly retracts upward from the pinch-off location. Due to similar effect of the inertia of the upward fluid motion, a new local minimum of radius develops at the top of the liquid bridge, see Fig. 2.7(g), where soon another pinching happens. At the end, the liquid bridge is separated from the attached liquid and the primary drop, forming the secondary drop (see Fig. 2.7(h)). A closeup of the secondary drop is also provided to show the high-resolution mesh used to resolve the pinching process. The dynamics of drop formation shown in the present experiment and simulation are consistent with former studies of drop formation (Zhang and Basaran, 1995; Wilkes *et al.*, 1999; Popinet, 2009) and filament breakup (Castrejón-Pita *et al.*, 2015).

Since for the present problem $Oh \ll 1$, the pinching process is mainly in the inertial regime where the temporal evolution of the minimum radius follows the 2/3 power law: $x_{\min} \sim (t_d - t)^{2/3}$. As the new minimum radius shifts from near the center toward the two ends of the liquid bridge, the downward flow from the neck to the primary drop slows down, reducing the local Reynolds number and bringing the pinching dynamics into the viscous regime (Castrejón-Pita *et al.*, 2015), where $x_{\min} \sim (t_d - t)$. The temporal evolution of $x_{\min}$ for both experiment and simulation is plotted in Fig. 2.8(a), where the two power-law scalings and the transition from the inertial to viscous regimes can be clearly identified. As the viscous regime cannot

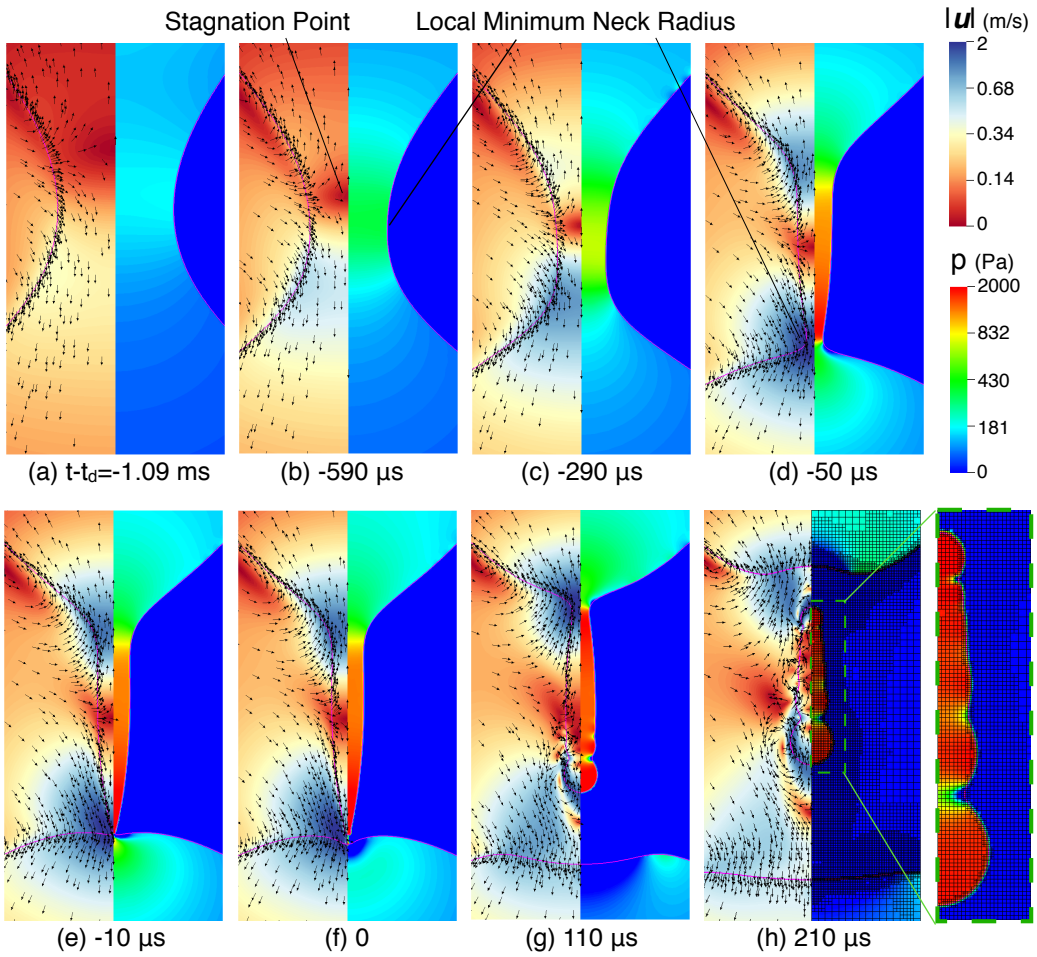


Figure 2.7. Evolution of the velocity (left) and pressure (right) fields for the formation of primary and secondary drops. Skewed color scales have been used for better visualization.

sustain to the eventual breakup, another transition from the viscous regime to the inertial-viscous regime will occur in the pinching process at an even smaller time scale. Nevertheless, that time scale for the present problem with such a small $Oh$ is hard to resolve by simulation. Yet ignoring the inertial-viscous regime seems to introduce little effect on the formation of the primary drop.

The elongation of the drop due to the pinching process is measured and shown in Fig. 2.8(b). Again the numerical and experimental results agree very well. When the primary drop detaches from the liquid bridge, the drop height is about $z_{\max}/R_0 = 7.35$. Similar experiments of dripping water drops by Zhang and Basaran (Zhang and Basaran, 1995) showed that $z_{\max}/R_0 = 9.92$ and 5.58 for nozzle radius $R_0 = 0.4$ and 1.6 mm, respectively. In the present study, $R_0 = 0.8$ mm, so the drop height at the detachment time is in a good agreement with the experimental results.

Due to the low liquid viscosity in the present problem, when the liquid rushes from the neck toward the to-be-formed drop, the interface overturns before pinch-off occurs (Day *et al.*, 1998; Chen *et al.*, 2002). The overturning of the interface at the bottom of the liquid bridge can be identified with a careful look at Fig. 2.7(e). A closeup of the interface near the pinch-off location is presented in Fig. 2.8(c) to better show the overturning interface. The simulation results are shown to approach the self-similar solution given by Day *et al.* (Day *et al.*, 1998). For the same minimum radius $x_{min}/R_0 = 0.0028$, the overturning interface obtained in the present simulation agrees well with the inviscid flow result (Day *et al.*, 1998).

The excellent agreement between the simulation, experiment, and theoretical results for both drop growth and detachment fully affirms that the drop formation is well captured and its effect on the subsequent fall of the drop has been faithfully incorporated in the present study.

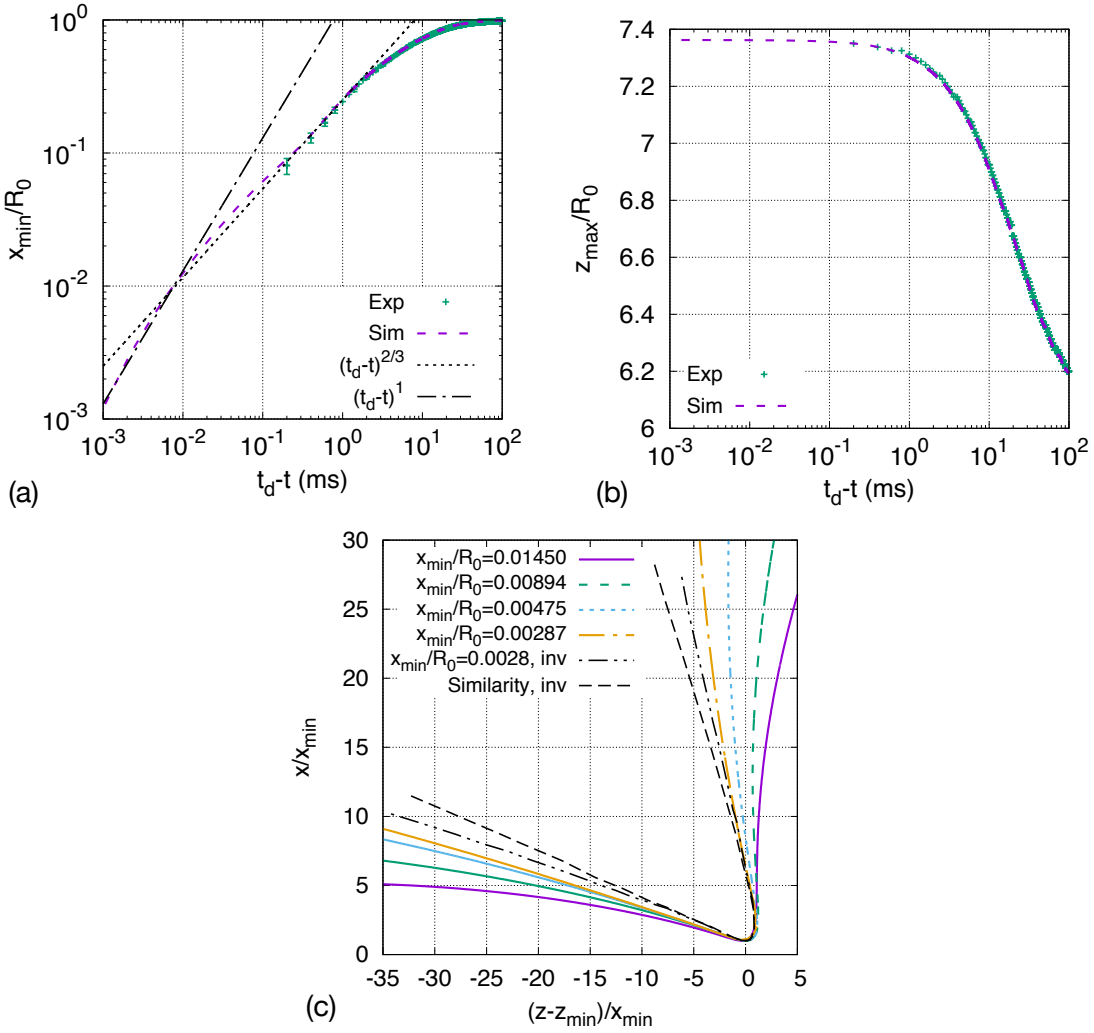


Figure 2.8. Temporal evolution of (a) the minimum radius $x_{min}$, (b) the drop height $z_{max}$, and (c) the interface profiles near the pinching location prior to drop breakup. The dotted and dash-dotted lines in (a) indicate the $(t_d - t)^{2/3}$ and $(t_d - t)$ power laws for the inertial and viscous regimes, respectively. The error bars on the experimental data in (b) are smaller than the line thickness and thus are not plotted. The simulation results shown in (c) approach the inviscid self-similar solution provided by (Day *et al.*, 1998).

### *2.4.1 Validation Studies for Oscillation and Falling Dynamics*

When the drop is detached from the nozzle, the drop shape is elongated and out of equilibrium. Under the action of surface tension, the drop starts to deform and oscillate. The eccentricity of the drop, defined as the ratio between the height ($b$) and the width ($a$) of the drop, $e = b/a$, is a common parameter to characterize the shape deformation of an oscillating drop. The height $b$ is defined as the difference between the minimum and maximum z-coordinates of the droplet surface and thus does not account for the concave shape near the top of the drop shown in Fig. 2.6. The temporal evolutions of $e$ obtained from simulations with different meshes are compared with the experimental measurement in Fig. 2.9. It is observed that the second mode dominates the oscillation of $e$ and the time period agrees well with that for the second mode of Lamb, $\tau_{2,Lamb}$. Therefore, $\tau_{2,Lamb}$ is taken to be the reference time scale for drop oscillation, namely $\tau_{osc} = \tau_{2,Lamb}$, and in Fig. 2.9 time is normalized by $\tau_{osc}$. This indicates that the falling drop retains similar dominant frequency (or periods) as for a free drop. This observation is consistent with the former studies (Lalanne *et al.*, 2013; Staat *et al.*, 2017; Bergeles *et al.*, 2018).

The angular frequency for the $n^{\text{th}}$ spherical harmonic mode for small-amplitude oscillations of a free, viscous, and incompressible drop was derived by Lamb (Lamb, 1932), which is given as

$$\omega_{n,Lamb}^2 = \frac{(n-1)n(n+1)(n+2)\sigma}{[(n+1)\rho_l + n\rho_f]R_d^3}\,. \tag{2.6}$$

The frequency is $f_{n,Lamb} = \omega_{n,Lamb}/(2\pi)$ (for convenience $\omega$ is simply referred to as "frequency" in the rest of the paper) and the time period is $\tau_{n,Lamb} = 1/f_{n,Lamb} = (2\pi)/\omega_{n,Lamb}$. For the second mode, the angular frequency is $\omega_{2,Lamb} = 292$ s$^{-1}$, and the oscillation period $\tau_{2,Lamb} = 21.5$ ms. The Lamb frequencies for other modes, $\omega_{n,Lamb}$, for the present drop size are listed in Table 2.3.

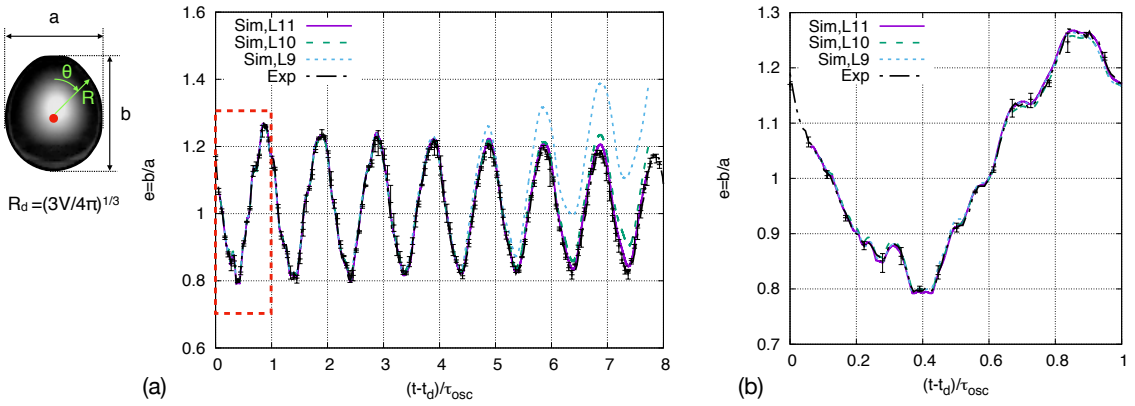


Figure 2.9. Temporal evolution of the drop eccentricity for experiment and simulation. Here, the eccentricity is defined as $e = b/a$, where $b$ and $a$, as indicated, represent the height and width of the drop, respectively. The simulation results for different maximum mesh refinement levels ($L$) are compared to the experimental data in figure (a) and a closeup for $0 < (t - t_d)/\tau_{osc} < 1$ is given in figure (b). The corresponding minimum cell size $\Delta_{\min}$ for $L = 11$, 10, and 9 are 3.12, 6.25, and 12.5 µm, respectively.

The simulation results for all the three mesh refinement levels agree well with the experimental data at early times as shown in Fig. 2.9(a), though the results for the coarser meshes deviate from the experimental data at later times. For example, the curve for $L = 9$ becomes different from the experimental data at about $(t - t_d)/\tau_{osc} > 4.6$. For the most refined case $L = 11$ ($\Delta_{\min} \approx 3$ µm and $R_d/\Delta_{\min} \approx 595$), the numerical and experimental results match remarkably well in the time range ($(t-t_d)/\tau_{osc} \lesssim 8$) considered in the present study, indicating that $L = 11$ is necessary and adequate to resolve the present problem.

A closeup of the eccentricity evolution for $0 < (t - t_d)/\tau_{osc} < 1$ is presented in Fig. 2.9(b), from which it can be observed that the simulation results agree with experiment not only for the large-scale variation set by the dominant second mode, but also for the small-scale variations induced by the high-order oscillation modes. The temporal evolution of the drop centroid position is shown in Fig. 2.10(a). The simulation and experiment results again match very well. Since the falling motion of the drop is coupled with the shape oscillation, the excellent agreement in high-level details between simulation and experiment for both eccentricity and drop trajectories fully validates the simulation results for both falling and oscillation dynamics of the

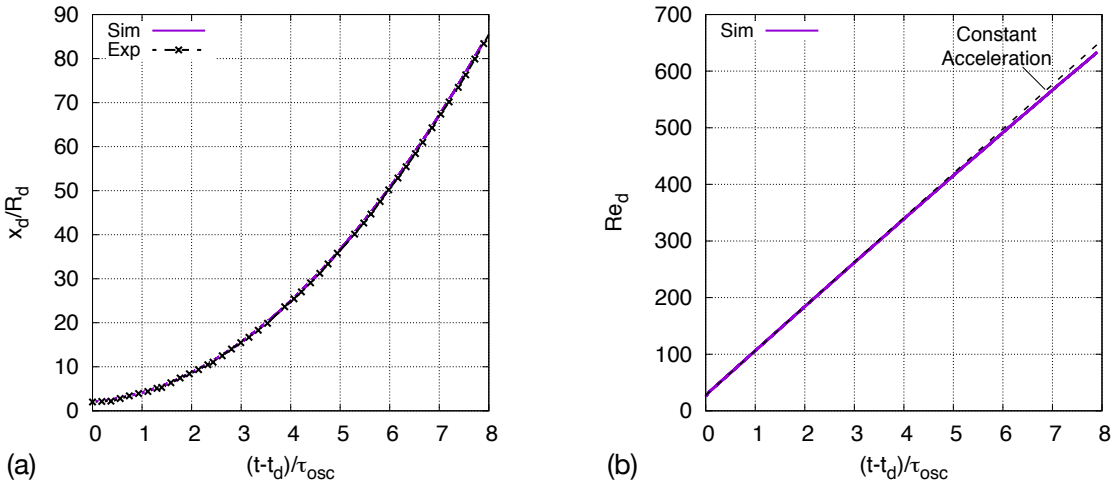


Figure 2.10. Temporal evolutions of the drop centroid $x$-position and Reynolds number $Re_d$.

drop. It also confirms that the axisymmetric approximation made in the present simulation is valid up to the time range considered.

The evolution of the drop velocity, plotted in dimensionless form as the drop Reynolds number, is shown in Fig. 2.10(b). A dashed line is given to indicate the evolution of Re when the drop falls with no aerodynamic drag, namely undergoes a constant acceleration. In the short term, it is clear that the aerodynamic drag is small compared to the gravity force. The Reynolds number increases almost linearly, though small discrepancy can be identified for $(t - t_d)/\tau_{osc} > 5$. The oscillation Reynolds number is $Re_{osc} = 1/Oh_{osc} = 360$. Initially $Re_d$ is smaller than $Re_{osc}$ but later overtakes and becomes larger than $Re_{osc}$. At $(t - t_d)/t_{osc} = 7.9$, the drop Reynolds number, $Re_d = 633$, is about 75% larger than $Re_{osc}$. Nevertheless, it is observed that the dominant oscillation frequency for the falling drop is still well predicted by Lamb's linear theory for a free drop.

### *2.4.2 Spherical Harmonic Mode Decomposition*

To better understand the shape oscillation of the falling drop, the instantaneous shape of the drop is decomposed into spherical harmonic modes (Basaran, 1992; Lalanne *et al.*, 2013). The temporal evolution and frequency spectra of the mode

Table 2.3. Results for the spherical harmonic mode analysis for the oscillation of the falling drop. The frequency $\omega_{n,Lamb}$ and damping rate $\beta_{n,Lamb}$ are calculated following the linear theory of (Lamb, 1932). The primary frequency $\omega_{n,sim}$ is measured through the frequency spectrum of the computed Fourier-Legendre coefficients $A_n$. The value of $A_n$ at $t = t_d$ is denoted by $A_{n,0}$, while the amplitude ($\alpha_n$) of the oscillation of $A_n$ at $t = t_d$ is represented by $\alpha_{n,0}$. The initial phase of the oscillation of $A_n$ is denoted by $\phi_n$. The values of $A_{n,0}$, $\alpha_{n,0}$ and $\phi_n$ are obtained from simulation results for drop formation. Exponential functions are used to fit the peaks and valleys of the temporal evolution of $A_n$ for $n = 2, 3$. The fitted initial oscillation amplitudes and damping rates for peaks and valleys are represented by $\alpha_{n,0,peak}$ and $\alpha_{n,0,valley}$, and $\beta_{n,0,peak}$ and $\beta_{n,0,valley}$, respectively.

| n | 2 | 3 | 4 | 5 | 6 | 7 | 8 | 9 | 10 |
|---|---|---|---|---|---|---|---|---|---|
| $\omega_{n,Lamb}$ ($s^{-1}$) | 292.3 | 566.1 | 877.0 | 1223 | 1601 | 2009 | 2446 | 2909 | 3397 |
| $\omega_{n,sim}$ ($s^{-1}$) | 306.8 | 552.2 | 859.0 | 1227 | 1595 | 2024 | 2454 | 2883 | 3436 |
| $\beta_{n,Lamb}$ ($s^{-1}$) | 1.44 | 4.05 | 7.80 | 12.7 | 18.8 | 26.0 | 34.4 | 43.9 | 54.6 |
| $A_{n,0}$ | 0.10 | 0.037 | 0.022 | 0.012 | 0.0066 | 0.0031 | 0.0011 | -0.00045 | -0.0014 |
| $\alpha_{n,0}$ | 0.144 | 0.0672 | 0.0393 | 0.0280 | 0.0210 | 0.0165 | 0.0135 | 0.0110 | 0.0092 |
| $\phi_n/\tau_2$ | 0.12 | 0.08 | 0.06 | 0.04 | 0.031 | 0.024 | 0.020 | 0.017 | 0.015 |
| $\beta_{n,peak}$ ($s^{-1}$) | 1.35 | 4.12 | - | - | - | - | - | - | - |
| $\beta_{n,valley}$ ($s^{-1}$) | 1.67 | 3.45 | - | - | - | - | - | - | - |
| $\alpha_{n,0,peak}$ | 0.148 | 0.0673 | - | - | - | - | - | - | - |
| $\alpha_{n,0,valley}$ | 0.141 | 0.0652 | - | - | - | - | - | - | - |

amplitudes will be presented to analyze the effects of the drop formation, the nonlinear dynamics, and the falling motion on the shape oscillation.

The shape of an axisymmetric drop can be described by the radius of the drop contour with respect to the centroid $R$ as a function of the colatitude $\theta$ (which is taken to be zero at the top of the drop), as shown in Fig. 2.9. For an oscillating drop, $R = R(\theta, t)$, and can be expanded as the superposition of spherical harmonic modes as

$$\frac{R(\theta, t)}{R_d} = \sum_{n=0}^{\infty} A_n(t) P_n(\cos(\theta)) \,, \tag{2.7}$$

where $P_n$ is the Legendre polynomial of degree $n$ and $A_n$ is the corresponding Fourier-Legendre coefficient, which represents the amplitude of the $n^{\text{th}}$ spherical harmonic mode. Assuming incompressibility, the drop volume is fixed and $A_0 = 1$. Furthermore, for the analysis of the falling drop, a reference frame moving with the drop velocity is used and the origin is set as the centroid of the drop. As a result, $A_1 = 0$. The temporal evolutions of $A_2$ to $A_{10}$ for the simulation results are shown in Fig. 2.11. A grid refinement study has been performed to confirm that the results presented are mesh independent, see appendix B.

The Fourier-Legendre coefficients at $t = t_d$ are denoted as $A_{n,0}$ and the values are listed in Table 2.3. The initial amplitudes for spherical harmonic modes generally decrease with the mode number $n$. The amplitudes of higher order modes ($n > 2$) are finite and cannot be ignored. For example, $A_{5,0}$ and $A_{7,0}$ are about 11% and 3% of $A_{2,0}$. The small-scale spatial variations in the drop contours near the top of the drop (see Fig. 2.6(c)), which are in turn induced by the pinching process, contribute to the finite amplitudes of the high order oscillation modes.

The frequency spectra of $A_n$ are shown in Fig. 2.12, from which the primary frequency for each mode can be identified. The values of the primary frequencies for simulation, $\omega_{n,sim}$, are given in Table 2.3. It can be seen that the oscillation frequency agrees well with the Lamb frequency. This conclusion is valid not only for the dominant $n = 2$ mode (as already shown in Fig. 2.9) but also for other modes

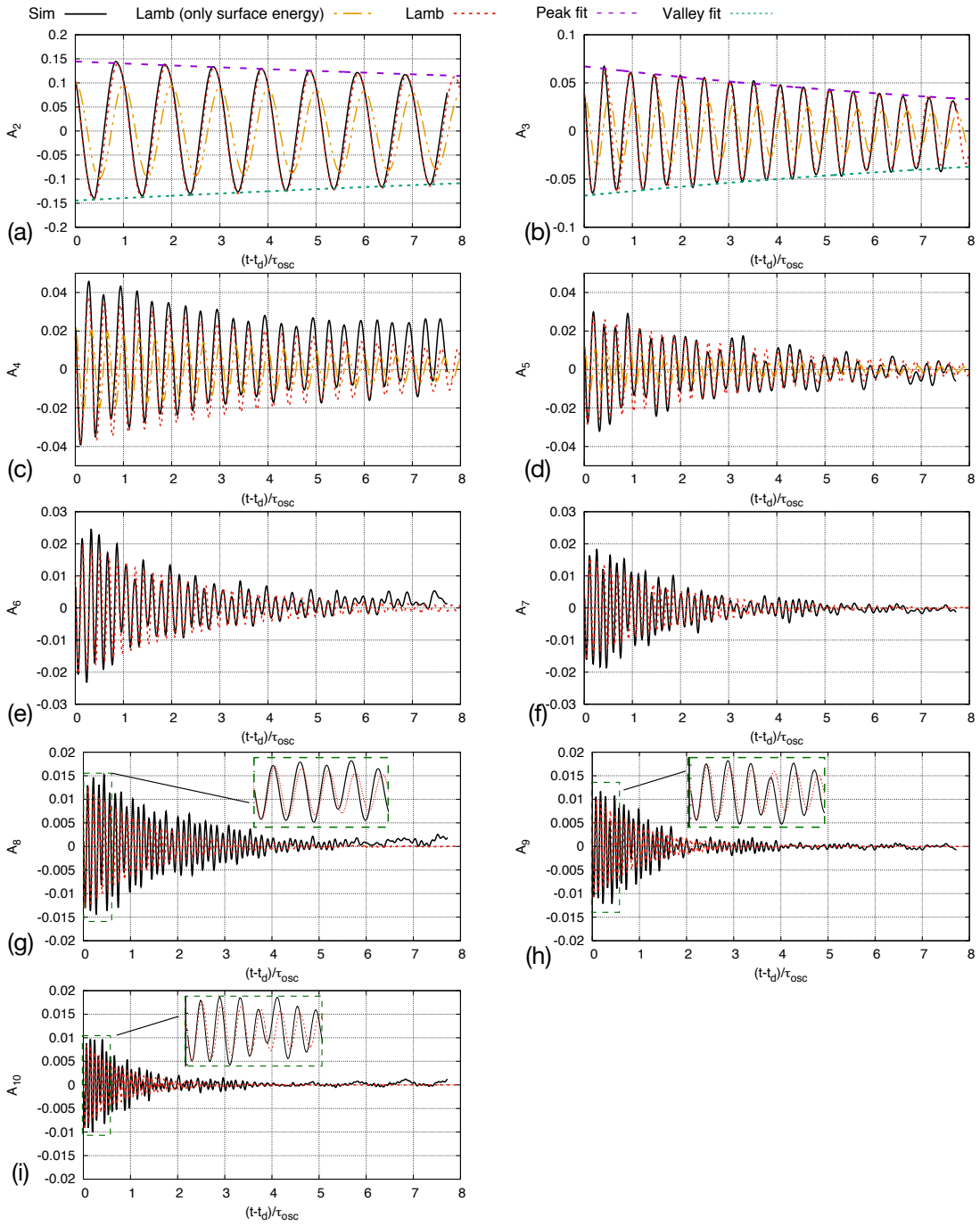


Figure 2.11. Temporal evolutions of the Fourier-Legendre coefficients, $A_n$, for different spherical harmonic modes, comparing the simulation results with the linear free-drop model based on the theory of (Lamb, 1932), with and without the initial kinetic energy. The exponential decay of the oscillation amplitudes for the peaks and valleys are also indicated in (a) and (b) for $n = 2$ and 3 modes.

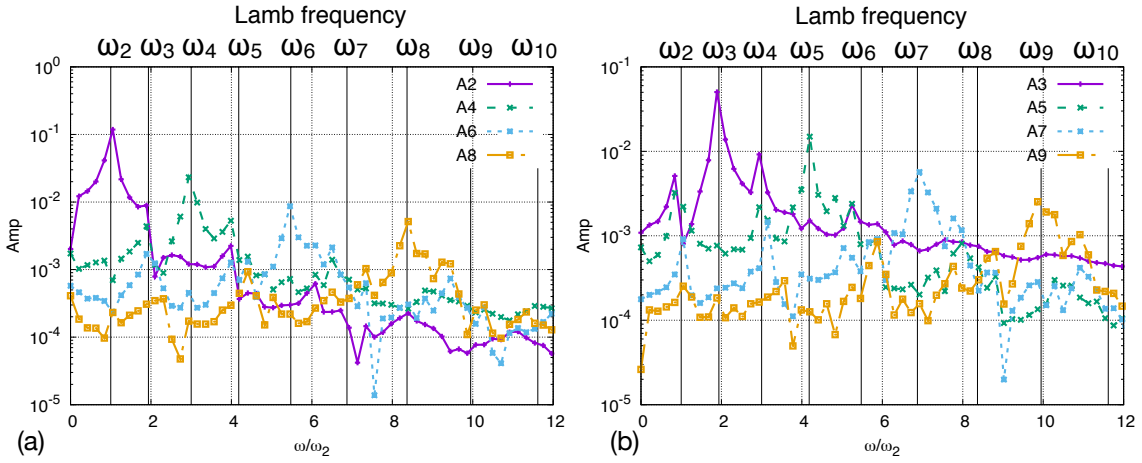


Figure 2.12. Frequency spectra of Fourier-Legendre coefficients for (a) even and (b) odd spherical harmonic modes, indicating the effect of mode coupling.

up to $n = 10$. It can be observed from Fig. 2.11 that, at the end of the simulation, $(t - t_d)/t_{osc} \approx 7.9$, the drop Reynolds number, $Re_d = 633$, is about 75% larger than $Re_{osc}$, yet the agreement with the Lamb frequency is still very good.

According to the nonlinear analysis of Tsamopoulos and Brown (Tsamopoulos and Brown, 1983), the leading term in the decrease of oscillation frequency due to finite amplitude is second order. For the dominant second mode, the initial amplitude $A_{2,0}$ is about 10%. The correction of frequency due to nonlinear effects is about 1%, which is quite small. This explains why the linear theory of Lamb (Lamb, 1932) remains a very good approximation for present case, even though the mode amplitudes are finite.

### *2.4.3 Linear Oscillation of a Free Viscous Drop*

The short-term oscillation of the drop is mainly controlled by the capillary effect; however, it is also significantly affected by the drop formation, the nonlinear dynamics due to finite oscillation amplitudes, and the falling motion. To better understand these effects on the oscillation dynamics, the simulation results are compared to the linear theory of Lamb (Lamb, 1932) for the linear oscillation of a free viscous drop.

The Fourier-Legendre coefficients for the n$^{th}$ Lamb mode, $A_{n,Lamb}$, are given as

$$A_{n,Lamb}(t) = \alpha_n \cos[\omega_{n,Lamb}(t + \phi_n)] \,. \tag{2.8}$$

For a viscous drop, the oscillation amplitude $\alpha_n$ decreases in time due to viscous dissipation. For small $Oh_{osc}$, the viscous damping effect causes an exponential decay of $\alpha_n$,

$$\alpha_n(t) = \alpha_{n,0} \exp(-\beta_{n,Lamb} t) \,, \tag{2.9}$$

where $\beta_{n,Lamb}$ is the damping rate, given by (Lamb, 1932) as

$$\beta_{n,Lamb} = \frac{(n-1)(2n+1)\nu_l}{R_d^2} \,. \tag{2.10}$$

Then Eq. (2.8) can be rewritten as

$$A_{n,Lamb}(t) = \alpha_{n,0} \exp(-\beta_{n,Lamb} t) \cos[\omega_{n,Lamb}(t + \phi_n)] \,. \tag{2.11}$$

It has been shown that the viscous damping influences the oscillation frequency as $\omega_n^{*2} = \omega_{n,Lamb}^2 - \beta_{n,Lamb}^2$. For the present problem $\beta_{n,Lamb} \ll \omega_{n,Lamb}$ (see Table 2.3), as a result, the decrease of frequency due to viscous effect is negligible. This also explains why the dominant oscillation frequency agrees so well with the Lamb frequency (Eq. (2.6)) as already shown in figure 2.9.

In Eq. (2.11), there are in total four parameters, $\omega_{n,Lamb}, \beta_{n,Lamb}, \alpha_{n,0}, \phi_n$. The frequency $\omega_{n,Lamb}$ and damping rate $\beta_{n,Lamb}$, as shown in Eqs. (2.6) and (2.9), depend only on the fluid properties. In contrast, the initial oscillation amplitude of the Fourier-Legendre coefficient, $\alpha_{n,0}$, and its the initial phase, $\phi_n$, are determined by the drop formation process and the resultant post-formation state, including both the shape (surface energy) and the velocity field (kinetic energy).

### *2.4.4 Effect of the Initial Kinetic Energy in the Drop*

Conventionally, the surface energy contained in the initial shape is assumed to dominate the initial state of drop oscillation and the initial kinetic energy (velocity

field) is usually ignored. The present study that covers both the drop formation and subsequent oscillation provides an opportunity to reexamine this assumption.

If the kinetic energy in the initial condition is ignored, *i.e.*, the velocity field is zero everywhere, or a static drop with the same shape as the post-formation drop is released, then $\alpha_{n,0} = A_{n,0}$ and $\phi_n = 0$ and Eq. (2.11) becomes

$$A_{n,Lamb,surf}(t) = A_{n,0} \exp(-\beta_{n,Lamb} t) \cos[\omega_{n,Lamb}(t)] \,. \tag{2.12}$$

The results of Eq. (2.12) for the first four modes ($n$ = 2 to 5) are plotted in Fig. 2.11. It is clear that the model including only the surface energy in the initial state yields results that are very different from the simulation results, even though the Fourier-Legendre coefficients for the exact initial shape of the drop, $A_{n,0}$, have been used. A close examination of Fig. 2.11(a) indicates that the deviation starts right at $t - t_d = 0$. The computed $A_2$ decreases faster and to a lower minimum than that predicted by the model. The decrease of $A_2$ represents that the drop deforms from the prolate (elongated) to the oblate (flattened) shapes. Therefore, the drop in simulation is flattened faster and to a larger extent compared to the model prediction. The discrepancy is due to the remaining effect of pinching dynamics and the non-uniformly distributed kinetic energy in the post-formation drop. As discussed above in section 2.3.3, the high pressure in the liquid bridge expels fluid toward the drop (which even induces overturning of the interface at the top of drop). As a consequence, when the drop is just detached from the liquid bridge, the top portion of the drop retains a significant downward velocity, which contributes to strengthening the prolate-to-oblate deformation, in addition to the capillary effect. The results clearly lead to the conclusion that the initial kinetic energy is as important as the initial surface energy to the shape oscillation and should not be ignored.

The key contributions of the initial kinetic energy to the shape oscillation are the amplification of $\alpha_{n,0}$ and the non-zero initial phase angle $\phi_n$. The values of $\alpha_{n,0}$ and $\phi_n$ for different modes can be obtained by fitting Eq. (2.11) with the simulation results near $t - t_d = 0$. As shown in Table 2.3, $\alpha_{n,0} > |A_{n,0}|$ and $\phi_n \neq 0$ are true

for all the modes considered here. The amplification of $\alpha_{n,0}$ and the non-zero initial phase angle due to drop formation were also observed in the experiments of Becker *et al.* (Becker *et al.*, 1991), though the physics behind them was not discussed. With the corrected $\alpha_{n,0}$ and $\phi_n$, Eq. (2.11) yields a much better agreement with the simulation results for the whole time range considered, see Fig. 2.11. (Hereafter, Eq. (2.11) with corrected values of $\alpha_{n,0}$ and $\phi_n$ is referred to as the linear free-drop model.) Considering the fact that the linear free-drop model still ignores the effects of falling motion and nonlinear dynamics, the agreement between the model and the simulation is quite impressive for the $n = 2$ and 3 modes.

In spite of the apparent good agreement between the linear free-drop model and the simulation results for the lower-order modes ($n = 2, 3$), significant differences exist in the higher-order modes ($n \geq 4$). At early time ($t \lesssim 5\tau_{osc}$) the falling velocity is small and thus the effect of the falling motion is negligible. The discrepancy is thus mainly due to the nonlinear effects, which are in turn triggered by the finite mode-amplitudes when the drop is formed. At later time, when the drop velocity becomes large, $Re_d > Re_{osc}$, the contribution of the falling motion to the discrepancy becomes significant. These two effects are discussed in sequence in the following sections.

### *2.4.5 Effect of Mode Coupling and Energy Transfer*

As summarized by Becker *et al.* (Becker *et al.*, 1991), typical nonlinear effects in shape oscillation include a) the dependence of the oscillation frequency on the amplitude, b) the asymmetry of the oscillation amplitude, and c) the coupling between modes. As shown in Fig. 2.9 the variation in frequency is small for the present case, however, the other two nonlinear effects can be clearly identified.

A close look at Fig. 2.11 shows that the oscillation amplitude of $A_n$ is generally asymmetric, namely the oscillation amplitudes corresponding to the peaks and valleys are different. The asymmetry of oscillation amplitude is most profound for the $n = 4$ mode: the temporal evolution of $A_4$ is clearly shifted upward, see Fig. 2.11(c). (A physical explanation for the strong nonlinear effect for the $n = 4$ mode is to be given

later.) Similar but less obvious upward shifting in the mode amplitude evolution can also be identified for the $n = 6$ and 8 modes. The asymmetric behavior is less obvious for the lower-order modes ($n = 2$ and 3). To better illustrate the asymmetric behavior, the exponential function (Eq. (2.9)) is used to fit the peaks and valleys of the temporal evolutions of $A_2$ and $A_3$. The fitted initial amplitudes and damping rates for the peaks and valleys are different as shown in Table 2.3. It is shown that $\alpha_{n,0,peak} > \alpha_{n,0,valley}$ for both $n = 2$ and 3 modes. For the damping rate, $\beta_{2,peak} < \beta_{2,valley}$ while $\beta_{3,peak} > \beta_{3,valley}$. The damping rate prediction of Lamb (Eq. (2.10)) lies in between the damping rates for the peaks and valleys. Due to the strong non-monotonicity in the decay of the oscillation amplitude for the higher-order modes, it is infeasible to fit the amplitude with an exponential function.

Another important nonlinear effect on drop oscillation is the interaction between different spherical harmonic modes through energy transfer. When energy is added or extracted from a specific mode, the oscillation amplitude of that mode will be amplified or suppressed, respectively. As a result, the decay of oscillation amplitude becomes non-monotonic, see Figs. 2.11 (d–i). It is conventionally considered that the nonlinear effects arise due to a large amplitude; however, it is observed here that the nonlinear effect is stronger for the higher-order modes ($n \geq 4$) than the lower-order modes ($n = 2, 3$) while the amplitudes of the former are actually smaller than of the latter. This interesting behavior has also been observed in experiments and can be explained through mode coupling (Becker *et al.*, 1991). For the present problem, the energy stored in the lower-order modes is significantly larger than that in the higher-order modes, see $\alpha_{n,0}$ values in Table 2.3. Therefore, when a small energy transfer between the lower-order and higher-order modes, its effect on the lower-order mode amplitude is small but it can modify the higher-order mode amplitude significantly.

Due to the large water-to-air density ratio in the present problem, the Lamb frequency is similar to the Rayleigh frequency

$$\omega^2_{n,Rayleigh} = \frac{(n-1)n(n+2)\sigma}{\rho_l R_d^3}\,. \tag{2.13}$$

An important feature of the Rayleigh frequency is that $\omega_2$ and $\omega_4$ are commensurate ($\omega_4 = 3\omega_2$), see Table 2.3. As a result, there exists a resonant effect in the coupling between the $n = 2$ and $n = 4$ modes (Tsamopoulos and Brown, 1983; Natarajan and Brown, 1987). As the $n = 2$ mode is the dominant mode that contains the most of the oscillation energy, the $n = 4$ mode is modulated significantly due to the resonant energy transfer between the two modes. This explains why the nonlinear effect is always the most intense for the $n = 4$ mode.

The effect of mode coupling is also shown in the frequency spectra of the spherical harmonic mode amplitudes $A_n$, see Fig. 2.12. While the linear free-drop model yields a single frequency for each mode, $\omega_{n,Lamb}$ (indicated by the vertical lines), the spectra of computed $A_n$ show multiple frequencies for modes $n > 2$. For the fundamental $n = 2$ mode, only the primary frequency $\omega_2$ is observed. (Other smaller peaks in the $A_2$ spectrum correspond to the even number times of the primary frequency, such as $2\omega_2$, $4\omega_2$, $6\omega_2$.) For a given mode $n > 2$, the spectrum shows a primary frequency that agrees well with $\omega_{n,Lamb}$, and also multiple secondary frequencies corresponding to other modes ($\omega_m$ with $m \neq n$) which interact with the $n^{th}$ mode. In the spectrum of $A_4$, secondary frequencies $2\omega_2$ and $4\omega_2$ are observed, (note the small difference between $4\omega_2$ and $\omega_5$,) which is further evidence for its strong coupling with the $n = 2$ mode. A close look indicates that the $A_6$ spectrum also shows similar secondary frequencies at $2\omega_2$ and $4\omega_2$. Former studies have shown that an initial second-mode deformation will excite even modes due to mode coupling (Tsamopoulos and Brown, 1983; Basaran, 1992). Therefore, though the coupling between the dominant $n = 2$ mode and other higher-order even modes like $n = 6$ is not as strong as with the $n = 4$ mode, their spectra also show the influence from the second mode.

Furthermore, a drop with initial finite-amplitude deformation of odd modes will transfer energy to the fundamental $n = 2$ mode and excite the oscillation of the latter (Basaran, 1992). In Fig. 2.12, a secondary frequency of $\omega_2$ is observed in the spectra of the odd modes $n = 3, 5, 7, 9$. Due to the resonant coupling between the $n = 2$

and 4 modes, the oscillation energy from the odd modes can also be transfered to the $n = 4$ mode through the intermediary $n = 2$ mode. As a result, the spectra of the odd modes also show a secondary frequency $\omega_4$. Finally, another commensurate relation exists between the $n = 5$ and 8 modes, namely $\omega_8 = 2\omega_5$, and therefore, there exists a resonant coupling between the two. That explains why a secondary frequency $\omega_8$ arises in the spectrum of $A_5$. It can be seen from Fig. 2.11 that, although the decay in oscillation amplitude is non-monotonic due to mode-coupling, the viscous damping rates are generally consistent with Lamb's prediction (see the results for the linear free-drop model). However, the $n = 8$ mode seems to be an exception; the decay of oscillation amplitude is slower than the linear free-drop model, which is due to the resonant coupling between the $n = 5$ and 8 modes.

### *2.4.6 Effect of Falling Motion*

The effect of the drop fall on the shape oscillation is initially small, yet as the drop falling velocity increases in time, its impact on drop oscillation is enhanced. The influence of the falling motion on the shape oscillation can be identified through the asymmetric oscillation amplitude. The asymmetric amplitude in $A_n$ (such as $n = 4$) for $(t-t_d)/\tau_{osc} \lesssim 4$ is due to the nonlinear effect. If the drop does not fall, then as the oscillation amplitude decreases with time, the nonlinear effect will become weaker and the level of asymmetry will also decrease over time. For the falling drop considered here, it is observed in Fig. 2.11(c) that the difference between the peak and valley amplitudes decreases initially but then remains at a similar level for $(t-t_d)/\tau_{osc} \gtrsim 4$. This is due to the interaction between the drop and the external flow induced by the falling motion. In the long term when the drop reaches its terminal falling velocity, (the drop can reach a fixed shape (Feng, 2010) or still oscillate (Helenbrook and Edwards, 2002) depending on $Re_{d,\infty}$ and $We_{d,\infty}$), the balance between surface tension and shear stress induced by the external flow results in a non-spherical equilibrium drop shape which exhibits non-zero mode amplitudes ($A_{n,eq} \neq 0$). Although the time period considered here is far from the equilibrium state, the shear stress induced by

falling motion already has an impact on the drop shape and enhances the asymmetry in oscillation amplitudes. The asymmetric effect is reflected as an upward shift of $A_n$ for the higher-order even modes ($n = 4, 6, 8, 10$) and is negligibly small for higher-order odd modes ($n = 5, 7, 9$). For the lower-order modes ($n = 2, 3$), the oscillation amplitudes are large and thus the capillary effect dominates. Therefore, the effect of falling motion is less profound.

There also exists an energy transfer between the falling motion and the shape oscillation. It can be observed from Fig. 2.11(c) that for $(t - t_d)/\tau_{osc} \gtrsim 4$, the oscillation amplitude decays much more slowly than the linear free-drop model. The energy dissipated by viscosity is compensated by the energy from the falling motion. Similar slower decay in oscillation amplitude for $(t - t_d)/\tau_{osc} \gtrsim 4$ can also be observed in Figs. 2.11(d–i) for other high-order modes.

## *2.5 Results for the Transient Flow Field*

The multi-mode oscillation of the falling drop is accompanied by a complex transient velocity field around the drop, see Fig. 2.13. The snapshot shown here is taken soon after the drop is formed, at $(t - t_d)/\tau_{osc} = 0.5$, from the simulation results. The inward and outward motions of the interface can be observed from the velocity vector field. The oscillating motion of the interface induces swirling motion of the fluid near the drop, which can be visualized by the vorticity ($\Omega$) field, as shown in the right half of figure 2.13.

### *2.5.1 Asymptotic Limits*

To better understand the development of the flow field for the falling and oscillating drop, we first look at the two asymptotic limits: 1) the case when the drop is freely oscillating but not falling, and 2) the case when the drop is falling but without oscillation.

A representative flow field around a freely oscillating drop is shown in Fig. 2.14(a). The simple case shown here contains only the second mode. As a response

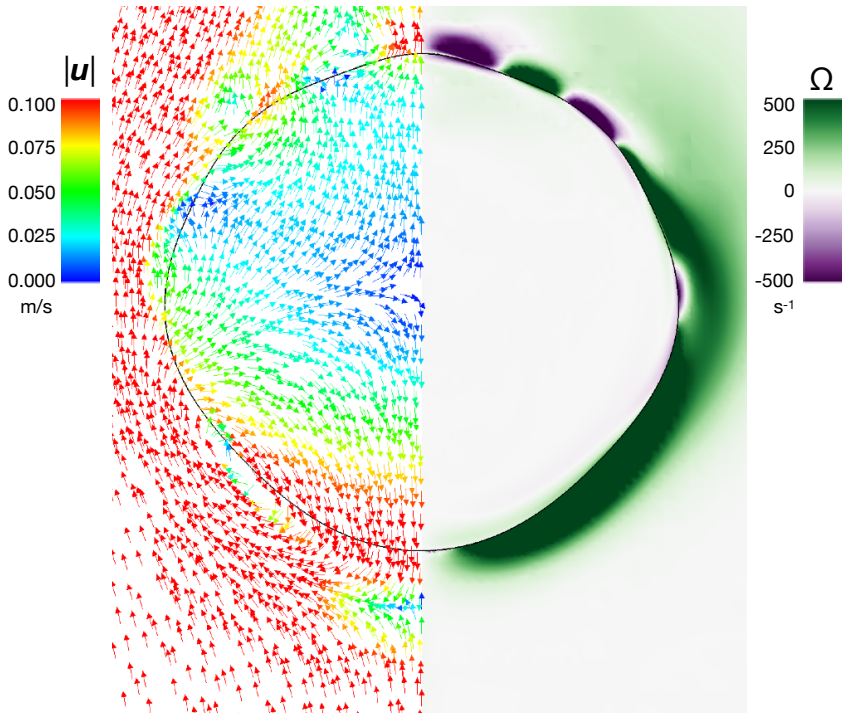


Figure 2.13. Simulation results for the velocity (left) and vorticity (right) fields around the drop at $(t - t_d)/\tau_{osc} = 0.56$.

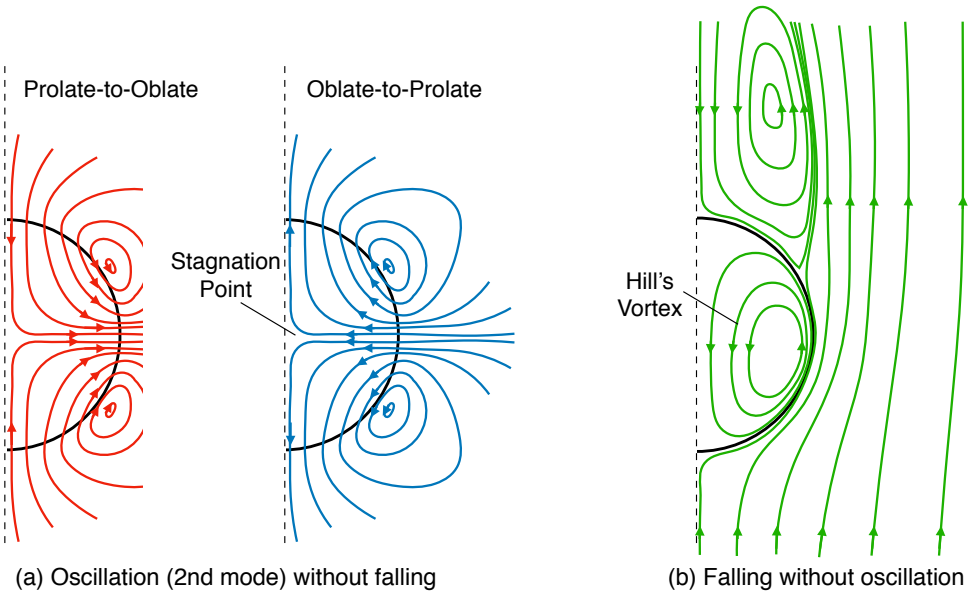


Figure 2.14. Schematics of the flow field for (a) a drop that is oscillating without falling motion, and (b) a drop that is falling without oscillation. Figure (a) is adapted from our simulation of a free drop undergoing only second mode oscillation. In figure (b) the streamlines are sketched based on the simulation results by (Feng, 2010) for $Re_d = 200$ and $We_d = 1$.

to the oscillation, two vortices are formed outside the drop with opposite rotation directions. The directions of the two vortices change within the oscillation cycle. When higher-order modes exist, more vortices will arise as can be seen in Fig. 2.13.

As the drop falls, it accelerates and the relative velocity between the drop and the surrounding air increases in time until the terminal velocity is reached. When the drop Reynolds and Weber numbers are small, the drop will eventually reach a steady state. For this limiting case where the drop is falling without oscillation, the internal flow pattern is dictated by the external shear. In the Stokes limit, the drop shape will remain spherical and the flow circulation inside the drop is known as Hill vortex (Hill, 1894). For finite but small Reynolds and Weber numbers, the drop will not be perfectly spherical but the internal flow remains similar to Hill vortex (Feng, 2010). A representative flow field for a falling drop without oscillation is shown in Fig. 2.14 (b), which is sketched based on the simulation results of Feng (Feng, 2010) for $Re_d = 200$ and $We_d = 1$. There exist only one vortex, similar to the Hill vortex, inside the drop.

### *2.5.2 Flow Patterns during one Oscillation Cycle*

The interplay between the falling motion and the shape oscillation creates a complicated transient flow which is different from either of the two limiting cases. The evolution of the flow is illustrated with streamlines in the drop reference frame in Fig. 2.15. Since the second mode is dominant, the temporal variation of the flow pattern generally follows the cycle of the second-mode oscillation. The time range covered in Fig. 2.15 is $(t - t_d)/\tau_{osc} \approx 5$ to 6, namely representing the sixth oscillation according to the second mode. The drop deforms from its prolate (elongated in $z$-direction) to oblate (flattened in $z$–direction) shapes in Figs. (a)-(c), reaching the most oblate shape at $(t - t_d)/\tau_{osc} \approx 5.30$. Then the drop returns back to the prolate shape from (c)–(g), until a new cycle starts.

When the drop deforms from the prolate to the oblate shapes, see Figs. 2.15(a)-(b), the streamlines inside the drop are quite similar to those for the second-mode

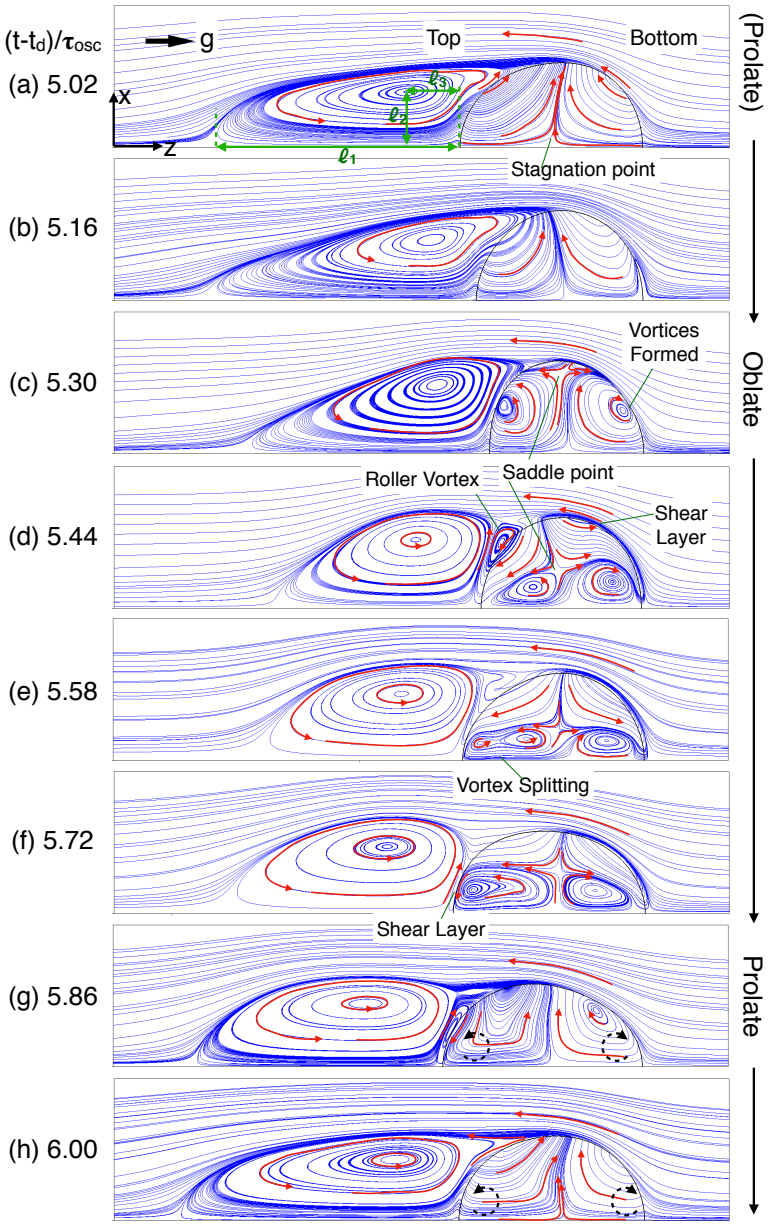


| $\frac{(t-t_d)}{\tau_{osc}}$ | $Re_d$ | e | $\frac{\ell_1}{R_0}$ | $\frac{\ell_2}{R_0}$ | $\frac{\ell_3}{R_0}$ |
|---|---|---|---|---|---|
| 5.02 | 416 | 1.17 | 2.74 | 0.64 | 0.59 |
| 5.16 | 428 | 0.96 | 2.95 | 0.67 | 0.53 |
| 5.30 | 438 | 0.86 | 2.68 | 0.77 | 0.59 |
| 5.44 | 449 | 0.84 | 2.25 | 0.77 | 0.75 |
| 5.58 | 459 | 0.99 | 2.20 | 0.75 | 0.69 |
| 5.72 | 470 | 1.12 | 2.47 | 0.75 | 0.75 |
| 5.86 | 481 | 1.21 | 2.79 | 0.69 | 0.86 |
| 6.00 | 492 | 1.16 | 3.11 | 0.69 | 0.75 |

Figure 2.15. Flow field near the oscillating and falling drop for $(t-t_d)/\tau_{osc}$ from 5 to 6. The characteristic length scales for the wake geometry, including the wake length $l_1$, the distance between the wake-vortex center and the axis $l_2$, and the distance between the wake-vortex center and the top of the drop $l_3$, are measured.

free oscillation. A stagnation point is formed when the fluid moves from the two poles toward the center. In the ground reference frame, the fluid velocity at that stagnation point is identical to the mean falling velocity of the drop. A close examination further shows that the stagnation point does not generally overlap with the centroid. In this time range, the external flow going over the drop is already strong enough to overcome the rotational flow induced by drop oscillations, therefore, the vortices outside the drop that are seen in the free oscillation (see Fig. 2.14(a)) become invisible. At the colatitude $\theta$ about 45 and 135 degrees, the streamlines inside the drop align well with those outside. The internal flow corresponding to the prolate-to-oblate oscillation is enhanced by the external flow.

After the drop reaches the most oblate shape and starts to deform back (Figs. 2.15(c)-(g)), the internal flow field becomes very different from that for the free oscillation shown in Fig. 2.14(a). For the freely-oscillating drop, while the drop deforms from the oblate to the prolate shapes, the flow moves from the lateral side to the the stagnation point and then bifurcates toward the two poles (see Fig. 2.14(a)). However, for the falling drop, as the original internal flow due to prolate-to-oblate oscillation is strengthened by the external flow, the oblate-to-prolate oscillation fails to reverse flow direction near the stagnation point. Indeed, the flow direction near the stagnation point does not change through the oscillation cycle. While the interface at the lateral side of the drop retracts toward the axis, the flow near the stagnation point still tries to move toward the lateral side. As a consequence, a saddle point (a saddle curve due to the axisymmetric geometry) is formed, which in turn induces two vortices (vortex tubes in the axisymmetric geometry) within the drop, see Fig. 2.15(c).

As the drop continues to deform towards the prolate shape, the saddle point is further pushed toward the $z$–axis, so are the two vortices. Furthermore, as the internal circulations near the top and bottom of the drop are not aligned with the wake and the external flow, see Fig. 2.15(d), roller vortices are formed outside the

drop (Bergeles *et al.*, 2018). When the drop becomes more prolate, the two vortices inside are further flattened. At a certain point, see Fig. 2.15(e), the internal vortex near the top of the drop splits into two.

After reaching the most prolate shape, the drop starts to deform back toward the oblate shape. In this process, as shown in Fig. 2.15(g), the two vortices inside the drop near the axis become invisible. However, they still exist, as will be shown later with vortex-identification techniques. It is just that the potential flow induced by the drop oscillation is so strong that, the local swirling motion cannot be shown by streamlines. Two new transient vortices are formed inside the drop near the lateral side, which vanish very soon. Then the internal flow pattern returns to the form similar to the beginning of the cycle.

Within the time range considered the drop oscillation is still quite strong, *e.g.*, the second-harmonic-mode amplitude remains larger than 0.1 as shown in Fig. 2.11. As a result, the fluid inertia due to oscillation plays a significant role in the transient flow inside the drop. It is important to note that the internal flow pattern observed here is substantially different from Hill vortex, which corresponds to the long-term behavior when the drop oscillations are damped. In particular, the two vortices formed during the oblate-to-prolate process rotate in opposite directions compared to the corresponding external flows. Roller vortices are then formed in between the internal and external flows to satisfy the fluid kinematics.

The formation of the saddle point during the oblate-to-prolate deformation is an important feature, which is due to the different directions of the flows induced by the external shear and the shape oscillation. Therefore, the Strouhal number, $Sr = u_{osc}/u_{ic}$, can be defined to characterize the formation of the saddle point, where $u_{osc}$ and $u_{ic}$ represent the characteristic velocities for the internal flows induced by the shape oscillation and by the external flow, respectively. While $u_{osc}$ can be estimated as $u_{osc} \approx a_2\omega_2$, where $a_2 = A_2R_d$ and $\omega_2$ are the oscillation amplitude and frequency corresponding to the dominant second mode, $u_{ic}$ can be approximated as $u_{ic} \approx u_d\nu_{ic}$,

where $\nu_{ic}$ is the internal circulation intensity (Feng, 2010). The Strouhal number can be rewritten as $Sr = a_2\omega_2/(u_d\nu_{ic})$. When $Sr \to 0$, the droplet falls without oscillation (see Fig. 2.14(b)). When $Sr \to \infty$ the drop oscillates without translational motion (see Fig. 2.14(a)). For both these asymptotic limits, there is no saddle point in the flow. The saddle point will arise only when $Sr \sim O(1)$, namely when $u_{osc}$ and $u_{ic}$ are comparable.

### *2.5.3 Wake Topology Evolution*

The characteristic length scales for the wake geometry, including the wake length $l_1$, the distance between the wake-vortex center and the axis $l_2$, and the distance between the wake-vortex center and the top of the drop $l_3$, are measured over an oscillation cycle $(t - t_d)/\tau_{osc} = 5$ to 6 and are shown in Fig. 2.15. The simulation results show that the wake length $l_1$ generally increases over time, which is consistent with former observations by Bergeles *et al.* (Bergeles *et al.*, 2018). At $(t-t_d)/\tau_{osc} = 5$ and 6, the drop eccentricity, $e$, are the same, while the wake length increases from $l_1/R_0 = 2.74$ to 3.11 due to increasing $Re_d$. The values here are larger than those obtained by Bergeles *et al.* (Bergeles *et al.*, 2018) because of the larger $Re_d$. At $(t - t_d)/\tau_{osc} = 5$, $Re_d = 416$ and $l_1/R_0 = 2.74$, compared to $l_1/R_d = 2.2$ for the maximum $Re_d = 273$ in the former study (Bergeles *et al.*, 2018).

Furthermore, due to the higher resolution in the present simulation, variation of $l_1$ following the dominant second mode oscillation is observed, which was not shown in the former study (Bergeles *et al.*, 2018). It can be shown that $l_1$ decreases when the drop deforms from prolate to oblate shapes, and increases when the drop returns back to the prolate shape. There exits a small time lag between the temporal variation of $l_1$ and $e$ due to the inertial effect. Here $e$ reaches the local minimum at about $(t - t_d)/\tau_{osc} = 5.44$ while $l_1$ does not get to the local minimum until about $(t-t_d)/\tau_{osc} = 5.58$. The distance between wake-vortex center and the top of the drop $l_3$ also generally increases over time similar to $l_1$, though the increase is more gradual. As a result, its variation within the time range shown in Fig. 2.15 is mainly dictated

by the drop oscillation. The amplitude increase of $l_2$ over a cycle is also small, similar to $l_3$. The difference between $l_2$ and $l_3$ is that $l_2$ is large when the drop is oblate and is reduced when the drop turns back to the prolate shape. This is because when the drop deforms toward the oblate shape, the wake-vortex center is also pulled toward the lateral side.

### *2.5.4 Vortex Dynamics*

It is well known that streamlines are insufficient to fully identify vortices. Galilean invariant flow properties must be used instead. The swirling-strength vortex-identification criterion (Zhou *et al.*, 1999), also known as $\lambda_{ci}$-criterion, is employed here to illustrate the evolution of vortices, see Fig. 2.16. The $\lambda_{ci}$-criterion has been shown to be an effective way to visualize vortices (Zhou *et al.*, 1999; Chakraborty *et al.*, 2005). The vorticity, which cannot fully identify the vortices as $\lambda_{ci}$ (since $\lambda_{ci}$ excludes the contribution from strain), is also plotted here to indicate the rotation directions of vortices. The vortex rotation directions are clockwise and counter-clockwise for $\Omega < 0$ (purple color) and $\Omega > 0$ (green color) on the right half of the drop, respectively.

The figures are organized in such a way that the six rows represent the first, third, fourth, fifth, sixth and seventh oscillations based on the dominant second mode (see Fig. 2.9), as reflected by the time normalized by the dominant second-mode period, $\tau_{osc} = \tau_2$.

For the first row of the figure, the drop relative velocity is small and the effect of the falling motion is negligible. The multiple small vortices outside the drop are generated due to higher-order oscillation modes (see also the velocity field in Fig. 2.13). As time elapses, the amplitudes of the oscillations decrease in time due to viscous dissipation of the internal flow. It is shown in Fig. 2.11 that the decay rate is faster for the higher-order modes. As a result, the small vortices outside the drop disappear in the second row of Fig. 2.16. Only the larger vortices corresponding to the lower-order modes (*e.g.*, $n \leq 3$) survive.

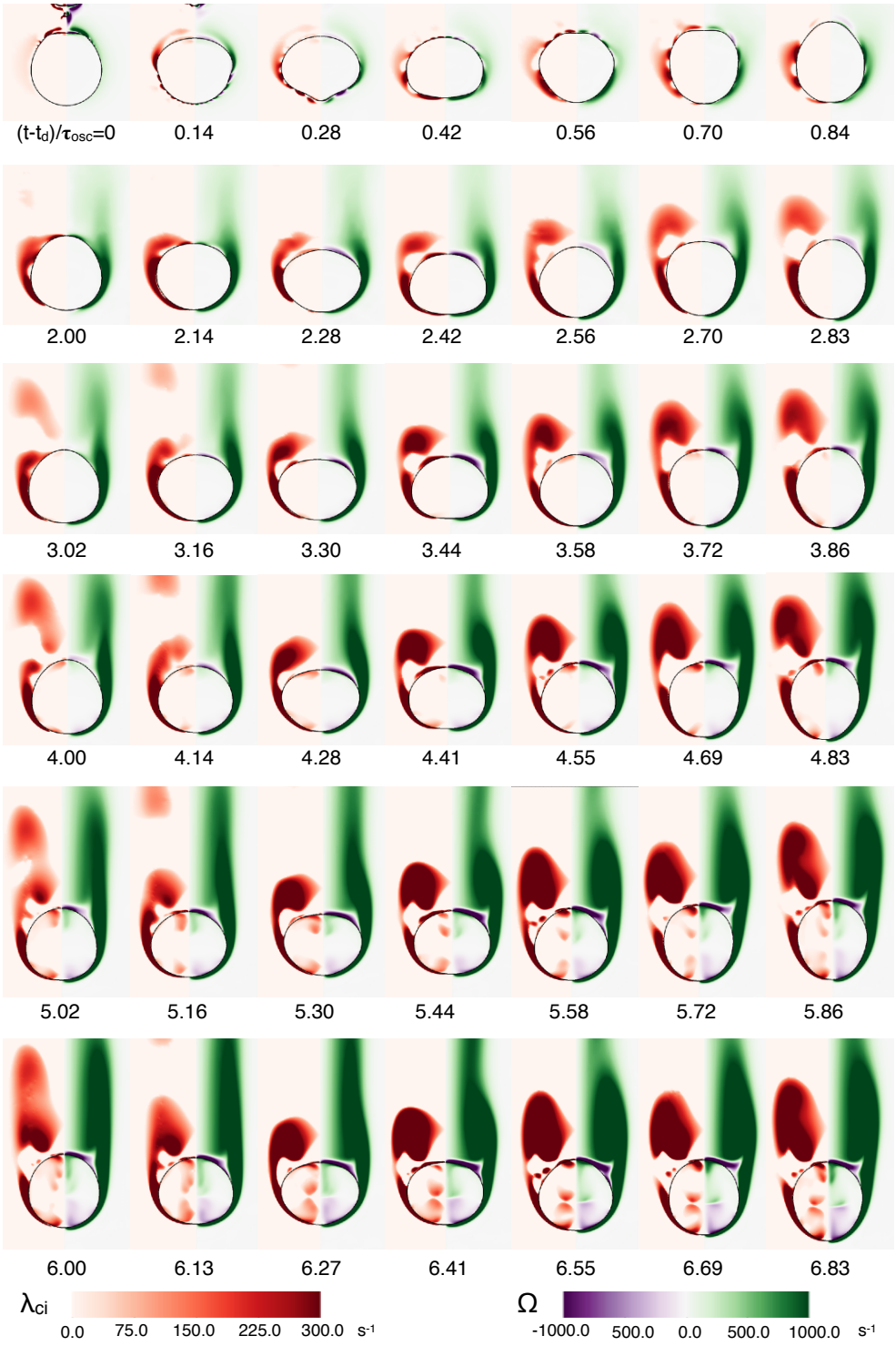


Figure 2.16. Evolution of $\lambda_{ci}$ (left) and vorticity (right) for the dripping drop. The vortices are visualized by the $\lambda_{ci}$ criterion.

In the first two rows (the first three second-mode oscillations), there is no vortex seen inside the drop. As the falling velocity continues to increase, the influence of the external flow becomes stronger and vortices inside the drop start to arise, at about the middle of third row of Fig. 2.16, $(t - t_d)/\tau_{osc} \approx 3.5$. As explained above, the formation of vortices inside the drop occurs when the drop deforms from oblate to prolate shapes and is the outcome of the interaction between drop shape oscillation and the external flow. The two internal vortices near the top and the bottom rotate in different directions, as indicated by the different colors in the vorticity plots.

It can be seen from Fig. 2.10 that the drop Reynolds number reaches 190 at $(t - t_d)/\tau_{osc} \approx 2$ and the wake developing at the downstream side of the drop can be seen from the second row of Fig. 2.16. From the subsequent rows of the figure, it can be observed that the shape and relative location of the wake vortex change periodically following the dominant second-mode oscillation.

An important observation from the $\lambda_{ci}$ plots is that the vortices inside the drop indeed remain even when the drop shape changes from prolate to oblate, even though they are invisible in the streamline plots as shown in Fig. 2.15. The potential flow induced by the prolate-to-oblate oscillation is strong and dominates the streamline pattern. Therefore, though local swirling motions exist, they can only be shown by Galilean-invariant vortex-identification scalars like $\lambda_{ci}$. From the vorticity plots, it is learned that the rotation directions of the internal vortices do not change over an oscillation cycle, even though the potential flow direction changes in the second-mode oscillation cycle, see Fig. 2.15. On the right half of the figure the top vortex always rotates in counter-clockwise direction, while the bottom one swirls in the clockwise direction all the time.

Closeups of the vortices with annotations are shown in Fig. 2.17. The topology of the vortices inside the drop changes within an oscillation cycle. When the drop deforms toward the prolate shape, the vortices are stretched and can even split into two pieces. During the oblate-to-prolate deformation, the vortices at the lateral side

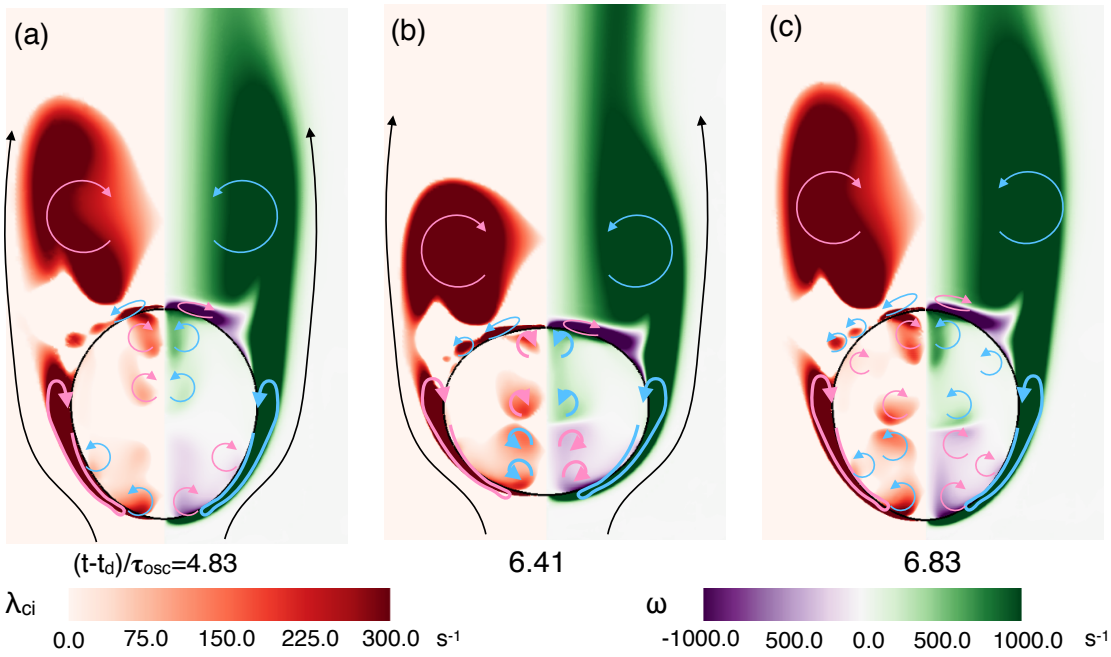


Figure 2.17. Closeup of the vortices formed around the drop. Annotations are added to indicate the rotation direction.

are pushed toward the axis and will eventually merge with the ones which are already there.

### *2.5.5 A Summary of Transient Flow Development inside the Drop*

With the assistance of both the streamlines and contours of $\lambda_{ci}$ and vorticity, the development of the transient flow and the vortices' interaction inside the drop can be described as follows:

(1) The internal flow induced by prolate-to-oblate oscillation is aligned and enhanced by the external flow.

(2) As the falling velocity increases, at a certain point, the oblate-to-prolate deformation fails to fully reverse the internal flow induced by its prolate-to-oblate counterpart.

(3) Then a saddle point (curve) arises inside the drop when the drop deforms from its most oblate shape toward the prolate shape.

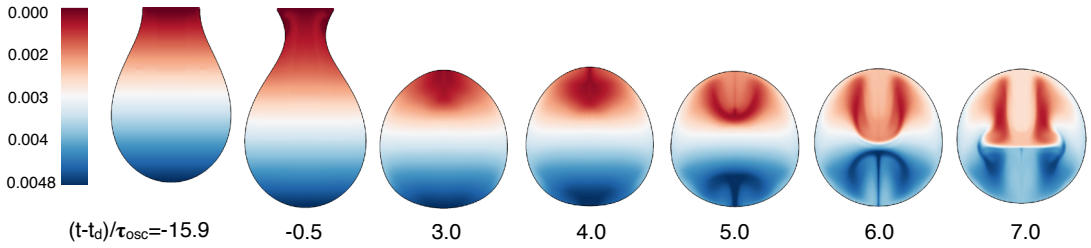


Figure 2.18. Evolution of the tracer function distribution.

(4) The saddle point induces two vortices rotating in different directions inside the drop.

(5) As the internal circulations are different from the external flows, roller vortices are formed to satisfy kinematics.

(6) As the drop continues to deform toward its most prolate shape, the two vortices are pushed toward the axis. (If there are vortices already near the axis, the new ones will merge with the old ones.)

(7) The vortices near the axis will be stretched and may split when the drop deforms toward the prolate shape.

(8) When the drop deforms back to the prolate shape, the two vortices remain present and the rotation directions do not change.

(9) Going back to (3) and a new cycle starts.

### *2.5.6 Passive Scalar Transport within the Drop*

It is of interest for many drop applications to know the influence of the transient flow within an oscillating drop on scalar transport inside the drop. The question of interest is whether mixing will occur if inhomogeneous fluids are injected into the drop through the nozzle. Although mixing of different fluids inside the drop is not the focus of the present study, here a passive tracer function is introduced in the simulation to illustrate the transport process within the drop. The initial value of the

tracer function is set as the streamwise coordinate $z$. The evolution of the tracer field serves to reveal the accumulation effect of the transient internal flow development described above on scalar transport.

The advection equation of the tracer function is only solved within the liquid phase. The Godunov advection scheme with the second-order centered estimate for the velocity gradient was used. There exists a small numerical diffusion, but due to the fine mesh used, the numerical diffusion effect on the advection process is small. The results of the tracer function at different times are shown in Fig. 2.18. Before the drop detaches from the nozzle, the tracer function only varies with $z$. The tracer function here can be considered to mimic an imaginary experiment in which the fluid fed in the nozzle is dyed sequentially with blue, white, and red colors. When the neck of the pendant drop develops, the tracer function is redistributed by the vortex ring created by the Ventruri jet through the neck (Hoepffner and Paré, 2013). The tracer function in the lower part of the drop remains unchanged.

The snapshots of the drop after detachment are chosen to exhibit similar eccentricity, namely similar phases in the second-mode oscillation. When the drop simply oscillates at early time ($0 < (t - t_d)/\tau_{osc} < 3$), the tracer function distribution varies only in $z$, similar to the initial distribution. The shape oscillation by itself may introduce longitudinal motion (for example by the odd modes), but will not lead to net longitudinal transport of the tracer function. This is simply because the fluid motion induced by small-amplitude oscillation is symmetric and after one oscillation cycle the scalar function distribution will return to its original state. As the falling velocity increases, the external flow develops and interacts with the drop oscillation. Vortices arise inside the drop and they translate and interact following the drop oscillation cycle. Then stretching and folding of the fluids of different tracer function values are observed. As the top and bottom circulations are of different directions, the folding directions of the red and blue fluids are different. Though the fluids are "mixed" inside the top and bottom portions of the drop, the two portions remain segregated

most of the time. At later time, however, more complex distorted patterns of the tracer function arise, which is due to the unsteady motion of the saddle point (see Fig. 2.15(c–f)). If the simulation was run for a longer time to allow more oscillation cycles, chaotic mixing (Aref and Balachandar, 1986; Angilella and Brancher, 2003) of inhomogeneous fluids may arise. More detailed investigation of transport phenomena will be left for our future work.

## *2.6 Conclusions*

The short-term transient falling dynamics of a dripping water drop has been studied. One specific case with a low inflow rate in the dripping regime is considered. The focus is on the short term behavior and the time range considered covers about eight dominant second-mode oscillations of the drop after it is formed. A high-resolution numerical simulation has been performed to investigate the oscillation and falling dynamics. An experiment under the same conditions was also conducted for validation purposes. The grid-refinement study and the excellent agreement between simulation and experiment/theory verify and validate the simulation results. Despite the low fluid inertia, the post-formation state of the drop still triggers a nonlinear oscillation. To rigorously account for the effect of drop formation on shape oscillation, the overall process including the drop growth, pinch-off, and fall, is studied. The interaction between the shape oscillation and the falling motion introduces complex oscillation dynamics and transient flow around the drop.

### *2.6.1 Drop Formation*

The experimental results for the growing pendant drop, such as the relation between drop height and volume, agree well with the static pendant drop theory, which confirms that the drop development process is quasi-static and can be fully described by the static theory. This justifies the way the simulation is setup by using the static pendant drop solution slightly ahead of the pinch-off time as the initial condition in the simulation. The computed drop contours for the drop growth and

formation match very well with the experimental results, validating the setup of the numerical model. Though pinching dynamics is not the focus of the present study, evolutions of the velocity and pressure fields are presented to illustrate important features for low-viscosity liquid drop formation, including the shifting of the minimum radius to the two ends of the liquid bridge, the interface overturning before pinch-off occurs, and the formation of the secondary drop. The temporal evolution of the liquid bridge minimum radius shows an initial inertial regime ($(t_d - t)^{2/3}$ power law) which later transitions to the viscous regime ($(t_d - t)^1$ linear law). The results affirm that the drop formation is precisely captured.

### *2.6.2 Effect of Drop Formation on Drop Oscillation*

The post-formation state serves as the initial condition for the subsequent oscillation of the drop. The initial shape of the drop when it is just formed is decomposed into spherical harmonic modes. The initial mode amplitudes, characterized by the Fourier-Legendre coefficients, are found to be finite for the modes $n \leq 10$ considered. The pinching dynamics such as interface overturning introduces small-scale variation on the drop contour, which in turn contributes to the finite amplitudes of the higher-order modes. Furthermore, during the pinching process the high pressure in the neck expels fluids toward the to-be-formed drop, which leads to a significant downward velocity in the top region of the drop when it is just detached. The initial kinetic energy is as important as the initial surface energy contained in the drop shape, and is found to amplify the initial oscillation amplitude and to induce a phase shift in the oscillation of all the modes. By incorporating both the initial surface and kinetic energy, the linear model for a free drop oscillation yields very good predictions for the second and third modes.

### *2.6.3 Effect of Nonlinear Dynamics on Drop Oscillation*

The post-formation state of the drop triggers a moderately nonlinear drop oscillation. The oscillation amplitude for the dominant second mode is about 10%, so the

influence of finite amplitude on oscillation frequency is small for all the modes considered here. Nevertheless, typical nonlinear effects including asymmetry in oscillation amplitude and interaction between different modes are identified. The nonlinear effects are more profound for higher-order modes ($n \geq 4$) than lower-order modes ($n = 2, 3$). Since the majority of energy is stored in the lower-order modes, the small energy transfer between modes may be significant for the higher-order modes but will have little impact on the lower-order modes. Mode coupling is clearly reflected in the frequency spectra of the Fourier-Legendre coefficients. In the spectrum of a given mode $n$, a primary frequency that is very similar to the Lamb frequency can be identified. Furthermore, the spectrum shows secondary frequencies corresponding to different modes due to mode coupling. Due to the low viscosity of water, there exists a commensurate relation between the $n = 2$ and 4 modes, which explains why nonlinear effects are always strongest for the $n = 4$ mode.

### *2.6.4 Effect of Falling Motion on Drop Oscillation*

The present results indicate that the effect of the fall on the oscillation frequency is little for the time range considered here. The oscillation frequency for the falling drop agrees well with Lamb's prediction even when the drop Reynolds number is 75% higher than the oscillation Reynolds number. This conclusion is true for both lower and higher order modes. The effect of the drop fall on shape oscillation lies mainly in the time evolution of the amplitudes of the various shape oscillation modes. The increasing shear stress induced by the falling motion changes the force balance with surface tension, resulting in a strengthened upward shift in oscillation amplitude for the higher-order even modes. The drop falling motion also seems to provide energy to the oscillations, and as a result, the damping in amplitude is slowed down for $(t - t_d)/\tau_{osc} \gtrsim 4$.

### *2.6.5 Effect of Drop Oscillation on Transient Flow Development*

When the drop falls without oscillation, the external shear induced by the falling motion will induce the Hill vortex within the drop. For the present case, nonlinear shape oscillation interacts with the external flow induced by the falling motion, resulting in a complicated transient flow around the drop. When the drop oscillates from prolate to oblate shapes, the flow induced by the oscillation is aligned with the external flow. In contrast, for a oblate-to-prolate deformation, the flow goes against the external flow. As a result, a saddle point (curve for the axisymmetric geometry) arises in the drop, which gives rise to two counterrotating vortices. The rotating directions of the vortices remain unchanged, while the potential flow directions vary due to the dominant second-mode oscillation. The drop oscillation also influences the wake geometry. The swirling-strength vortex-identification criterion ($\lambda_{ci}$) and the vorticity are employed to better elucidate the vortex dynamics. When the drop oscillates, the vortices inside can be stretched and even split. Finally, a tracer function is introduced to demonstrate the scalar transport within the drop. Pure shape oscillation does not induce net longitudinal transport of the tracer function. Stretching and folding of the scalar function contours are only observed after vortices arise within the drop. The unsteady motion of the saddle point creates a more distorted tracer function field, which may result in a chaotic mixing of inhomogeneous fluids inside the drop. Yet a longer simulation than the present one will be required to fully verify this.

# CHAPTER THREE

## Modeling and Detailed Numerical Simulation of the Primary Breakup of a Gasoline Surrogate Jet under Non-Evaporative Operating Conditions

### *3.1 Introduction*

A comprehensive understanding of the injection and atomization of gasoline fuels is essential to improving the fuel injection systems in gasoline direct injection (GDI) engines. The characteristics of the droplets formed in the atomization process have a direct impact on the subsequent turbulent dispersion of droplets, droplet evaporation, mixing between the fuel vapor and the air, and eventually combustion features like spark ignition and flame propagation in engines (Zhao *et al.*, 1999). Due to the increasing demand for high fuel efficiency and low pollutant emission, extensive research efforts have been directed toward understanding and predicting the atomization of gasoline jets and the resulting spray characteristics in the past decades (Mitroglou *et al.*, 2006; Wang *et al.*, 2015; Duke *et al.*, 2017; Khan *et al.*, 2017; Sphicas *et al.*, 2018; Payri *et al.*, 2017). For the purpose of advancing the understanding of gasoline spray formation, the Engine Combustion Network (ECN) has developed the benchmark "spray G" injector and operating conditions. ECN has also provided a rich experimental database for numerical model validation. In the present study we will develop a numerical model for a gasoline non-evaporative surrogate jet under the spray G operating conditions and investigate the primary breakup of the liquid jet.

The breakup or atomization of a liquid jet is usually divided into the primary and secondary breakup/atomization processes: while the former refers to the disintegration of bulk liquid jets into droplets and ligaments, the latter describes the breakups of large droplets and ligaments to even smaller ones. The primary and secondary breakups can happen simultaneously and the boundary between the two

processes is often blurry. The primary breakup typically dominates in the near field and the secondary breakup appears mostly in the mid/far field. The primary breakup of a liquid jet is a problem of enormous complexity and involves multiple physical processes occurring in a wide range of spatial scales (Reitz and Bracco, 1982; Lin and Reitz, 1998; Aleiferis *et al.*, 2010). This multi-scale nature makes the investigation of primary breakup challenging. Furthermore, the flow of the liquid fuel inside the injector (*i.e.*, the so-called internal flow) can also affect the breakup dynamics of the liquid jet outside the nozzle (Payri *et al.*, 2016; Agarwal and Trujillo, 2020), which further complicates the problem. Experiments have been the major approach to investigate gasoline injection in the past (Mitroglou *et al.*, 2006; Duke *et al.*, 2017; Aleiferis *et al.*, 2010). However, even with the most advanced optical and X-ray diagnostics, there remain two-phase flow features that are hard to measure in experiments. This is in particular true for the near field where the primary breakup happens (Heindel, 2018). As a result, numerical simulation is an important alternative to shed light on the underlying flow physics (Gorokhovski and Herrmann, 2008).

Due to the wide range of length scales involved in liquid fuel injection and atomization, a direct numerical simulation (DNS) that can fully resolve all the scales is generally too expensive. The recent rapid development of numerical methods and computer power has enabled large-scale numerical simulations of the primary breakup of a liquid jet (Fuster *et al.*, 2009; Lebas *et al.*, 2009; Desjardins and Pitsch, 2010; Shinjo and Umemura, 2010; Li and Soteriou, 2016; Ling *et al.*, 2017; Shao *et al.*, 2017; Ling *et al.*, 2019; Hasslberger *et al.*, 2019). These simulations adopt the DNS approach, namely solving the Navier-Stokes equations for the interfacial two-phase flows without explicit physical models. Interface-capturing methods, *e.g.*, the volume-of-fluid (VOF) and the level-set methods, were used to resolve the sharp interfaces separating the two immiscible fluids. Ideally, the mesh resolution should be fine enough to fully resolve the turbulence (to the Kolmogorov scale), the interfaces (the surfaces of the smallest droplets) and the interaction between the two. Nevertheless,

the minimum cell sizes used in most of these simulations were several microns and thus will not be sufficient to capture the sub-micron droplets that are known to exist from experiments. The general consensus has been that while the small-scale physics are under-resolved, the large-scale flow remains correct. Since small sub-micron droplets and filaments contain little mass, leaving them under-resolved should have only minor impact on the overall results. Therefore, these "DNS" simulations should be viewed as high-resolution *detailed numerical simulation* without explicit physical models. There are also studies in the literature which employed the sub-grid scale (SGS) model established in single-phase turbulent flows and used interfacial-capturing methods to resolve the interfaces (Lakehal *et al.*, 2012; Agbaglah *et al.*, 2017). However, the single-phase SGS models do not account for two important physical processes in atomization: the unresolved morphology or topology changes of the interfaces, and the interaction between turbulence and interfaces. Therefore, the capability of this type of LES approach to capture the unresolved two-phase turbulence remains to be examined (Aniszewski, 2016). So far, the best way to examine whether a high-fidelity simulation (HFS), either DNS or LES, truly captures the "high-fidelity" details is through a grid refinement study, namely examining if the simulation results yield converged or converging results toward high-fidelity experimental data or analytical solutions. For example, the recent DNS study by Ling *et al.* (Ling *et al.*, 2017, 2019) has varied the mesh for four different levels (from 8 million to 4 billion cells) to identify the resolution required to capture converged high-order turbulence statistics (such as turbulent kinetic energy dissipation) in airblast atomization.

Due to the extreme cost of HFS of atomization, a low-fidelity simulation (LFS) approach is often adopted in macro-scale simulations of practical gasoline fuel injection applications (Dukowicz, 1980; Hoyas *et al.*, 2013; Aguerre and Nigro, 2019; Paredi, Lucchini, D'Errico, Onorati, Pickett, and Lacey, Paredi *et al.*). Since the mesh resolution is not enough to resolve the physical process in atomization, including the primary breakup of the liquid jet, micro-scale flows around droplets, secondary

breakup, droplet collision and coalescence, and small turbulent eddies, different physical models are then required to represent these unresolved physics. The primary breakup is often modeled in the Lagrangian framework, in which the liquid fuels are injected into the domain as discrete parcels/blobs (one parcel represents multiple physical droplets), instead of a continuous bulk liquid jet (Dukowicz, 1980). The droplet formation from the primary breakup is considered to be driven by the shear instability, see for example the Kelvin-Helmholtz (KH) instability model, while the droplet secondary breakup is considered to be dictated by the Rayleigh-Taylor accelerative instability. The hybrid KH-RT model for droplet breakup has been widely used in fuel injection simulations, yielding reasonable agreement with experiments (Beale and Reitz, 1999; Duret *et al.*, 2013). Primary breakup models have also been proposed based on the Eulerian framework, such as the Eulerian/Lagrangian Spray Atomization (ELSA) model (Vallet and Borghi, 1999; Duret *et al.*, 2013). Instead of tracing individual parcels, the ELSA model solves an additional transport equation for the surface density. Furthermore, the unresolved turbulent fluctuations and their effects on the mean flow and droplet breakup also need to be considered. Therefore, the primary breakup models (no matter in Lagrangian or Eulerian frameworks) are usually used together with RANS turbulence models (Sparacino *et al.*, 2019; Duret *et al.*, 2013). Since the flow around each individual droplet is not resolved, the drag force and heat transfer models are required to account for the unresolved interaction between the droplets and surrounding gas (Maxey and Riley, 1983; Michaelides and Feng, 1994; Ling *et al.*, 2016), so that the motion and temperature evolution of the droplets can be captured.

The extreme computational costs still prohibit a DNS for the whole fuel injection process in GDI engines, even with the computer power today. Nevertheless, DNS is still very important to atomization research since they can resolve the interfacial multiphase flows much more accurately and can provide high-level details that are hard to obtain in experiments or LFS. More important, the physical insights and

high-fidelity simulation data obtained in DNS can be used to improve the sub-scale models in LFS through physics-based or data-based approaches. The research direction on improving atomization models through DNS results has received increasing attention and good progress has been made in the past decade (Lebas *et al.*, 2009; Duret *et al.*, 2013).

In the previous studies of DNS of atomization, the inlet conditions for the liquid jet are usually significantly simplified, compared to the liquid fuel jets in GDI engines. For example, the injection velocities used in DNS are usually lower than practical engine conditions and the effect of internal flow on the primary breakup is ignored (Lebas *et al.*, 2009; Desjardins and Pitsch, 2010; Shinjo and Umemura, 2010). Therefore, even though such a simulation can accurately capture the physics of the primary breakup, the process resolved does not faithfully represent the fuel atomization process occurring in GDI engines. The goal of the present study is to accurately model and simulate the primary breakup of a gasoline jet with operating conditions and injector geometry which better represent realistic engine conditions. The Engine Combustion Network (ECN) "Spray G" benchmark case is thus employed. In particular, we will focus on modeling and simulating the experiment by Duke *et al.* (Duke *et al.*, 2017).

The ECN spray G injector geometry is configured based on modern gasoline injection systems and the specified operating conditions correspond to non-reacting early phase of spray-guided gasoline injection. The same injector and operating conditions have been used by different experimental groups with different diagnostic techniques (Duke *et al.*, 2017; Payri *et al.*, 2017; Piazzullo *et al.*, 2018; Sphicas *et al.*, 2018). The experimental database can be then used to validate the numerical model and simulations. Low-fidelity simulations using Lagrangian (Sphicas *et al.*, 2017; Aguerre and Nigro, 2019; Di-Ilio *et al.*, 2019; Paredi, Lucchini, D'Errico, Onorati, Pickett, and Lacey, Paredi *et al.*) and Eulerian (Navarro-Martinez *et al.*, 2020) approaches have been performed to test the breakup models (Aguerre and Nigro, 2019;

Di-Ilio *et al.*, 2019; Navarro-Martinez *et al.*, 2020) and to investigate the inter-plume aerodynamics (Sphicas *et al.*, 2017). Recently, attempts have been made to perform LES of primary breakup including the whole injector geometry (Befrui *et al.*, 2016; Yue *et al.*, 2020). Yet due to the high Reynolds and Weber numbers involved, whether the mesh resolutions in these simulations were sufficient to faithfully resolve both the internal flow and the external turbulent sprays remains to be examined.

In the present study, in order to focus the computational resources on resolving the primary breakup process, the injector geometry will be simplified. Nevertheless, the boundary conditions at the inlet are carefully specified and calibrated based on the X-ray experimental data (Duke *et al.*, 2017) to capture the dominant effect of the internal flow on the liquid jet breakup. To allow for a direct comparison between the numerical and experimental results, a low-volatility gasoline surrogate is used in the simulation, following the experiment. As a result, evaporation is ignored in the present study. For DNS of primary breakup, it is crucial to resolving the sharp interfaces separating the gas and liquid phases. A geometric volume-of-fluid (VOF) method that conserves both mass and momentum is thus used in the present simulation. The VOF method has been implemented in the open-source multiphase flow solver, *Basilisk*. The details of the numerical methods and the simulation setup will be explained in section 3.2. The results will be presented and discussed in section 3.3 and we will summarize the key findings in section 3.4.

## *3.2 Modeling and Simulation Approaches*

### *3.2.1 Governing Equations*

The one-fluid approach is employed to resolve the gas-liquid two-phase flow, where the phases corresponding to the liquid and the gas are treated as one fluid with material properties that change abruptly across the interface. Both the gas and liquid flows are considered as incompressible, so the Navier-Stokes equations with

surface tension can be written as

$$\rho\left(\frac{\partial u_j}{\partial t}+u_i\frac{\partial u_j}{\partial x_i}\right)=-\frac{\partial p}{\partial x_j}+\frac{\partial(2\mu D_{ij})}{\partial x_i}+\sigma\kappa\delta_s n_j\,, \tag{3.1}$$

$$\frac{\partial u_i}{\partial x_i}=0\,, \tag{3.2}$$

where $\rho$, $\mu$, $u$, and $p$ represent density, viscosity, velocity and pressure, respectively, and the subscripts $i,j=1,2,3$ represent the Cartesian indices. The deformation tensor is denoted by $D_{ij}=(\partial_i u_j+\partial_j u_i)/2$. The third term on the right hand side of Eq. (3.1) is a singular term, with a Dirac distribution function $\delta_s$ localized on the interface, and it represents the surface tension. The surface tension coefficient is $\sigma$, and $\kappa$ and $n_i$ are the local curvature and unit normal vector of the interface. The surface tension coefficient $\sigma$ is taken as constant in the present study.

The two different phases are distinguished by a characteristic function $c$, and the temporal evolution of which satisfies the advection equation

$$\frac{\partial c}{\partial t}+u_i\frac{\partial c}{\partial x_i}=0\,, \tag{3.3}$$

the conservative form of which can be expressed as

$$\frac{\partial c}{\partial t}+\frac{\partial(cu_i)}{\partial x_i}=c\frac{\partial u_i}{\partial x_i}\,, \tag{3.4}$$

For incompressible flow, the term on the right hand side is identical to zero.

### *3.2.2 Numerical Methods*

The momentum-conserving volume-of-fluid (MCVOF) method of Fuster and Popinet (Fuster *et al.*, 2018) is employed to resolve the interfacial two-phase flows. In the original paper, the method was introduced in the context of compressible flows. Here we summarize only the important steps that are related to incompressible flows.

3.2.2.1 *Volume-of-fluid method.* In VOF method, the advection equation for $c$, Eq. (3.4), is solved in its integral form

$$\Delta\Omega\frac{\partial f}{\partial t}+\oint_{\partial\Omega}cu_i n_i\mathrm{d}s=\int_\Omega c\frac{\partial u_i}{\partial x_i}\mathrm{d}V\,, \tag{3.5}$$

where $\Delta\Omega$ is the cell volume, and $\partial\Omega$ represents the surface of the cell. The mean value of $c$ in the cell is denoted by $f$,

$$f = \frac{1}{\Delta\Omega}\int_{\Omega} c dV\,, \tag{3.6}$$

which represents the volume fraction of liquid in the cell. The fluid density and viscosity can then be evaluated as

$$\rho = f\rho_l + (1-f)\rho_g\,, \tag{3.7}$$

$$\mu = f\mu_l + (1-f)\mu_g\,. \tag{3.8}$$

where the subscripts $g$ and $l$ represent the gas and the liquid phases, respectively.

The discrete form of Eq. (3.5) on a Cartesian cell can be expressed as

$$\Delta\Omega\frac{f^{n+1}-f^n}{\Delta t} + \Delta_i F_{f,i} = c_c\frac{\partial u_i}{\partial x_i}\Delta\Omega\,. \tag{3.9}$$

The net flux for all three directions is $\Delta_i F_{f,i} = \Delta_1 F_{f,1} + \Delta_2 F_{f,2} + \Delta_3 F_{f,3}$, based on a direction-split advection approach. It has been shown by Weymouth and Yue (Weymouth and Yue, 2010) that the term on the right hand side of Eq. (3.9) is important to guarantee exact mass conservation. Furthermore, $c_c$ is the value of $c$ at the cell center, which can be easily evaluated as $c_c = 1$ if $f > 0.5$ and $c_c = 0$ if $f \leq 0.5$. The value of $c_c$ must be kept as a constant for all sweep directions. The volume-fraction flux $F_{f,i}$ in the direction $i$ is calculated as

$$F_{f,i} = f_a u_{f,i} S\,, \tag{3.10}$$

where $u_{f,i}$ is the $i$-component of velocity at the cell surface where the flux is evaluated, and $S$ is the surface area. The fraction of reference fluid that is advected across the cell surface over $\Delta t$ is $f_a$, which is calculated based on the reconstruction of the interface. Here the piecewise linear interface construction (PLIC) approach is applied (Scardovelli and Zaleski, 1999). The interface normal is computed by the Mixed-Youngs-Centered (MYC) method (Aulisa *et al.*, 2007) and the location of the interface in the cell is calculated based on the method of Scardovelli and Zaleski (Scardovelli and Zaleski, 2000).

3.2.2.2 *Momentum advection.* It has been shown in previous studies that it is important to conserve momentum in the momentum advection near the interface, which is in particular true for cases with a large difference between the densities of the two phases (Vaudor *et al.*, 2017; Fuster and Popinet, 2019). The fundamental requirement is to advect the momentum in Eq. (3.1) in a manner consistent with the advection of the volume fraction in Eq. (3.4).

The momentum equation can be rewritten in its conservative form

$$\frac{\partial \rho u_j}{\partial t} + \frac{\partial (\rho u_i u_j)}{\partial x_i} = -\frac{\partial p}{\partial x_j} + \frac{\partial (2\mu D_{ij})}{\partial x_i} + \sigma \kappa \delta_s n_j \,. \tag{3.11}$$

The discretization of Eq. (3.11) is based on the finite-volume approach and the update of velocity from $u_j^n$ to $u_j^{n+1}$ is done in the following steps (Fuster *et al.*, 2018)

$$\frac{\left(\rho_l f u_j\right)^* - \left(\rho_l f u_j\right)^n}{\Delta t} = -\Delta_i F_{ml,ij} \,, \tag{3.12}$$

$$\frac{\left(\rho_g (1-f) u_j\right)^* - \left(\rho_g (1-f) u_j\right)^n}{\Delta t} = -\Delta_i F_{mg,ij} \,, \tag{3.13}$$

$$u_j^* = \frac{\left(\rho_l f u_j\right)^* + \left(\rho_g (1-f) u_j\right)^*}{\rho_l f^{n+1} + \rho_g (1 - f^{n+1})} \tag{3.14}$$

$$\frac{u_j^{**} - u_j^*}{\Delta t} = \frac{1}{\rho} \frac{\partial (2\mu D_{ij})}{\partial x_i} \,, \tag{3.15}$$

$$\frac{u_j^{***} - u_j^{**}}{\Delta t} = \frac{1}{\rho} \sigma \kappa \frac{\partial f}{\partial x_j} \,, \tag{3.16}$$

$$\frac{u_j^{n+1} - u_j^{***}}{\Delta t} = -\frac{1}{\rho} \frac{\partial p}{\partial x_j} \,, \tag{3.17}$$

where Eqs. (3.12)–(3.14) are for the advection term, and Eqs. (3.15)–(3.17) are for the three forcing terms on the right hand side of Eq. (3.11) (viscous stress, surface tension, and pressure). The viscous term is discretized by the Crank-Nicholson method. The surface tension term is discretized using a balanced-force approach (Francois *et al.*, 2006) and the height-function method is utilized to calculate the local interface curvature (Popinet, 2009). The projection method is used to incorporate the incompressibility condition. The pressure Poisson equation is solved and the pressure obtained is then used in Eq. (3.17) to correct the velocity. The numerical methods to compute these three terms (Eqs. (3.15)–(3.17)) have been discussed in detail in (Popinet, 2009) and thus are not repeated here.

In Eqs. (3.12) and (3.13), $F_{ml,ij}$ and $F_{mg,ij}$ are the fluxes of the liquid and gas $j$-momentum on cell surfaces normal to the $i$ direction, which is the momentum analogue of $F_{f,i}$ in Eq. (3.9). To achieve the important feature of momentum conservation, $F_{ml,ij}$ and $F_{mg,ij}$ are calculated to be consistent with the volume-fraction flux $F_{f,i}$:

$$F_{ml,ij} = (\rho_l u_j)_a f_a u_{f,i} S \,, \tag{3.18}$$

$$F_{mg,ij} = (\rho_g u_j)_a (1 - f_a) u_{f,i} S \,. \tag{3.19}$$

where $(\rho_l u_j)_a$ and $(\rho_g u_j)_a$ denote the liquid and gas momentum per unit volume to be advected. Following the method of (López-Herrera *et al.*, 2015), $(\rho_l u_j)_a$ and $(\rho_g u_j)_a$ are advected as tracers associated with the volume fraction of the corresponding phase non-diffusively. The Bell-Collela-Glaz (BCG) second-order upwind scheme (Bell *et al.*, 1989) is used for the reconstruction of $(\rho_l u_j)$ and $(\rho_g u_j)$ in the cell, and the generalized minmod slope limiter is employed to compute the gradient.

In order to highlight the advantage of the MCVOF method, we have also solved the advection term in the momentum equation using the standard BCG advection scheme (Bell *et al.*, 1989) as in former studies (Popinet, 2009). The results obtained by the two different methods will be compared and discussed in sections 3.2.2.4 and 3.3.3.

3.2.2.3 *Numerical solver.* The above numerical methods have been implemented in the open-source adaptive multiphase solver, *Basilisk* (Popinet, Popinet). In particular, the VOF associated tracer advection method of López-Herrera *et al.* (López-Herrera *et al.*, 2015) was implemented in the header file "vof.h", which is used for momentum advection in "conserving.h" (Popinet, Popinet). In *Basilisk*, a finite volume approach based on a projection method is used. The mass and momentum control volumes are collocated in the spatial discretization, which makes it easier to calculate the momentum flux consistently with the volume-fraction flux. A staggered-in-time discretization of the volume-fraction/density and pressure leads to a formally second-order accurate time discretization. An octree spatial discretization is used in

3D simulations, which gives a very important flexibility allowing dynamic grid refinement into user-defined regions. The adaptation criterion is based on the wavelet estimate of the discretization error (van Hooft *et al.*, 2018). The parallelization of the solver is done through a tree decomposition approach to guarantee a high parallel performance even if a large number of refinement levels are used.

3.2.2.4 *Validation test: 2D rising bubble.* The 2D rising-bubble benchmark problem proposed by Hysing *et al.* (Hysing *et al.*, 2009) is employed to validate the MCVOF method described in section 3.2.2 and to examine the distinction between the MCVOF method and the conventional BCG methods. This benchmark case has been tested by different two-phase flow solvers using different numerical methods. The converged numerical results obtained by the MooNMD code (John and Matthies, 2004; Ganesan *et al.*, 2007), which uses an arbitrary Lagrangian–Eulerian approach, can be used as a reference for numerical method validation. The densities and viscosities for the liquid and gas phases are given as $\rho_l = 1000, \mu_l = 10, \rho_g = 1, and \mu_g = 0.1$. The surface tension is $\sigma = 1.96$, and the gravity is $g = 0.98$. All parameters here are dimensionless. The 2D computational domain and the bubble surfaces at different times are shown in Fig. 3.1(a). The bottom of the domain is a symmetric boundary. The bubble is initially a circle of diameter $d = 0.25$ and stationary. The bubble rises and deforms due to buoyancy effect. In this test, we have only considered the time up to 2, since capturing the skirt of the bubble formed at later time will require a much higher mesh resolution. The temporal evolution of the bubble centroid obtained by the BCG and MCVOF methods are shown in Figs. 3.1(b)-(d). It is observed that the results for both of the methods agree well with the reference data in general. Close-ups at the local maximum and minimum of the centroid velocity are shown in Figs. 3.1(c) and (d), which clearly show that the MCVOF method is more accurate and the results converge to the reference data faster when the mesh is refined. It is worth noting that for the coarse mesh ($d/\Delta_{\min} = 64$) the MCVOF method does a much better job, compared to the BCG method. This feature is particularly important

to atomization simulations, since the mesh resolution is sometimes relatively low in resolving the small-scale interfacial flow features.

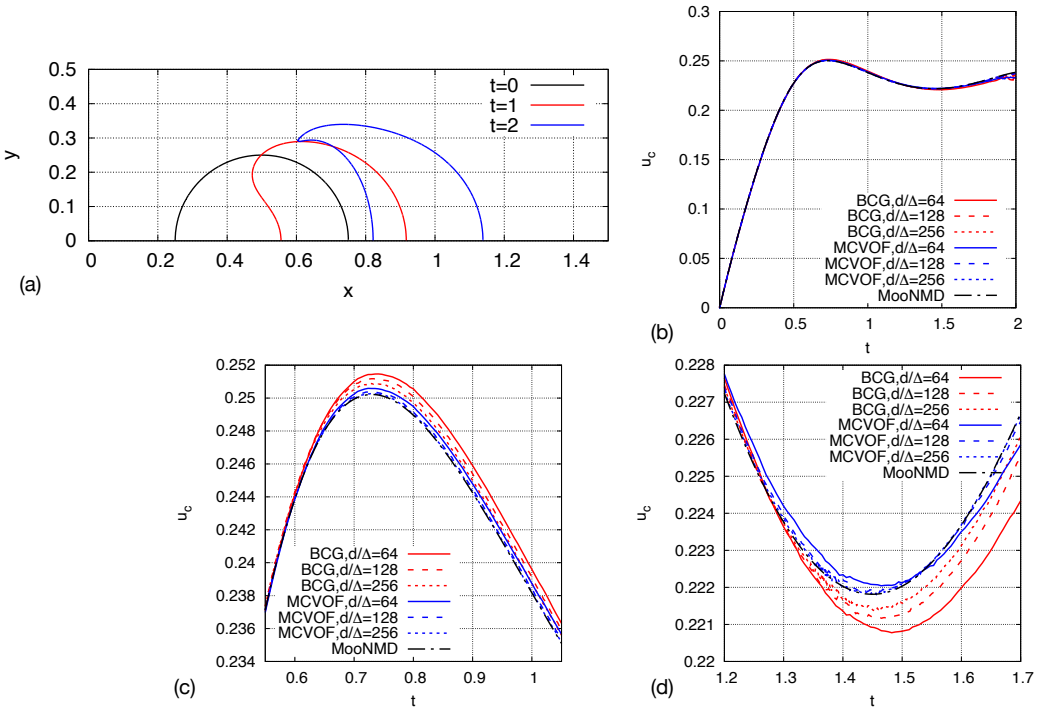


Figure 3.1. Results for the 2D test problem of a rising bubble. (a) Computation domain and bubble surfaces; (b) temporal evolution of bubble centroid velocity; (c) and (d) closeups near the local maximum and minimum of the bubble velocity.

### *3.2.3 Modeling and Simulation Setup*

3.2.3.1 *A simplified model for the spray G injector.* The computational domain is shown in Fig. 3.2(a). Simplifications on the injector geometry have been made to focus the computational resources on capturing the interfacial dynamics and primary breakup of the liquid jet.

First of all, only one of the eight jets generated by the ECN Spray G injector is considered. The original injector has eight holes which are uniformly distributed azimuthally (Duke *et al.*, 2017). The jets are spatially separated (Sphicas *et al.*, 2018), therefore, ignoring inter-jet interaction will not influence the primary breakup in the near field (Befrui *et al.*, 2016; Yue *et al.*, 2020).

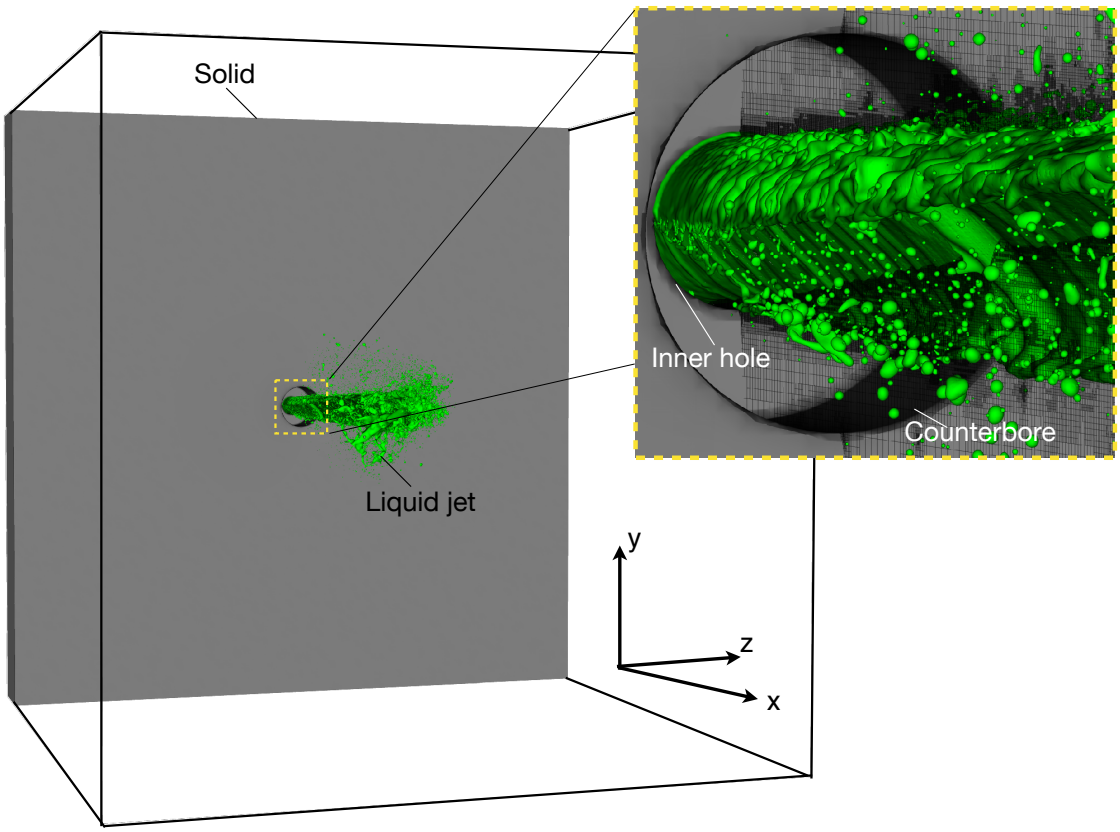


Figure 3.2. Computational domain and the mesh used to simulate the primary breakup of the liquid jet with a nonzero injection angle.

Furthermore, the injector in the numerical model includes only the inner-hole and counterbore, with the portions upstream, such as the needle, ignored, see Fig. 3.4(a). As a result, the internal liquid flow over the needle into the inner-hole will not be simulated. Special boundary conditions, as will be discussed below, will be applied to model the dominant effect of the internal flow on the primary breakup.

At last, the rate of injection is taken to be a constant. The inlet flow rate in the original Spray G operation varies in time due to the lifting and closing motion of the needle. Here, we only consider the injection rate corresponding to the quasi-steady phase when the needle is completely open. It has been shown in previous experiments that the transition phase is short and its impact on the jet dynamics, such as the penetration length, is generally small (Duke *et al.*, 2017).

The grey color in Fig. 3.2(a) indicates the embedded solid in the domain, representing the injector geometry. The embedded solid is specified through the solid volume fraction in a cell, $f_s$. Therefore, $f_s = 1$ for cells fully occupied by solid, $f_s = 0$ for cells with only gas or liquid, and $f_s$ is fractional for cells containing solid boundaries. Since the embedded solid here, namely the injector nozzle, is stationary, the velocity in the cells with $f_s \neq 0$ are masked as $\boldsymbol{u} = (1 - f_s)\boldsymbol{u}$ to achieve the no-slip boundary condition at the solid boundaries. To reduce the numerical error induced by the embedded solid, cells containing solid boundaries are always refined to the maximum refinement level. A 2D test of the liquid jet entering the domain through a solid nozzle was performed and the results are shown in Fig. 3.3. As can be seen, the boundary layer near the solid boundary and the gas-liquid interface are well resolved.

3.2.3.2 *Boundary conditions.* Previous numerical studies on the full Spray G injector showed that when the liquid flows over the needle and enters the inner-hole, the liquid velocity at the inlet of the inner-hole is not aligned with the inner-hole axis (Befrui *et al.*, 2016). The angle between the inlet velocity and the inner-hole axis is referred to as the "injection angle", denoted by $\alpha$. This nonzero injection angle will introduce an interaction between the injected liquid with the inner-hole wall and will

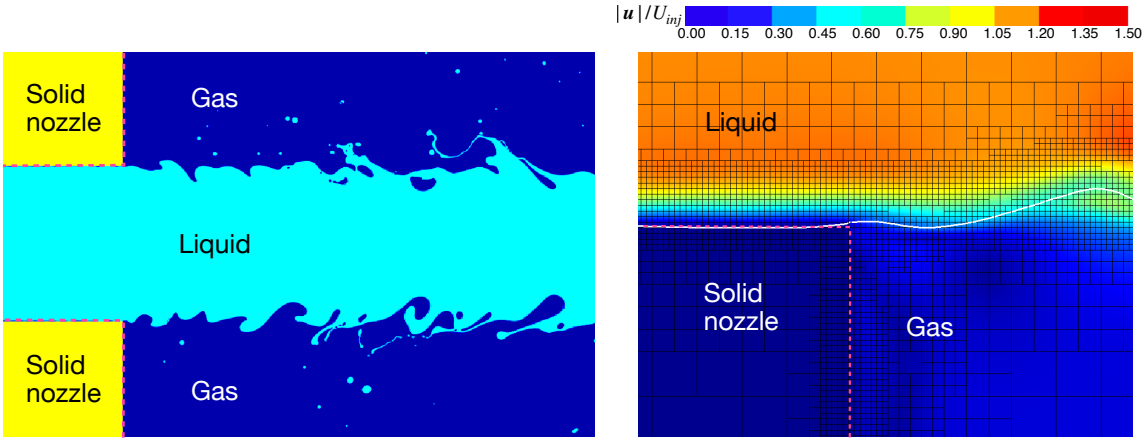


(a) Solid nozzle and liquid jet (b) Velocity magnitude near the exit

Figure 3.3. (a) The liquid jet at the inner-hole exit and (b) closeup of the velocity field at the nozzle exit. The purple dashed lines indicate the solid boundaries.

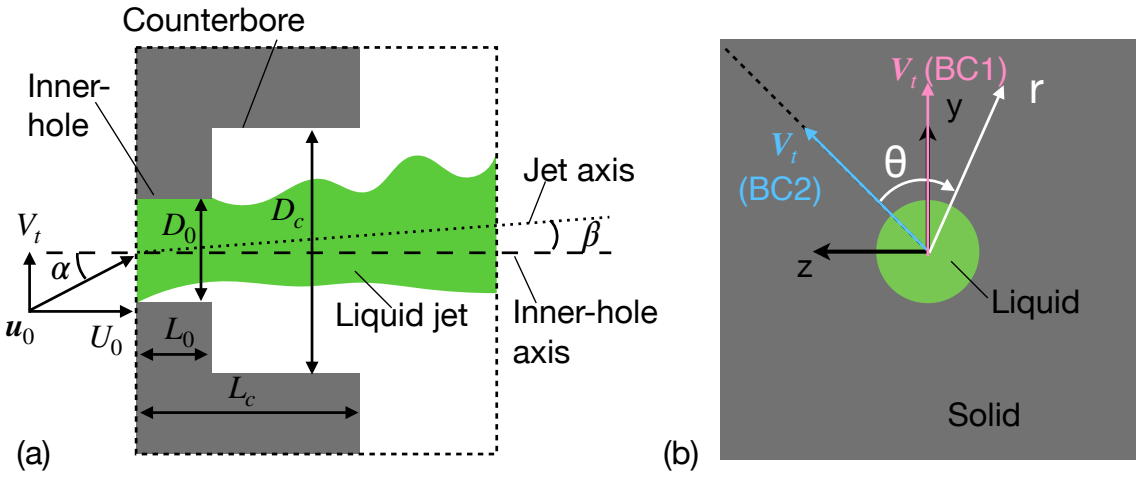


Figure 3.4. Schematics for the inlet boundary conditions on the (a) symmetric plane along the tangential inlet velocity $\boldsymbol{V}_t$ and (b) the $y$-$z$ plane at the inlet. Two different ways to specify the tangential inlet velocity are indicated as BC1 and BC2 in (b).

Table 3.1. Dimensions of the inner-hole and counterbore and injection velocity components used in the present simulation. The parameters are chosen to be consistent with the experiment (Duke *et al.*, 2017).

| $D_0$ ($\mu$m) | $D_c$ ($\mu$m) | $L_0$ ($\mu$m) | $L_c$ ($\mu$m) | $U_0$ (m/s) | $V_t$ (m/s) |
|---|---|---|---|---|---|
| 173 | 388 | 152 | 395 | 89 | $0, 17.8, 35.6$ |

influence the macro-scale and micro-scale features of the primary breakup, see the closeup of the jet near the exit of the injector in Fig. 3.2. In the present study, $\alpha$ is specified through the Dirichlet velocity boundary condition at the inlet, which is schematically shown in Fig. 3.4.

The spatial dimensions of the injector geometry are chosen to be the same as the experiment (Duke *et al.*, 2017) and are listed in Table 3.2. The normal component of the inlet velocity (along the $x$ axis), $U_0$, is determined by the mass flow rate for the quasi-steady phase of injection (Duke *et al.*, 2017). The two tangential components of the inlet velocity, along the $y$ and $z$ axes, are represented by $V_0$ and $W_0$, respectively. The magnitude of the total tangential inlet velocity $V_t = |\boldsymbol{V}_t| = \sqrt{V_0^2 + W_0^2}$ varies with the injection angle $\alpha$, or the tangent of $\alpha$, $\eta = \tan(\alpha) = V_t/U_0$. We have tested two different ways to specify the tangential inlet velocity $\boldsymbol{V}_t$: 1) $V_0 = V_t$ and $W_0 = 0$ and 2) $V_0 = V_t/\sqrt{2}$ and $W_0 = V_t/\sqrt{2}$. These two boundary conditions are denoted as BC1 and BC2 in Fig. 3.4(b), respectively. For the BC1, $\boldsymbol{V}_t$ is aligned with the y axis and it will be shown later that this exact alignment between $\boldsymbol{V}_t$ and the Cartesian mesh will introduce a numerical artifact on the jet surfaces. Rotating $\boldsymbol{V}_t$ for 45 degrees as in the BC2 significantly reduces this numerical artifact.

For the convenience of discussion of the simulation results, a cylindrical coordinate, $(r, \theta, x)$, is introduced, see Fig. 3.4(b). The azimuthal angle, $\theta$, is defined with respect to $\boldsymbol{V}_t$ according to the BC2.

In the present setup, no disturbance is added in the inlet velocity, yet the numerical error induced by the embedded solid plays the role of inlet flow fluctuations. The turbulent velocity fluctuations at the jet inlet can have an impact in the interfacial

instability development and the resulting spray characteristics (Ménard *et al.*, 2007; Jiang and Ling, 2019). A systematic investigation of the effect of the inlet disturbance is of interest but out of the scope of the present study.

The pressure-outlet boundary condition is invoked at the right surface of the domain. All lateral boundaries of the domain are taken to be slip walls. Thanks to the adaptive mesh, a large simulation domain is used. The length of the cubic domain edge is $H = 32D_0$, where $D_0$ is the diameter of the inner-hole, see Fig. 3.4(a). The effects of the lateral boundaries on the jet are negligible.

3.2.3.3 *Mesh resolution.* The octree mesh is used to discretize the domain. The local cell size is adapted based on the estimated discretization errors of the volume fraction $f$ and the three components of velocity $u_i$. The assessment of discretization error for each scalar is achieved through a wavelet transform (van Hooft *et al.*, 2018). If the estimated error is larger than the specified threshold, the mesh will be locally refined, or vice versa. For the present simulation, the normalized error thresholds for the volume fraction and all three velocity components are all set as 0.01. For the present problem, the mesh is generally refined to the maximum level near the jet surfaces. The error threshold for velocity is used to identify the region away from the jet, where the mesh can be coarsened. As shown in Figs. 3.2 and 3.3, the threshold values used here are sufficient to refine the mesh to resolve the interfaces and the shear layers near the interfaces.

The minimum cell size in the octree mesh is controlled by the maximum refinement level, $L$, *i.e.*, $\Delta_{\min} = H/2^L$. Two different meshes have been used, $L = 11$ ($\Delta_{\min} = 2.70$ $\mu$m) and $L = 12$ ($\Delta_{\min} = 1.35$ $\mu$m), and the corresponding meshes are denoted as L11 and L12, respectively. A representative snapshot of the L12 mesh is shown in Fig. 3.2. It can be seen that a high mesh resolution is used to resolve the jet surfaces and the flow nearby, while the mesh away from the jet is coarsened to reduce the computational cost. The total number of cells increases in time as more and more liquid enters into the domain. The mesh shown in Fig. 3.2 consists of about

Table 3.2. Fluid properties used in the simulation. The parameters are chosen to be consistent with the experiment by Duke *et al.*(Duke *et al.*, 2017).

| $\rho_l$ (kg/m$^3$) | $\rho_g$ (kg/m$^3$) | $\mu_l$ (Pa s) | $\mu_g$ (Pa s) | $\sigma$ (N/m) |
|---|---|---|---|---|
| 838 | 3.6 | $9.64 \times 10^{-4}$ | $1.77 \times 10^{-5}$ | 0.0278 |

Table 3.3. Key dimensionless parameters.

| $Re_g$ $D_0U_0/\nu_g$ | $Re_l$ $D_0U_0/\nu_l$ | $We_l$ $\rho_l D_0 U_0^2/\sigma$ | $\xi$ $\rho_l/\rho_g$ | $\eta$ $V_0/U_0$ |
|---|---|---|---|---|
| 3130 | 13400 | 41300 | 233 | 0, 0.2, 0.4 |

160 million cells. The maximum number of cells in the L12 mesh simulation goes up to 210 million, compared to $(2^{12})^3 \approx 69$ billion cells for the equivalent uniform Cartesian mesh. The simulations for the L11 mesh were performed on the Baylor cluster *Kodiak* using 144 cores (Intel E5-2695 V4). The simulation for the L12 mesh was run on the machine *Stampede2* at the Texas Advanced Computing Center with 1440 cores (Intel Xeon Platinum 8160) for about 4 days.

### *3.2.4 Fluid Properties and Key Parameters*

The fluid properties and the injection conditions are chosen to be similar to the experiment by Duke *et al.* (Duke *et al.*, 2017). The X-ray diagnostics facilities at Argonne National Laboratory were used in the experiment and were restricted to non-evaporative conditions. Therefore, the liquid and gas were replaced by a low-volatility gasoline surrogate (Viscor 16br, Rock Valley Oil & Chemical Company) and nitrogen, respectively. The chamber pressure was decreased so that the gas-to-liquid density ratio remains the same as the standard Spray G conditions.

If the gas density $\rho_g$, the inner-hole diameter $D_0$, and the normal inlet velocity $U_0$ are chosen to be the reference scales, the key dimensionless parameters can be defined and the values are given in Table 3.3. The Reynolds and Weber numbers of the liquid jet are defined as $\mathrm{Re}_l = \rho_l(D_0)U_0/\mu_l$ and $\mathrm{We}_l = \rho_l(D_0)U_0^2/\sigma$. For the large values of $\mathrm{Re}_l$ and $\mathrm{We}_l$ here, the viscous and surface tension forces are insufficient to hold the injected liquid as a bulk, and the liquid jet will break. The Reynolds

Table 3.4. Test cases for different mesh resolutions, boundary conditions, and momentum-advection methods, considered in the present study.

| Test | Maximum level | Boundary Conditions | Momentum advection method |
|---|---|---|---|
| 1 | 11 | BC1 | MCVOF |
| 2 | 11 | BC2 | BCG |
| 3 | 11 | BC2 | MCVOF |
| 4 | 12 | BC2 | MCVOF |

number based on gas properties, $\mathrm{Re}_g = \rho_g D_0 U_0/\mu_g$, is defined to characterize the gas flow induced by the liquid jet. When $\mathrm{Re}_g$ is large, the gas flow will turn to turbulent. The liquid-to-gas density ratio is represented by $\xi$ with $\xi = \rho_l/\rho_g$. Finally, the angle between the inlet velocity and the inner-hole axis is characterized by its tangent, $\eta = \tan\alpha$, and different values of $\eta$ are considered.

### *3.2.5 Summary of Simulation Cases*

To investigate the effects of simulation approaches on the results, four different tests have been performed, which are summarized in Table 3.4. Tests 1 to 3 are done on the coarser L11 mesh to examine the effects of inlet boundary condition (BC1 and BC2) and the numerical method for momentum advection (MCVOF and BCG) on the simulation results. Test 4 uses the same numerical method and boundary condition as Test 3, but is performed on the finer L12 mesh, to show the effect of mesh resolution. For Test 3, different $\eta$, varying from 0 to 0.4 are simulated. The simulation results for these tests will be presented and discussed in section 3.3.

## *3.3 Results*

### *3.3.1 General Effect of the Nonzero Injection Angle on the Liquid Jet*

The simulation results for Test 4 and $\eta = 0.2$ are shown in Fig. 3.5 to illustrate the effect of the nonzero injection angle on the liquid jet. In Fig. 3.5, the liquid is injected into the stagnant gas from the left, with a view angle for which $\boldsymbol{V}_t$ points upward. The boundaries of the inner-hole and counterbore on the central plane are indicated by the black dashed lines. The nonzero injection angle induces several new

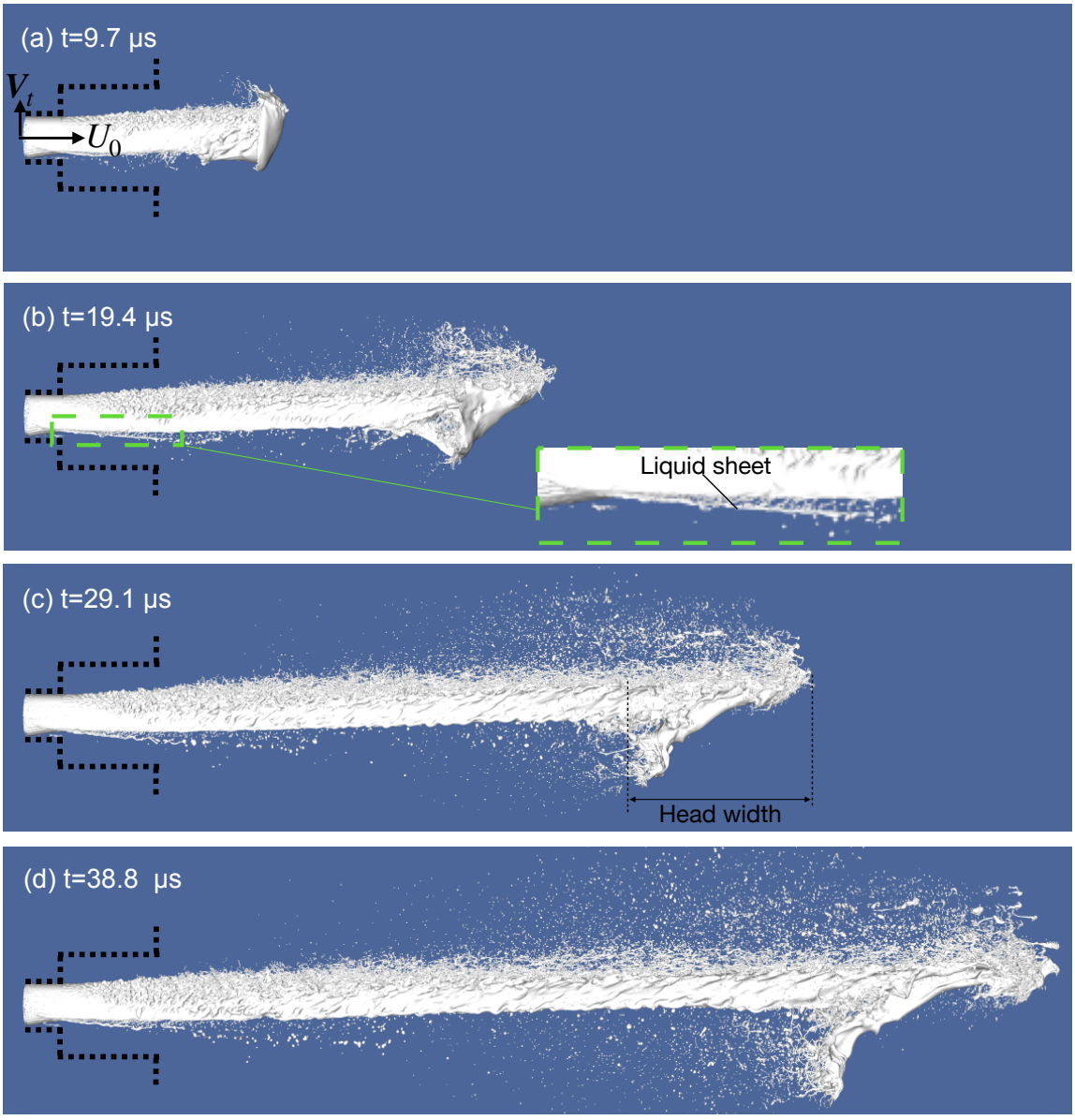


Figure 3.5. Temporal evolution of the liquid jet for $\eta = 0.2$ and Test 4 (L12 mesh). The dashed lines denote the boundaries of the inner-hole and counterbore on the central plane.

features of primary breakup that have not been observed in a round jet with zero injection angle (Lebas *et al.*, 2009; Shinjo and Umemura, 2010).

First of all, the liquid jet is seen to detach from the bottom wall of the inner-hole. The ambient gas is then entrained into the gap between the liquid surface and the inner-hole wall. This phenomenon has also been observed in simulations for the full spray G injector (Befrui *et al.*, 2016).

Secondly, the liquid jet loses its azimuthal symmetry. For the case with zero injection angle, see *e.g.*, (Shinjo and Umemura, 2010), the overall shape of the jet remains symmetric, though small-scale features, like interfacial waves and ligaments, may vary azimuthally. Here, the interfacial instability develops much faster on the top surface of the jet than the lateral and bottom surfaces. Furthermore, the top of the jet head moves faster than the bottom, resulting in a stretching of the jet head in the streamwise direction, see Fig. 3.5(c). The upper part of the jet head also breaks earlier and more violently. The asymmetry breakup dynamics eventually leads to a non-uniform spatial distribution of droplets: significantly more droplets are formed above the jet than below.

At last, it is observed that liquid sheets develop on the two lateral sides of the liquid jet after it leaves the inner-hole, see the closeup in Fig. 3.5(b). This is due to the interaction between the liquid flow and the inner-hole wall and the resulting flow around the inner-hole wall from the top to the bottom (both clockwise from $\theta = 0$ to $\pi$ and also counter-clockwise from $\theta = 0$ to $-\pi$). Capillary breakups occur near the edge of this liquid sheet, forming relatively large droplets below the jet.

### *3.3.2 Effect of the Injection Angle on Jet Penetration and Deflection*

The detachment of the liquid jet within the inner-hole reduces the cross-section area of the liquid jet. Due to mass conservation, the liquid velocity increases, resulting in a faster penetration of the liquid jet. A quantitative evaluation of the effect of $\eta$ on the jet penetration length is shown in Fig. 3.6(a). In order to directly compare the simulation results with the experimental data, the penetration length of the liquid

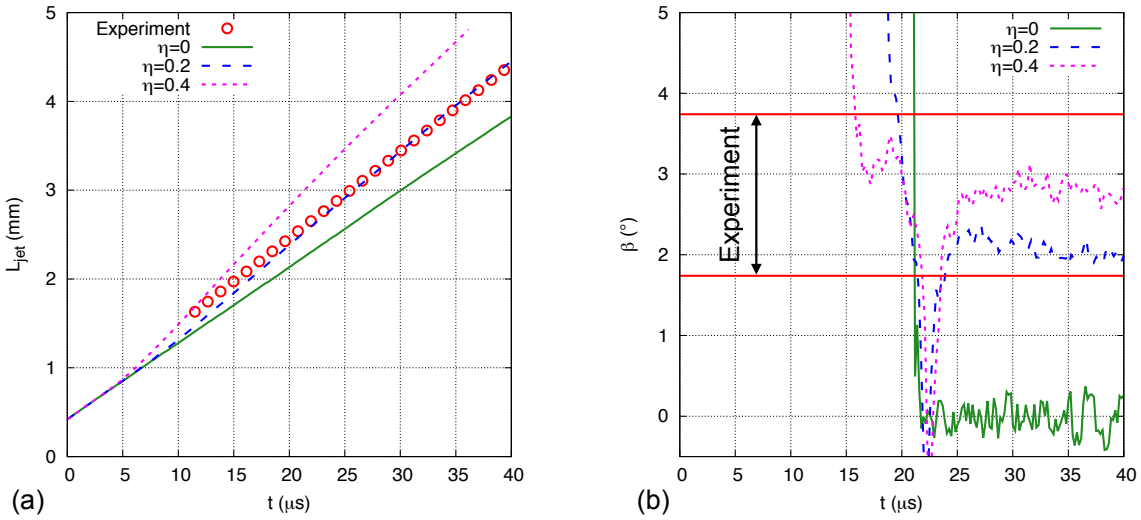


Figure 3.6. Temporal evolutions of (a) the liquid jet penetration and (b) the jet deflection angle for different injection angles, $\eta = \tan(\alpha)$. The simulation results are for Test 3 and the experimental data are from Ref. (Duke *et al.*, 2017).

jet, $L_{jet}$, is defined based on the transverse integrated mass (TIM) (Duke *et al.*, 2017). The TIM is calculated by integrating the liquid density over the $y$-$z$ plane at a given streamwise location and thus is a function of $x$ and $t$:

$$\mathrm{TIM}(x,t) = \iint \rho_l(x,y,z,t)\,\mathrm{d}y\,\mathrm{d}z\,. \tag{3.20}$$

The threshold of TIM for determining the penetration length is taken to be 20% of $\mathrm{TIM}_{\mathrm{inlet}}$, consistent with the experiment. Results for three different injection angles are shown here, $\eta = 0, 0.2$ and 0.4. The slopes of the lines represent the penetration speed. It can be observed that for $\eta = 0$, penetration speed is constant. The penetration speed for $t \lesssim 5$ $\mu$s varies little with $\eta$ due to the confinement effect of the inner-hole wall. Yet soon after the jet head leaves the inner-hole exit, the penetration speed for nonzero $\eta$ transits to a larger value at about $t = 5$ $\mu$s. Since then the penetration speed remains unchanged in the rest of the time range considered ($5 \lesssim t \lesssim 40$ $\mu$s). In the long term, the penetration speed of the jet will decrease in the far field (Duke *et al.*, 2017). Nevertheless, the present simulation focuses on the short-term dynamics of the jet in the near field, the variation of the penetration speed after the early transition is negligibly small. For convenience, hereafter, we simply refer to

the penetration speed as the value after the transition. It can be observed that the penetration speed monotonically increases with $\eta$. The penetration length for $\eta = 0.2$ agrees well with the experimental results.

The nonzero injection angle also induces a deflection of the liquid jet. The deflection angle $\beta$ is defined as the angle between the axes of the liquid jet and the inner-hole, see Fig. 3.4(a). The axis of the liquid jet consists of centroids of the liquid phase on the cross sections normal to the $x$-direction. The deflection angle is then calculated as $\beta = \tan^{-1}(\sqrt{y_m^2 + z_m^2}/x_m)$, where $x_m, y_m$ and $z_m$ are the coordinates of the centroid of liquid phase. We measured $\beta$ at about $x/D_0 = 11$ (x=2 mm), following the experiment (Duke *et al.*, 2017), and the results are shown in Fig. 3.6(b). The deflection angle can only be measured after the jet has reached the measurement location. The fluctuations for $t = 16$ to 24 $\mu$s in the results are due to the passage of the jet head. After the transition, $\beta$ reaches a quasi-steady state with small-amplitude fluctuations due to the interfacial waves on the jet surface. For $\eta = 0$, the mean of $\beta$ is close to zero, namely there is no deflection of the liquid jet. Similar to the penetration speed, the mean of $\beta$ increases monotonically with $\eta$. The experimental result for $\beta$ has a quite large error bar, which is indicated by the two horizontal lines in Fig. 3.6(b). The simulation results for both $\eta = 0.2$ and 0.4 lie in the range of the experimental data (Duke *et al.*, 2017). The deflection angle $\beta$ is generally smaller than the injection angle $\alpha$ due to the constraint of the inner-hole wall.

Since the injection angle $\alpha$ is used here to model the dominant effect of the neglected internal flow on the dynamics of the liquid jet, the value of $\alpha$ is not known a priori. The results presented in Fig. 3.6 serve to identify the value of $\alpha$ that best represents the overall dynamics of the Spray G jet. It is shown that $\eta = 0.2$ ($\alpha = 11.3^\circ$) yields the best agreement with the experimental results for both the jet penetration and deflection. More different values of $\eta$ have been tested to identify the best $\eta$ value, though only three of them are shown here.

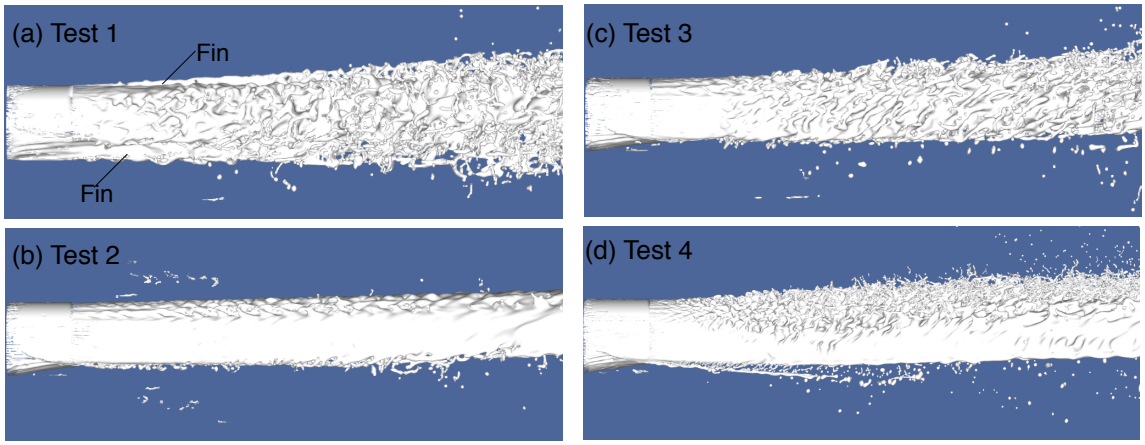


Figure 3.7. The surfaces of the liquid jet at $t = 19.4$ $\mu$s for different test cases (see Table 3.4) for $\eta = 0.2$. (a) Test 1: using the L11 mesh, the boundary condition with the tangential inlet velocity aligned with the $y$-axis (BC1), and the MCVOF method for momentum advection; (b) Test 2: using the L11 mesh, the boundary condition with the tangential inlet velocity rotated 45 °(BC2), and the BCG method for momentum advection; (c) Test 3: using the L11 mesh, the BC2, and the MCVOF method for momentum advection; (d) Test 4: using the L12 mesh, the BC2, and the MCVOF method for momentum advection.

### *3.3.3 Effects of Simulation Approaches on Resolving the Primary Breakup*

To show that the simulation approach taken in the present study, in terms of boundary conditions, numerical methods, and mesh resolution, is able and necessary to resolve the primary breakup of the liquid jet with a nonzero injection angle, four different test cases have been performed for $\eta = 0.2$, see Table 3.4. The results for the four test cases are shown in Figs. 3.7 and 3.8.

Two different boundary conditions (BC1 and BC2) for the tangential inlet velocity, $\boldsymbol{V}_t$, were used in Tests 1 and 3 (see Fig. 3.4 and Table 3.4). Comparing Figs. 3.7(a) and (c), it can be observed that "fins" are formed on the top and bottom of the jet for Test 1, which is obviously a numerical artifact. Since a Cartesian mesh is used to resolve a cylindrical jet, the numerical error adherent to the Cartesian grid (such as that in the curvature and surface tension calculations) will influence the interfacial instability development. For Test 1, the numerical error is amplified due to the alignment of $\boldsymbol{V}_t$ with the mesh. In Test 3, the tangential inlet velocity is rotated for 45 degrees, significant improvement was observed and the numerical "fin" vanishes, see Fig. 3.7(c).

The MCVOF method describe in 3.2.2 has been used for momentum advection in the present simulations. As already shown in section 3.2.2.4, the MCVOF method performs better than the BCG method, in particular when the mesh is relatively coarse. To further evaluate the effect of the momentum-advection method on the primary breakup dynamics, a simulation using purely the BCG method for momentum advection (Test 2) is conducted and the results are compared to those obtained by the MCVOF method (Test 3). The same VOF method has been used to advect the liquid volume fraction for both cases, so the differences in the results are purely induced by the different methods for the momentum advection. It can be clearly seen in Figs. 3.7(b) and (c) that the jet surfaces for Tests 2 and 3 are very different. In Test 3, the interfacial waves, the rims and fingers formed at the edges of liquid lobes are captured; while these important primary breakup features are missed in Test 2. Former studies have shown that, a non-momentum-conserving VOF method could introduce numerical breakups of the interfacial waves, which occur earlier and in smaller spatial scale than the physical reality (Ling *et al.*, 2017). The results for Test 2 shown in Fig. 3.7(b) correspond to the jet surface after those numerical breakups occurred and that is why the surfaces appear to be smoother than Test 3. Comparing the results for Tests 2 and 3 (L11 mesh) with those for Test 4 (L12 mesh), it is obvious that the MCVOF results (Test 3) are closer to the fine mesh results. The differences in the results for the jet surface deformation and breakup, captured by the two different numerical methods, will also impact the resulting droplet statistics.

The results for Tests 3 and 4 show the effect of mesh resolution on the primary breakup features. As shown in Fig. 3.7(d), Test 4 has captured the smaller wavy structures and ligaments that are not resolved in Test 3. As a result, the formation of smaller droplets is better captured and significantly more droplets are observed in Test 4 than in Test 3. The formation and subsequent breakup of the liquid sheets on the lateral sides of the jet near the inner-hole exit are clearly seen in Test 4, but not in Test 3. This indicates that a fine mesh is necessary to resolve the fine details

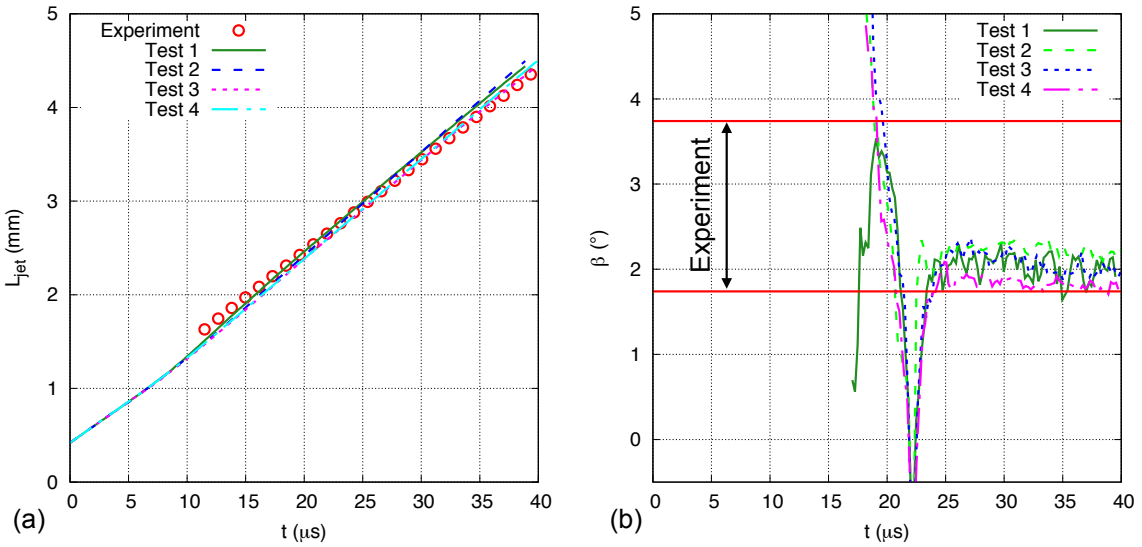


Figure 3.8. Temporal evolutions of (a) the liquid jet penetration and (b) the jet deflection angle for different test cases (see Table 3.4) for $\eta = 0.2$. The experimental data are from Ref. (Duke *et al.*, 2017).

of the primary breakup and to achieve accurate droplet statistics. Based on the difference between the Tests 3 and 4 results, a simulation with an additional level of grid refinement, *i.e.*, L13, may be needed to fully confirm mesh independency of the simulation results. Due to the high computational cost required, such a simulation will be relegated to our future work.

It is worth indicating that, the penetration length and the jet deflection angle for these four tests are actually very similar, see Fig. 3.8. When the mesh is refined from L11 to L12, the jet penetration length and deflection angle vary little, see Fig. 3.8, and both agree well with the experimental results. Similar conclusions can be made for the change of boundary conditions and numerical methods. This observation seems to show that the micro-scale breakup features do not have a strong influence on the macro-scale dynamics of the jet. Nevertheless, a high mesh resolution, proper boundary condition setup, and accurate numerical methods are required to resolve the micro-scale features like interfacial waves and formation of ligaments and droplets.

The results in sections 3.3.2 and 3.3.3 have affirmed that, the numerical model for the injection angle $\eta = 0.2$ and the simulation approaches specified in Test 4 will

capture both the macro-scale and micro-scale primary breakup features of the liquid jet. Therefore, in the rest of the paper, we will focus on the results for $\eta = 0.2$ and Test 4.

### *3.3.4 Interfacial Waves on the Jet Core*

The liquid jet surfaces at $t = 19.4$ $\mu$s near the inner-hole exit are shown in Fig. 3.9 from different view angles. The gas-liquid interfaces are colored with the streamwise velocity. At this time, the portion of the jet shown ($x/D_0 \lesssim 7$) has reached a statistically steady state, namely the average features of the surface morphology and the streamwise velocity do not vary in time.

The color on the jet surface clearly shows that the streamwise velocity is higher at the top of the jet ($\theta = 0$) and decreases clock-wisely from $\theta = 0$ to $\pi$ (also counter-clock-wisely from $\theta = 0$ to $-\pi$ due to symmetry). Since the shear interfacial instability on the jet surface is driven by the velocity difference between the liquid and gas (Squire, 1953; Yih, 1967; Otto *et al.*, 2013), the larger velocity at the top of the jet results in faster growing longitudinal interfacial waves. As the waves are advected downstream and grow in amplitude, the transverse waves arise and develop into lobes or fingers (Marmottant and Villermaux, 2004; Jarrahbashi *et al.*, 2016). Following the longitudinal waves, the transverse waves and lobes/fingers also develop faster at the top of the jet. The lobes/fingers are stretched by the surrounding gas and eventually disintegrate into small ligaments and droplets. After the ligaments and droplets are detached from the jet core, the aerodynamic drag causes them to slow down, as indicated by the blue color of the droplets and ligaments above the jet shown in the closeup of Fig. 3.9(a).

Due to the nonzero injection angle and the interaction between the injected liquid and the inner-hole wall, liquid sheets are formed on the two lateral sides of the jet near the inner-hole exit and extend toward the bottom, see Figs. 3.9(b) and (c). Holes arise in the liquid sheet soon after the liquid exits the inner-hole, which cause the liquid sheet to rapture. The rims at the edges of the sheets are then separated

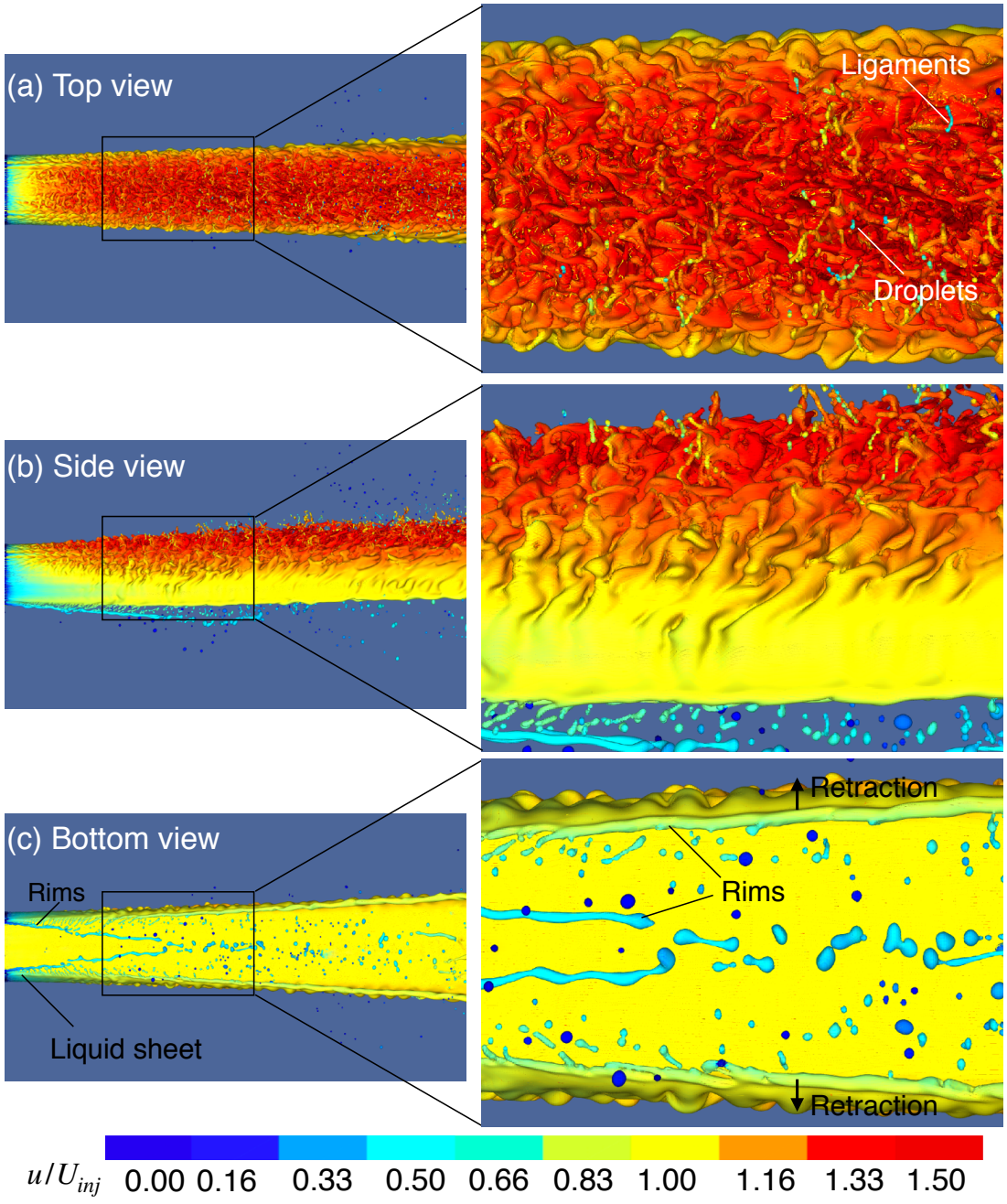


Figure 3.9. Interfacial waves on the jet core surface at $t = 19.4$ $\mu$s. The gas-liquid interfaces are colored by the streamwise velocity $u$.

from the jet core and become long ligaments. The unbroken liquid sheets attached to the jet core retract back toward the jet due to the Taylor-Culick effect. The two rims detached from the jet core, at the center of Fig. 3.9(c), eventually break into droplets. These droplets are significantly larger than those formed from the interfacial waves at the top of the jet, see Fig. 3.9(b).

In order to better show the variation of the longitudinal interfacial waves over the azimuthal angle, the jet surface contours for $\theta$ from 0 to $\pi/2$ are shown in Fig. 3.10. In each figure, the results for two different time instants are presented. Important wave features, such as the wavelength and amplitude, for the two different times are very similar, affirming that the portion of the jet has reached a quasi-steady state. The blue dashed lines indicate the outer boundary of the counterbore. Due to the higher liquid velocity for $\theta = 0$ and $\pi/6$, the wave amplitudes grow much faster than those for $\theta = \pi/3$ and $\pi/2$. The interfacial waves for small $\theta$ start to roll up and break into droplets and ligaments even within the counterbore. In the spatial region shown here, there are no droplets formed for $\theta = \pi/3$ and $\pi/2$. The average wavelength for $\theta = \pi/2$ is about 28 $\mu$m, which is more than 45% larger than the average wavelength for $\theta = 0$. The average wave length for $\theta = 0$ is only calculated for $x \lesssim 0.5$ mm, as it is hard to identify individual waves after the waves roll up and break.

### *3.3.5 Deformation and Breakup of the Jet Head*

Droplets are formed not only near the jet core, but also from the continuous breakup of the jet head. Actually, the number of droplets produced due to the breakup of the jet head is significantly higher than that for the jet core. Here, the term "jet head" includes also the liquid sheets extended from the tip of the liquid jet. The temporal evolution of the jet head is depicted in Fig. 3.11. Similar to Fig. 3.9, the color represents the streamwise velocity on the interface. It can be clearly seen that the velocity at the top of the jet head is higher than that at the bottom. At early time, the shape of the head remains approximately spherical on the front view, see Fig. 3.11(e). Yet as time elapses, the deformation of the jet head becomes strongly

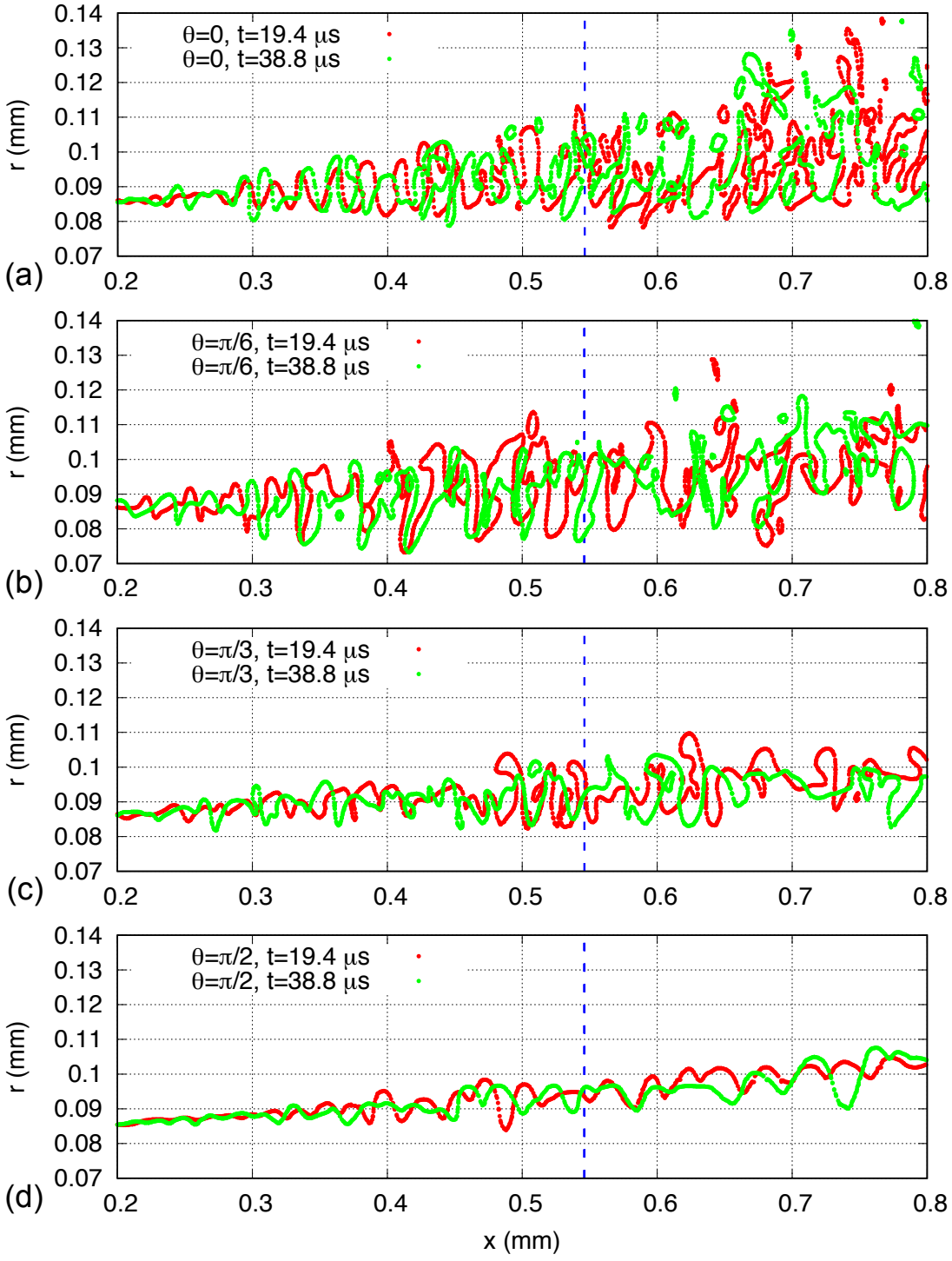


Figure 3.10. Jet surface contours on planes along different azimuthal angles, (a) $\theta = 0$, (b) $\pi/6$, (c) $\pi/3$, and (d) $\pi/2$, respectively. The blue vertical line denotes the position of the outer edge of the counterbore.

asymmetric. It can be observed from the side view that the head tilts more and more along the streamwise direction, see Figs. 3.11(c) and (d).

Due to the faster motion of the top of the jet, the liquid sheet extended from the top of the head experiences a larger aerodynamic drag. The stronger interaction with the surrounding gas results in a faster thinning of the sheets and also the earlier formation of holes in them, see the closeup of Fig. 3.11(e). Holes are first observed around $|\theta| \lesssim \pi/6$. The holes then expand due to the Taylor-Culick rim retraction. When the holes eventually merge, the sheet breaks into small ligaments and droplets. Similar to the droplets formed near the jet core, the droplets are slowed down by the aerodynamic drag and are left behind in the wake of the jet head.

As time elapses, the breakup of the jet head gradually extends toward the lower part. At $t = 19.4$ $\mu$s, the upper half of the head is almost completely broken while the bottom sheet remains relatively smooth. At $t = 38.8$ $\mu$s, the whole jet head is almost completely broken. The liquid velocity in the lower portion of the jet head is lower than the top. Furthermore, when the upper part of the jet head has broken, the gas can go around the head from the top, which further reduces the shear on the lower surface of the jet head. As a result, the interfacial instabilities develop slower and the breakup is less violent at the lower part of the jet head. The droplets formed from the lower part are generally larger than those from the upper part. As will be shown later, this azimuthal variation of breakup dynamics will lead to interesting asymmetric droplets statistics.

### *3.3.6 Turbulent Vortical Structures*

The $\lambda_2$ criterion (Jeong and Hussain, 1995) is used to visualize the vortices generated around the jet, see Fig. 3.12. The iso-surfaces for $D_0\lambda_2/U_0 = -100$ colored by the streamwise velocity at $t = 19.4$ $\mu$s are shown in Figs. 3.12(b) and (d) from two different views. The corresponding gas-liquid interfaces are shown in Figs. 3.12(a) and (c), respectively. The contour of $\lambda_2$ on a 2D plane along $\theta = 0$ is shown in Fig. 3.12(e).

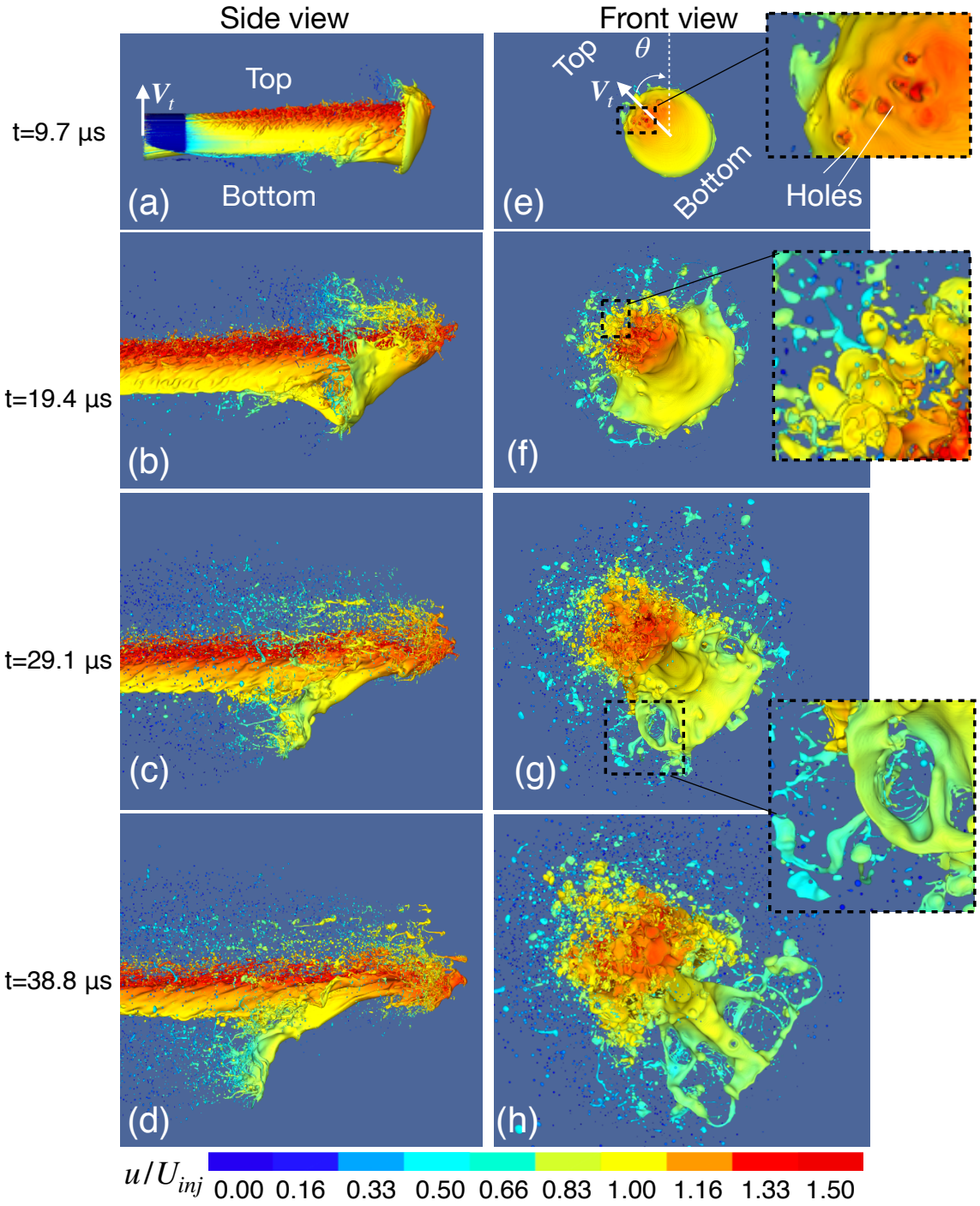


Figure 3.11. Temporal evolution of the jet head from the side (a-d) and front (e-h) views. The gas-liquid interfaces are colored by the streamwise velocity.

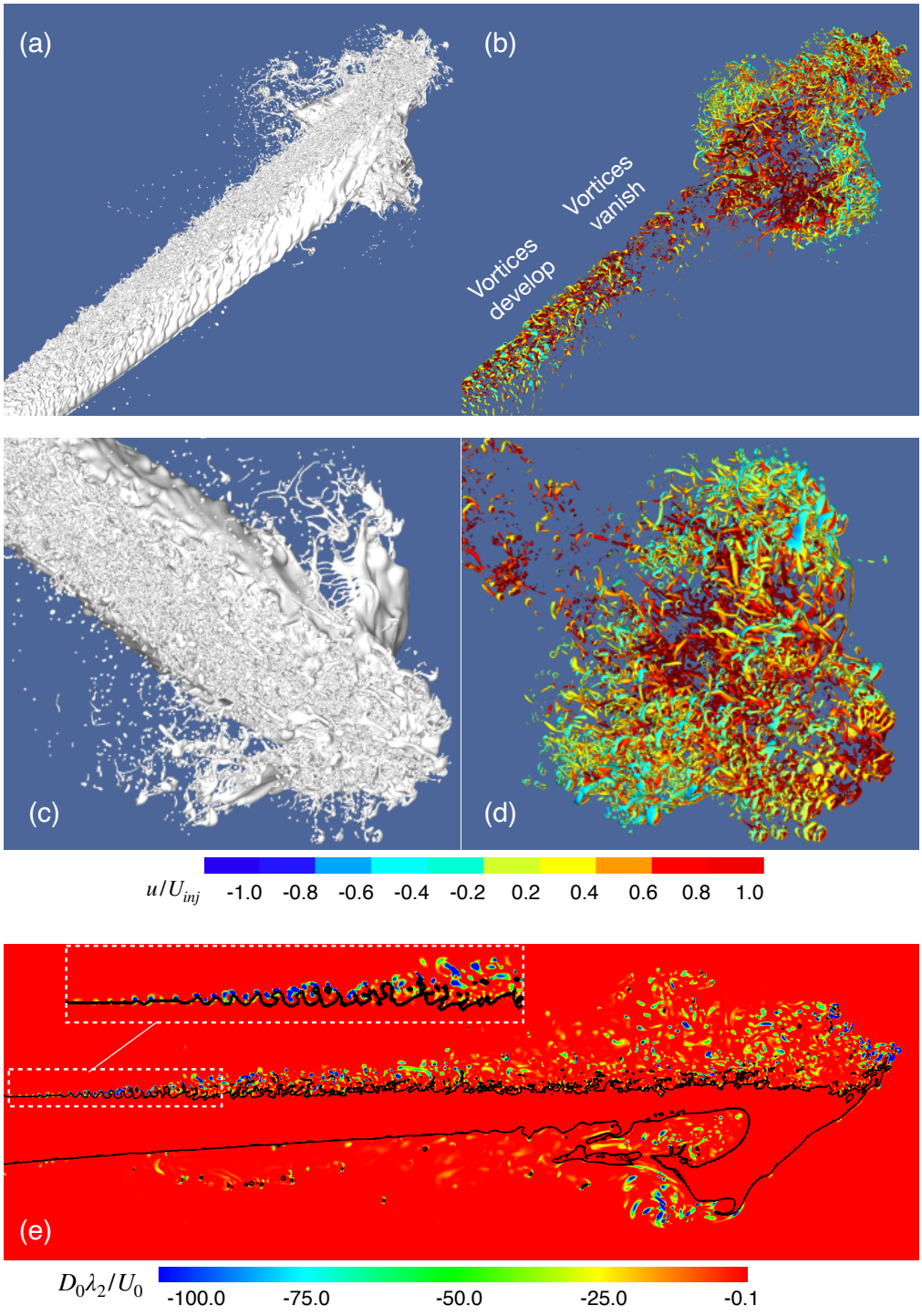


Figure 3.12. Jet surfaces (a,c) and vortical structures (b,d) for $\eta = 0.2$ from different views at 19.4 $\mu$s. The vortices are visualized by the iso-surfaces for $D_0\lambda_2 U_0 = -100$, colored with the streamwise velocity. (e) Contours of $\lambda_2$ on the 2D plane at $\theta = 0$, with the black lines indicating the gas-liquid interfaces.

Vortices are generated due to the shear instability at the interface (Jarrahbashi and Sirignano, 2014; Zandian *et al.*, 2019; Ling *et al.*, 2019). These vortices develop spatially and lead to turbulence. Due to the lower gas viscosity, the vorticity layer near the interface is significantly thinner on the gas side than that on the liquid side. As a result, the gas flow is less stable and the vortices are mainly located in the gas flow, see Fig. 3.12(e).

The evolution of the vortices around the jet core is closely related to the growth of the interfacial waves. Consistent with the observations in previous studies (Ling *et al.*, 2019), as the amplitudes of the interfacial waves grow spatially, more vortices are generated and the swirling strength of the vortices (characterized by the magnitude of $\lambda_2$) increases. After the interfacial waves break, the vortices gradually vanish. The number of vortices reaches its maximum at about $x/D_0 = 5$. Due to the stronger shear at the top of the jet, vortices are concentrated around the upper part of the jet surface.

A large amount of vortices are produced around the jet head, see Fig. 3.12(d). As the gas flows over the head, vortices are formed on the upstream side of the jet head due to the shear instability, similar to those on the surfaces of the jet core. Furthermore, the gas flow separates on the downstream side of the jet head and forms a recirculation region (Shinjo and Umemura, 2010). The recirculation flow itself is also unstable and becomes turbulent. Finally, when the jet head breaks into small ligaments and droplets, vortices are also produced in the wakes of these small liquid structures.

Since the jet is progressively entering the domain, it is infeasible to perform averaging and to calculate the turbulence statistics as in previous studies of turbulent atomization (Ling *et al.*, 2019). Nevertheless, the results here indicate that the turbulence near an atomizing jet is generally far from equilibrium. This non-equilibrium nature must be carefully incorporated to the sub-grid stress model if a LES simulation is to be performed.

### *3.3.7 Droplet Statistics*

In each time snapshot of the simulation results, the individual liquid structures, such as droplets and ligaments, are identified by examining the cells with $f > 0$ that are connected together. During the simulation, the droplets with a volume smaller than $(2\Delta_{x,\min})^3$ are removed, because these droplets are under resolved and removing them is helpful to stabilize the simulation. The temporal and spatial evolutions of the droplet number distributions over the volume-based droplet diameter, $d_v$, are shown in Fig. 3.13. The vertical dashed lines in the figures indicate the cut-off droplet diameter, $d_{v,cut}$. For the L12 mesh, $d_{v,cut} = 3.35$ $\mu$m.

3.3.7.1 *Time evolution of drop statistics.* In order to investigate the azimuthal variation of the droplet number, the droplets are counted in different azimuthal sectors $[\theta - \Delta_\theta/2, \theta + \Delta_\theta/2]$, where $\Delta_\theta$ is the span of $\theta$ for the sector. Due to the symmetry of droplet statistics with respect to the plane for $\theta = 0$, the number of droplets for $\theta$ also include the droplets in the sector for $-\theta$. The number of droplets collected in the azimuthal sector centered at $\theta$ and in the diameter bin centered at $d_v$ is denoted as $N_d(t, d_v, \theta)$, which is a function of $t, d_v$, and $\theta$. Summing $N_d$ over all $\theta$ sectors and $d_v$ bins will yield the total number of droplets at a given time, $N_{tot}(t)$. The temporal evolution of $N_{tot}$ is shown in Fig. 3.13 (a). As the liquid jet progressively enters the domain and breaks into droplets, $N_{tot}$ increases over time. It is interesting to notice that, the temporal growth of $N_{tot}$ exhibits two different scaling laws: at early time ($t \lesssim 27$ $\mu$s) $N_{tot} \approx (tU_0/d_0)^{10/3}$, and at later time ($t \gtrsim 27$ $\mu$s), $N_{tot} \approx 120(tU_0/d_0)^{1.5}$. The two scaling laws reflect the change of the breakup dynamics of the jet over time.

As shown in section 3.3.5, the breakup of the jet head first starts from its upper portion. Since the upper part of the jet head moves with larger velocity, the breakup is more violent, forming smaller droplets. As the liquid volume inflow rate is constant, the smaller droplet sizes will result in a higher rate of increase for droplet number and a faster growing power law, $N_{tot} \sim t^{10/3}$. As time evolves, the breakup of the jet head extends toward the lower part. The breakup of the lower portion of the jet head

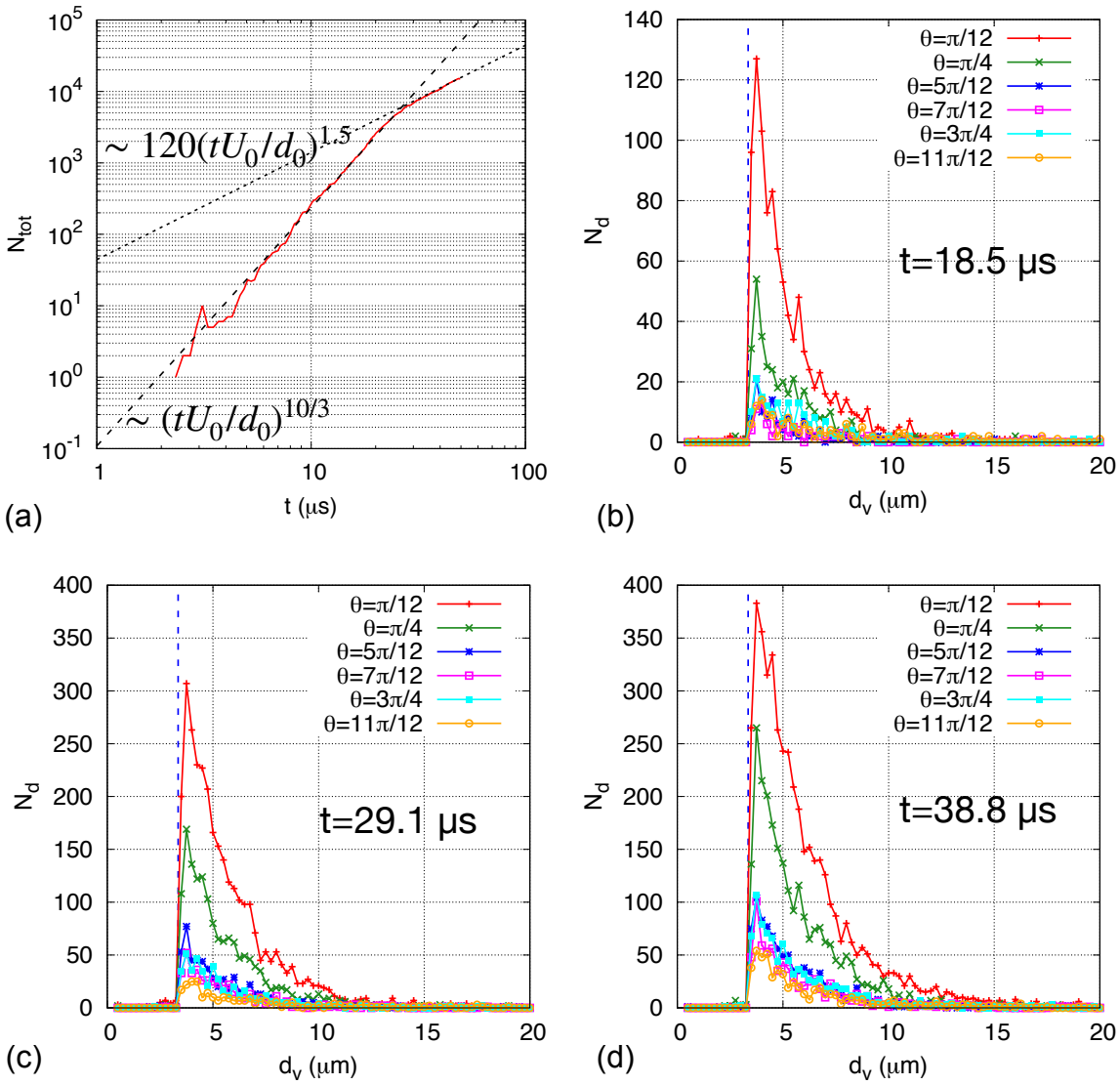


Figure 3.13. Temporal evolutions of (a) the total number of droplets and (b)-(d) size distributions for different azimuthal angles. The vertical dashed lines in (b)-(d) indicate the cutoff droplet diameter $d_{v,cut} = 3.35$ $\mu$m.

is less intense and the droplets formed are generally larger than those formed earlier from the upper portion of the jet head. As a consequence, the rate of increase in droplet number is reduced, as reflected in the slower growing scaling law ($N_{tot} \sim t^{1.5}$).

Since a simulation snapshot contains all the droplets generated up to that time, it is difficult to identify the formation time for individual droplets. In order to investigate the statistics of droplets formed at different times, the distribution of droplet number over $d_v$ and $\theta$ at different times are shown in Figs. 3.13(b)–(d). At $t = 18.5$ $\mu$s, the sector for $\theta = \pi/12$ dominates in $N_d$ and the distribution profile is relatively narrow, concentrating in the range of small $d_v$. This is consistent with the observation in Fig. 3.11 that the majority of the droplets earlier than $t = 18.5$ $\mu$s are from the breakup of the upper portion of the jet head. As a result, the droplets are located mainly at smaller $\theta$. As time evolves, the breakup of the jet head extends to larger $\theta$, and the ratio between $N_d$ for larger and smaller $\theta$ increases. Taking $d_v = 4.5$ $\mu$m as an example, the ratio between $N_d$ for $\theta = \pi/4$ and $\pi/12$ is around 25% at $t = 18.5$ $\mu$s, and the ratio increases to about 55% at $t = 29.1$ $\mu$s. Furthermore, the width of the distribution profile increases from $t = 18.5$ to $t = 38.8$ $\mu$s. This indicates that the droplets formed at later time biased toward larger $d_v$, which is due to the less violent breakup of the lower portion of the jet head.

3.3.7.2 *Self-similar PDF for different azimuthal angles.* Another important observation can be made from Fig. 3.13, *i.e.*, though $N_d$ varies significantly over $\theta$, the shapes of the size-distribution profiles for different $\theta$ are actually quite similar at later time ($t = 29.1$ and $38.8$ $\mu$s). This similarity in distribution profiles for different $\theta$ can be better illustrated by the probability distribution function (PDF) $P$. The PDF of $d_v$ also depends on $\theta$ and $t$, and can be computed as

$$P(d_v, \theta, t) = \frac{N(d_v, \theta, t)}{\Delta_d \sum_d N(d_v, \theta, t)}, \tag{3.21}$$

where $\sum_d N(t, d_v, \theta)$ represents the total number of droplets for $t$ and $\theta$. By definition $\int P \, \mathrm{d}d_v = 1$ for all $t$ and $\theta$.

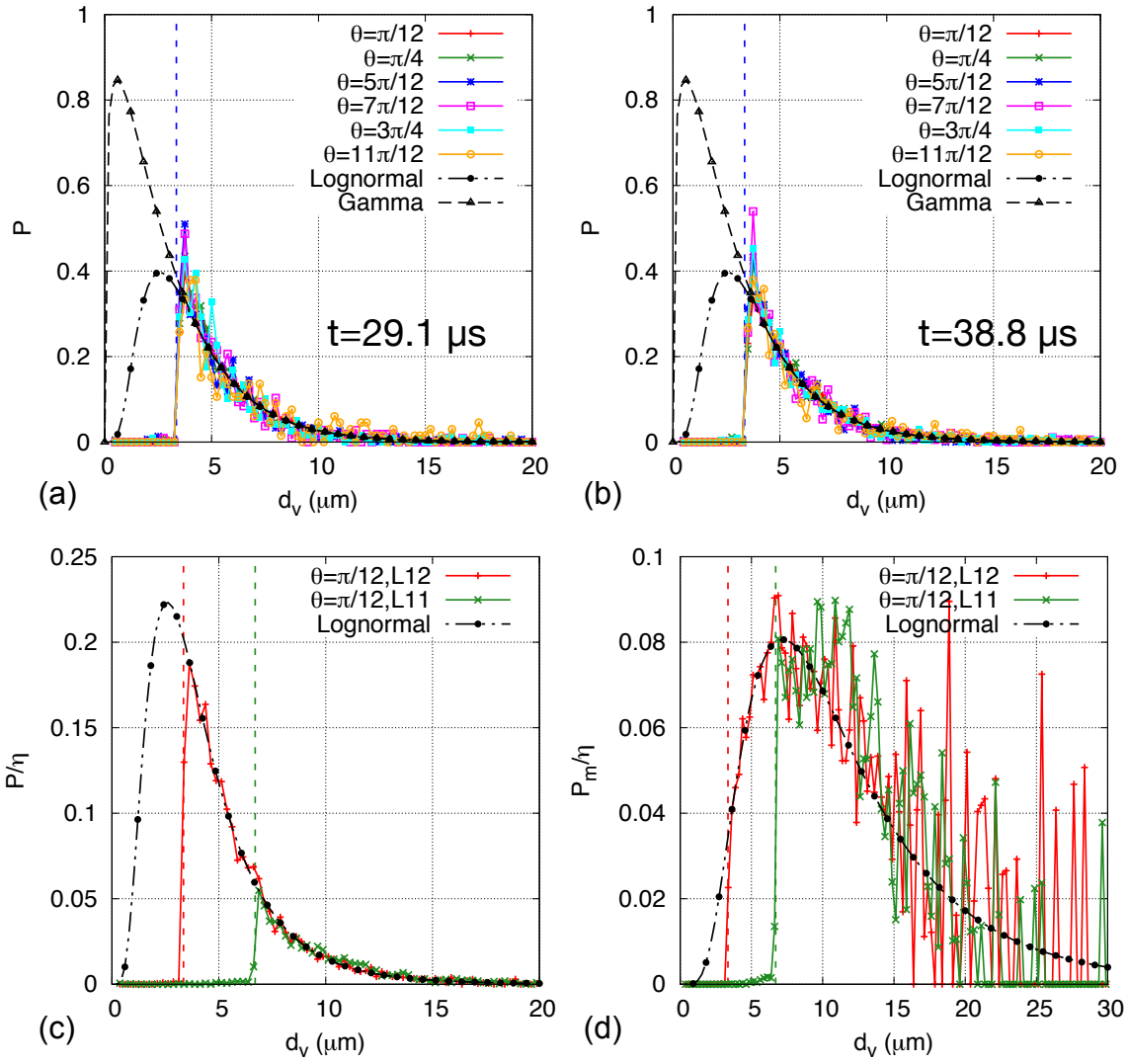


Figure 3.14. Probability distribution functions (PDF) of $d_v$ for different $\theta$ at (a) $t$ =29.1 and (b) 38.8 $\mu$s. The lognormal and gamma functions plotted in both (a) and (b) are fitted based on the results for $\theta = \pi/12$ and $t = 38.8$ $\mu$s and scaled by the correction factors $\eta$. The normalized PDF ($P/\eta$) for the L11 and L12 meshes and $\theta = \pi/12$ at 38.8 $\mu$s are compared with the lognormal function in (c). The droplet mass PDF of $d_v$ for $\theta = \pi/12$ and $t = 38.8$ $\mu$s and the L11 and L12 meshes are shown in (d). The vertical dashed lines indicate the cut-off droplet diameter $d_{v,cut}$ for the corresponding mesh.

It can be observed from Figs. 3.14(a) and (b) that the profiles of $P$ for different $\theta$ tend to collapse for both $t = 29.1$ and 38.8 $\mu$s. In other words, although the droplet number $N_d$ varies significantly over $\theta$, the PDF $P$ does not. Furthermore, the collapsed profile of $P$ varies little over time. As a result, $P$ at later time can be approximated by a self-similar form, $P_{sim}$, namely

$$P(d_v, \theta, t) \approx P_{sim}(d_v)\,, \tag{3.22}$$

while $P_{sim}$ is only a function of $d_v$ and does not depend on $t$ and $\theta$.

3.3.7.3 *Estimate for the statistics of under-resolved droplets.* It can be observed from Fig. 3.14 that, the peaks of $P$ are right next to $d_{v,cut}$, which seems to indicate that there exist droplets that are under resolved ($d_v < d_{v,cut}$) in the present simulation. In order to estimate the statistics of these under-resolved droplets, the model distribution functions, including the lognormal and gamma distribution functions, are employed to fit the PDF for resolved droplets ($d_v > d_{v,cut}$). The expressions for the lognormal and gamma distributions are given as

$$P_L(d_\mathrm{v}) = \frac{\eta}{d_\mathrm{v}\hat{\sigma}\sqrt{2\pi}} \exp\left[ -\frac{(\ln d_\mathrm{v} - \hat{\mu})^2}{2\hat{\sigma}^2} \right], \tag{3.23}$$

where $\hat{\mu}$ and $\hat{\sigma}^2$ are the mean and variance of $\ln d_\mathrm{v}$, and

$$P_G(d_\mathrm{v}) = \eta \frac{\hat{\beta}^{\hat{\alpha}}}{\Gamma(\hat{\alpha})} d_\mathrm{v}^{\hat{\alpha}-1} \exp(-\hat{\beta} d_\mathrm{v}) \tag{3.24}$$

where $\hat{\alpha} = (\tilde{\mu}/\tilde{\sigma})^2$ and $\hat{\beta} = \hat{\alpha}/\tilde{\mu}$ with $\tilde{\mu}$ and $\tilde{\sigma}^2$ the mean and the variance of $d_\mathrm{v}$, respectively. The correction factor $\eta$ is introduced to account for the under-resolved droplets. The lognormal and gamma profiles plotted in Figs. 3.14(a) and (b) are based on the results for $d_v \in [4 : 20]$ $\mu$m and $\theta = \pi/12$ at $t = 38.8$ $\mu$s. The fitting parameters are $(\hat{\mu}, \hat{\sigma}) = (1.29, 0.58)$ and $(\hat{\alpha}, \hat{\beta}) = (1.26, 0.44)$ for the lognormal and gamma functions, respectively. It can be observed that the fitted profiles agree well with results of $P$ for different $t$ and $\theta$.

The correction factors for the lognormal and gamma distributions are $\eta$ =1.8 and 3.2, respectively. If we assume that the PDF for the droplets generated followed

the lognormal or gamma distributions, the percentages of the under-resolved droplets in terms of number are about $(\eta - 1)/\eta$=44% and 69%, respectively. Previous numerical and experimental studies have shown that the lognormal function fits better the gradual decay of $P$ for larger $d_v$ (Sotolongo-Costa *et al.*, 1996; Ling *et al.*, 2017). The diameter at the peak of $P$ estimated by the lognormal function is about $d_v$ =2.6 $\mu$m, which is about twice of $\Delta_{x,\min}$ and is slightly smaller than $d_{v,cut}$ = 3.35 $\mu$m for the L12 mesh.

The results for the normalized PDF, namely $P/\eta$, are shown in Fig. 3.14(c). The simulation results for the L11 and L12 meshes ($\theta = \pi/12$ and $t$ = 38.8 $\mu$s) are compared with the lognormal function. The integration of the normalized lognormal function $\int_0^\infty (P_L/\eta)\mathrm{d}d_v = 1$. The correction factor $\eta$ for the L11 mesh results is about 6.5. In other words, when the coarser L11 mesh is used, the percentage of under-resolved droplets increases to about 85%. Nevertheless, it is observed that the normalized PDF for the resolved droplets for the L11 mesh agrees well with the PDF for the L12 mesh and also the lognormal function. This seems to indicate that the statistics of the droplets is not influenced by leaving some small droplets under resolved, assuming that the important primary breakup processes (such as the interfacial waves and the jet head breakups) are reasonably captured.

Furthermore, the percentage of under-resolved droplets may seem to be high in terms of number, but actually they take only a small portion of the total mass (or volume) of the droplets formed. The droplet mass PDF of $d_v$, $P_m$, is defined as

$$P_m(d_v, t, \theta) = \frac{m(d_v, \theta, t)}{\Delta_d \sum_d m(d_v, \theta, t)} \tag{3.25}$$

where $m(d_v, \theta, t)$ denotes the total mass of droplets for $d_v, \theta$ and $t$. Since the droplet fluid density is taken to be constant, so $P_m$ can be related to $P$ as

$$P_m(d_v, t, \theta) = \frac{N(d_v, \theta, t) d_v^3}{\Delta_d \sum_d [N(d_v, \theta, t) d_v^3]} = P_d \frac{d_v^3}{\langle d_v^3 \rangle} \tag{3.26}$$

where

$$\langle d_v^3 \rangle = \int_0^\infty P(d_v) d_v^3 \mathrm{d}d_v \tag{3.27}$$

is the mean of $d_v^3$ and it is computed that $\langle d_v^3 \rangle$ =220.57 $\mu$m$^3$ according to the fitted lognormal function. The results of $P_m$ for $\theta = \pi/12$, $t = 38.8$ $\mu$s, and the L11 and L12 meshes are shown in Fig. 3.14(d). The simulation results for $P_m$ are more noisy due to the factor of $d_v^3$. The peak of $P_m$ can be identified at about $d_v = 7$ $\mu$m, which is about the $d_{v,cut}$ for the L11 mesh and is about twice the $d_{v,cut}$ (about four times of $\Delta_{x,min}$) for the L12 mesh. More important, it can be computed from the lognormal fit that the percentage of the under-resolved droplets in terms of droplet mass for the L12 mesh is about 3.1%, which is actually quite small. Therefore, the present simulation with the finer L12 mesh does capture the majority of droplets in terms of mass or volume.

3.3.7.4 *PDF for azimuthal angle.* The PDF of the azimuthal angle $\theta$ is defined as

$$Q(\theta, t) = \frac{\sum_d N(d_v, \theta, t)}{\Delta_\theta N_{tot}(t)}\,, \tag{3.28}$$

which is a function of $\theta$ and $t$. It can be shown that $\int_0^\pi Q \mathrm{d}\theta = 1$ for all $t$. The results for $Q$ at different times are plotted in Fig. 3.15. Similar to $P$, it is observed that $Q$ varies only slightly over time for $t \gtrsim 29.1$ $\mu$s, so we can approximate $Q$ with a similar profile that depends on $\theta$ only

$$Q(t, \theta) \approx Q_{sim}(\theta)\,. \tag{3.29}$$

The variation of $Q$ over $\theta$ reflects the asymmetric breakup dynamics of the jet head and the jet core.

It is worth noting that the droplets have a small azimuthal velocity when they are just generated, so the change of droplet location in the $\theta$ coordinate is generally small. The hyperbolic tangent function well captures the decrease of $Q_{sim}$ over $\theta$ between 0 and $\pi/2$. There exist mild variations of $Q_{sim}$ between $\theta = \pi/2$ and $\pi$, but the amplitudes of those variations are much smaller than the change from $\theta = 0$ to $\pi/2$. The hyperbolic tangent function fitted based on the data at $t$ =38.8 $\mu$s is given

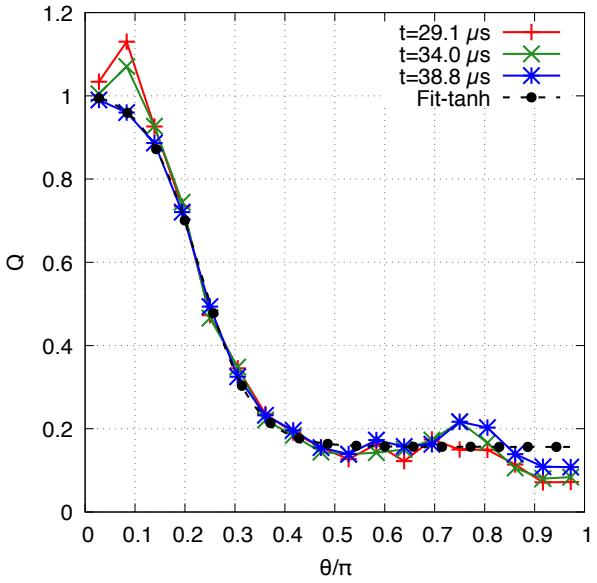


Figure 3.15. The PDF of droplet number for the azimuthal angle $\theta$ at different times. The fitted function is a hyperbolic tangent function.

as

$$Q_{sim}(\theta) \approx 0.0429 \tanh[-9.29(\theta/\pi - 0.229)] + 0.585\,, \tag{3.30}$$

which is plotted in Fig. 3.15 and is shown to be a good approximation of $Q$.

3.3.7.5 *Model to estimate droplet number.* Finally, the results obtained previously for (1) the time scaling law for the total number of droplets $N_{tot}(t)$ at later time, *i.e.*, $N_{tot} \approx 120(tU_0/d_j)^{1.5}$, (2) the self-similar PDF of droplet diameter, $P_{sim}(d_v)$, which is approximated by the lognormal function $P_L(d_v)$ (Eq. (3.23) with $(\eta, \hat{\mu}, \hat{\sigma}) = (1.8, 1.29, 0.58)$), and (3) the self-similar PDF for the azimuthal angle, $Q_{sim}(\theta)$ (Eq. (3.30)), lead to a useful model to estimate the number of droplets in any droplet size bin and azimuthal angle sector at later time of the primary breakup ($t \gtrsim 27$ $\mu$s):

$$N_{est}(t, d_v, \theta) = N_{tot}(t) Q_{sim}(\theta) P_{sim}(d_v) \Delta_\theta \Delta_d. \tag{3.31}$$

The droplet numbers for different $d_v, \theta$, and $t$ estimated by the model (Eq. (3.31)) are compared with the simulation results in Fig. 3.16. The data plotted here include three time snapshots at $t = 29.1$, 39.5 and 38.8 $\mu$s for the droplet diameter range from 3.5

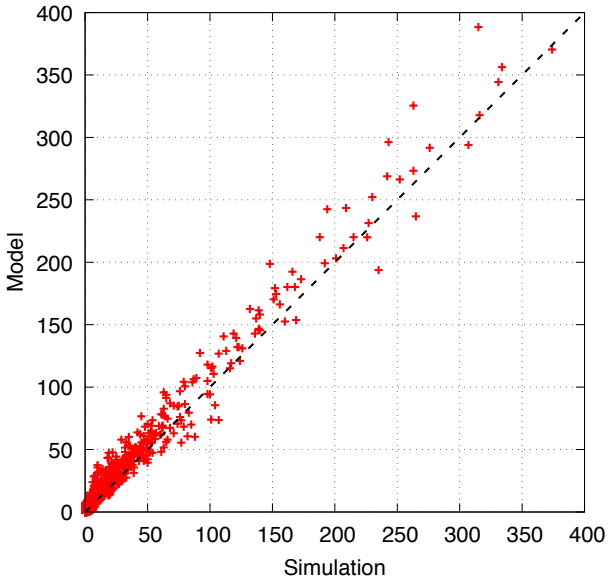


Figure 3.16. The number of droplets estimated by the model (Eq. (3.31)) are compared with the simulation results. The range of droplet size is $3.5 < d_v < 30$ $\mu$m, and the bin width is $\Delta_d = 0.25$ $\mu$m. The angle of the azimuthal sector $\Delta_\theta = \pi/6$. The data plotted include three time snapshots at $t = 29.1$, 39.5 and 38.8 $\mu$s.

to 30 $\mu$m. The bin width for $d_v$ is $\Delta_d = 0.25$ $\mu$m and the angle of the azimuthal sector $\Delta_\theta = \pi/6$. It is clearly shown that the model yields good estimates to the simulation results. The model exhibited a simple explicit form and accurately captures the droplets number distribution over $d_v, \theta$, and $t$, therefore, it is very useful in practical applications. For example, the model can be applied to specify the conditions of droplets at the inlet in a Lagrangian spray simulation where the primary breakup process is not directly simulated.

## *3.4 Conclusions*

The primary breakup of a gasoline surrogate jet is investigated through detailed numerical simulation. The interfacial two-phase flow is resolved using the *Basilisk* solver with a momentum-conserving volume-of-fluid method. The injection conditions are similar to the Engine Combustion Network (ECN) Spray G operating conditions. To focus the computational resources on resolving the liquid jet, the injector geometry is simplified. The effect of the internal flow in the injector on the jet dynamics is

modeled through a nonzero injection angle specified at the inlet. A parametric study is performed for the injection angle. The simulation results for different injection angles are compared with the experimental measurements for the jet penetration length and the jet deflection angle to identify the injection angle ($\eta = \tan\alpha = 0.2$) that best represents the Spray G conditions. The effects of the inlet boundary condition, numerical method, and mesh resolution are systematically investigated, affirming that the simulation approach is effective in resolving both the macro-scale and micro-scale breakup features. The nonzero injection angle introduces an azimuthally varying velocity within the liquid jet. As a consequence of that, the shear-induced interfacial waves on the jet core and the formation of liquid lobes and fingers become strongly asymmetric: the wavelengths for the longitudinal waves on the top of the jet are significantly smaller than those on the lateral sides. The deformation and breakup of the jet head are also influenced by the non-uniform velocity. Since the upper portion of the jet head moves faster than the lower portion, the jet head tilts in the streamwise direction and furthermore, the upper portion breaks earlier and more violently than the lower portion. This time-dependent and asymmetric breakup dynamics of the jet head results in two different scaling laws for the total droplet number at the early and later times. While the former scaling law corresponds to the smaller droplets generated from the earlier and more violent breakup of the upper portion of the jet head, the latter is dictated by larger droplets produced by the later breakup of the lower portion of the jet head. The distribution of the droplet number over the volume-based droplet diameter is presented as a function of time and azimuthal angle $\theta$. Though the droplet-number distribution varies significantly over $\theta$, the probability density functions (PDF) for different $\theta$ collapse to a self-similar profile. The self-similar PDF is fitted with both the lognormal and gamma distribution functions. The results for PDF suggest that there exist droplets that are smaller than the cut-off droplet diameter (droplet volume smaller than $(2\Delta_{x,min})^3$) and thus are under resolved in the present simulation. The PDF for the resolved droplets for the L11

and L12 meshes agree well with the lognormal function, indicating that the size-distribution of resolved droplets are not influenced by leaving some tiny droplets under resolved, assuming the mesh resolution is fine enough to capture the important micro-scale breakup features like the interfacial waves and the jet head deformation. The percentage and statistics of the tiny under-resolved droplets are estimated through the lognormal function. It is shown that about 3.1% of the total droplet mass are under resolved by the L12 mesh. The PDF of the azimuthal angle is also presented. The decrease of PDF over the azimuthal angle is well represented by a hyperbolic tangent function. Both the PDF of $d_v$ and $\theta$ vary little over time at later time ($t \gtrsim 27$ $\mu$s). Based on these self-similar PDF, a model has been proposed to predict the droplet number for an arbitrary droplet diameter and azimuthal angle at later time of the primary breakup. The model predictions are shown to agree well with the simulation results.

The present study has only simulated for a short physical time, compared to the whole injection duration of the spray G operation conditions. Therefore, the atomizing jet in the computation domain has not reached a statistically stationary state. To measure time-average two-phase turbulent flow properties, the simulation needs to be run for a much longer time (twice or even more). Such a simulation will be relegated to the future work.

# CHAPTER FOUR

## Direct Numerical Simulation of Compressible Interfacial Multiphase Flows Using a Mass-Momentum Consistent Volume-Of-Fluid Method

### *4.1 Introduction*

Compressible interfacial multiphase flows are present in a wide array of applications, such as lithotripsy, cavitation, raindrop damage in supersonic flight, and scramjet propulsion systems. As a bulk liquid is subjected to a supersonic gas flow, the liquid breaks due to the strong interaction with the gas flow. Liquid atomization in supersonic flows involves rich and complex physics. In the past, experiments have been the primary means to investigate underlying mechanisms. However, since the resulting multiphase flows involve complex topology changes that evolve at a very high speed, many flow details are still too difficult to measure even with the most advanced experimental diagnostics today. Therefore, numerical simulation is a necessary supplement to shed light on the unclear flow physics. Nevertheless, numerical simulation of liquid breakups in supersonic flows is also challenging since rigorous numerical methods are required to capture the material interfaces, shock waves, and surface tension on interfaces. The liquid breakups are usually initiated by the small-scale instabilities, including Kelvin-Helmholtz, Rayleigh-Taylor, and Richtmyer-Meshkov instabilities, near the interfaces, a high-mesh resolution is required to yield high-fidelity simulation results.

In order to capture the interfaces separating different fluids or phases involved in the interfacial multiphase flows, different interface tracking/capturing methods have been developed in the past, including the lattice Boltzmann method (Lee and Liu, 2010; Leclaire *et al.*, 2013; Liu *et al.*, 2014), the arbitrary Lagrangian-Eulerian method (Corot *et al.*, 2020; Hu *et al.*, 2001; Luo *et al.*, 2004), the front-tracking method (Unverdi and Tryggvason, 1992; Tryggvason *et al.*, 2001; Bo *et al.*, 2011), the level-

set method (Osher and Sethian, 1988; Osher and Fedkiw, 2001; Sethian and Smereka, 2003), and the volume-of-fluid method (Hirt and Nichols, 1981; Lafaurie *et al.*, 1994; Scardovelli and Zaleski, 1999). While the level-set method has the advantage that interface normal vector and curvature can be conveniently calculated, the conventional level-set methods suffer from not conserving mass. In contrast, mass is conserved by the volume-of-fluid method, which is essential to atomization simulation.

A wide array of shock-capturing schemes (LeVeque, 2002) have been developed to capture the shock waves and other sharp discontinuities in compressible flows. The key feature of shock-capturing methods is to suppress the spurious oscillations developed near the shocks and material interfaces without contaminating the regions with smooth flow properties. The classic Godunov's method takes advantage of the solution of the Riemann problem to compute the flux at the cell surfaces (Godunov, 1959). Approximate Riemann solvers have been developed to reduce the computational cost, since obtaining exact solution for the Riemann solvers is computationally expensive (Toro *et al.*, 1994). The pioneering work of developing approximate Riemann solvers can be traced back to those by Harten and Lax (Harten and Lax, 1981), Roe (Roe, 1981), and Toro (Toro, 2001).

To simulate compressible flows that involve multiple phases, sophisticated equations of state are required. Shyue (Shyue, 1998) numerically solved the set of quasi-conservative compressible Euler equations with a stiffened gas equation of state and extended the approximate Riemann solver of Roe from single-component to multi-component flows.

Johnsen and Colonius (Johnsen and Colonius, 2006) incorporated the Mie-Gruneisen equation of state in the Harten Lax van Leer Contact (HLLC) approximate Riemann solver, which overcomes the issue of not preserving positivity in the Roe's solver. They have also used weighted essentially non-oscillatory (WENO) scheme to reconstruct flow properties in a cell (Liu *et al.*, 1994). The volume-of-fluid method was used by Coralic and Colonius (Coralic and Colonius, 2014) to track the interfaces,

and the mass conservation issue in the earlier version of the method (Johnsen and Colonius, 2006) was significantly improved.

Surface tension is important to atomization and droplets formation, and thus must be incorporated rigorously in numerical simulation (Popinet, 2018). One of the most successful methods in the literature was developed by Popinet (Popinet, 2009), in which the interface curvature was calculated based on the generalized height function method and the surface tension is discretized by the balanced-force approach (Francois *et al.*, 2006). The accuracy and efficiency of this method is demonstrated by successful simulations for a wide range of interfacial multiphase flows, including droplet impact (Josserand *et al.*, 2016), drop formation and oscillation (Zhang *et al.*, 2019), and liquid jet atomization (Zhang *et al.*, 2020). Incorporating surface tension in a compressible multiphase flow simulation is an emerging area, and only few studies can be found in the literature. Garrick *et al.* (Garrick *et al.*, 2017) extended the HLLC solver to simulate the compressible multiphase flow with capillary forces, using the continuum surface force (CSF) model. Instead of using a typical geometric VOF method, they have used the Tangent of Hyperbola for Interface Capturing (THINC) method for interface reconstruction. Their methods were used to simulate the primary breakup of a liquid jet in a supersonic crossflow (Garrick *et al.*, 2017). Corot *et al.* (Corot *et al.*, 2020) has used the ALE method to solve the two-phase compressible Euler equation with surface tension to study Richitmyer-Meshkov instability. Schmidmayer *et al.* also modeled the surface tension using the CSF method (Schmidmayer *et al.*, 2017) and their methods were tested by the aerobreakup of a water column in a compressible flow.

More recently Fuster and Popinet (FP) presented an all-Mach method for simulation of compressible multiphase flows with surface tension (Fuster *et al.*, 2018). A key feature of the method is that the conservative variables and volume fraction are advected in a consistent manner. The method was used to simulate the collapse of an air bubble in liquid and a good agreement with experiment was achieved. An

issue of their method is that the spurious oscillations are observed near the shocks, indicating that the current method in computing the nonlinear convection term is not sufficient to suppress the numerical oscillations. Hence, in the present study we are going to extend the FP method by including additional numerical diffusion following the central upwind method of Kurganov and Tadmor (Kurganov and Tadmor, 2000; Kurganov *et al.*, 2001; Kurganov and Levy, 2002). The numerical diffusion will only be introduced in the region away from the interface, so the interface remains sharp. As will be shown later, the improved method is successful in reducing oscillations in the original FP method.

The remainder of the manuscript is organized as follows. The governing equations are presented in section 4.2. The numerical methods are explained in section 4.3. A wide range of compressible multiphase flows are used to validate the numerical methods, and the results will be presented and discussed in section 4.4. Finally the conclusions will be drawn in section 4.5.

## *4.2 Governing Equations*

The one-fluid approach is used, where the liquid and the gas are treated as one fluid with material properties that jump abruptly across the interface. The Naiver-Stokes equations for two-phase compressible flows with surface tension are given as

$$\frac{\partial \rho}{\partial t} + \frac{\partial \rho u_i}{\partial x_i} = 0\,, \tag{4.1}$$

$$\frac{\partial \rho u_i}{\partial t} + \frac{\partial \rho u_i u_j}{\partial x_j} = -\frac{\partial p}{\partial x_i} + \frac{\partial \tau_{ij}}{\partial x_j} + \sigma\kappa\delta_s n_i\,, \tag{4.2}$$

$$\frac{\partial E}{\partial t} + \frac{\partial E u_i}{\partial x_i} = -\frac{\partial p u_i}{\partial x_i} + \frac{\partial \tau_{ij} u_i}{\partial x_i} + \sigma\kappa\delta_s n_i u_i\,, \tag{4.3}$$

where $\rho$, $\mu$, $u$, $p$, and $E = \rho e + \frac{1}{2}\rho u^2$ represent density, viscosity, velocity, pressure, and total energy respectively, and $e$ is the internal energy. Furthermore, $\tau_{ij} = \mu(\partial_j u_i + \partial_i u_j) - 2/3\mu\partial_k u_k \delta_{ij}$ is the viscous stress tensor, $\delta_{ij}$ is the Kronecker delta, $\kappa$ and $n_i$ are the local curvature and unit normal vector of the interface, and $\delta_s$ is the Dirac distribution function localized on the interface. The surface tension coefficient $\sigma$ is taken as constant in the present study.

The stiffened equation of state (EOS) in the Mie-Grüneisen form is employed,

$$\rho e = \frac{p + \gamma \Pi_\infty}{\gamma - 1}\,, \tag{4.4}$$

where $\gamma$ is the specific heat ratio and $\Pi_\infty$ is the reference pressure. When $\Pi_\infty = 0$, the Mie-Grüneisen EOS reduces to the ideal gas EOS. The values of $\gamma$ and $\Pi_\infty$ for a given material are obtained by fitting the corresponding shock compression experimental data (Marsh, 1980). The speed of sound is given by

$$c = \sqrt{\gamma \frac{p + \Pi_\infty}{\rho}}\,. \tag{4.5}$$

The two different phases are distinguished by a characteristic function $\chi$, and the temporal evolution of which satisfies the advection equation

$$\frac{\partial \chi}{\partial t} + u_i \frac{\partial \chi}{\partial x_i} = 0\,. \tag{4.6}$$

## *4.3 Numerical Methods*

The governing equations are solved in the framework of the finite volume approach. The present method is based on the FP method (Fuster *et al.*, 2018). Additional artificial numerical diffusion is added in the region away from the interface. The numerical diffusion is computed based on the KT method (Kurganov and Levy, 2002).

### *4.3.1 VOF Advection*

The advection equation (Eq. (4.5)) can be expressed in the conservative form

$$\frac{\partial \chi}{\partial t} + \frac{\partial (\chi u_i)}{\partial x_i} = \chi \frac{\partial u_i}{\partial x_i}\,. \tag{4.7}$$

For incompressible flows, the term on the right hand side is zero. In the volume-of-fluid (VOF) method, Eq. (4.7) is solved in the integral form

$$\Delta\Omega \frac{\partial f}{\partial t} + \oint_{\partial\Omega} \chi u_i n_i \mathrm{d}s = \int_\Omega \chi \frac{\partial u_i}{\partial x_i} \mathrm{d}V\,, \tag{4.8}$$

where $\Delta\Omega$ is the cell volume, and $\partial\Omega$ represents the surface of the cell. The mean value of $\chi$ in the cell is denoted by $f$,

$$f = \frac{1}{\Delta\Omega} \int_\Omega \chi dV\,, \tag{4.9}$$

which represents the volume fraction of liquid in the cell. The fluid density and viscosity can then be calculated as

$$\rho = \rho_l f + \rho_g (1 - f)\,, \tag{4.10}$$

$$\mu = \mu_l f + \mu_g (1 - f)\,. \tag{4.11}$$

In the finite-volume method, the volume fraction advection equation can be written in a discrete direction-split form as follows,

$$\Delta\Omega \frac{f^{n+1} - f^n}{\Delta t} + \Delta_i F_{f,i} = \chi_c \frac{\partial u_i}{\partial x_i} \Delta\Omega\,, \tag{4.12}$$

where $\Delta_i F_{f,i}$ denotes the net flux along the $i^{th}$ direction and the flux of $f$ on a cell surface iscomputed as

$$F_{f,i} = f_a u_{f,i} S\,, \tag{4.13}$$

where $f_a$ represents the volume fraction of liquid to be advected across the cell surface, $u_{f,i}$ is the velocity at the cell surface, and $S$ is the cell surface area. As demonstrated by Weymouth and Due (Weymouth and Yue, 2010), $\chi_c$ is the value of $\chi$ at the cell center (evaluated as $\chi_c = 1$ if $f > 0.5$ and $\chi_c = 0$ if $f \leq 0.5$) and is required to be constant for all sweeping directions to ensure the exact mass conservation. In order to calculate the flux of the volume fraction across the cell face, the interface is reconstructed by the piecewise linear interface construction (PLIC) method (Scardovelli and Zaleski, 1999). The fraction of the reference phase crossing the cell surface, namely $f_a$, is evaluated based on the geometric reconstruction (Scardovelli and Zaleski, 1999).

### *4.3.2 Convection of Conservative Variables*

To solve the convection terms in the conversation laws (Eqs. (4.1)-(4.3)), an advection method that is consistent with the VOF method described above is used. The conservative variables are advected as tracers associated with the volume-fraction of the corresponding phase non-diffusively (López-Herrera *et al.*, 2015). In other words, the conservative variables $\vec{U} = \{\rho, \rho u_i, E\}$ are split into two groups, *i.e.*,

$\vec{U}_l = \{f\rho_l, \rho_l u_i, E_l\}$ for the liquid phase and $\vec{U}_g = \{\rho_g, \rho_g u_i, E_g\}$ for the gas phase and $\vec{U}_l$ and $\vec{U}_g$ are advected as tracers with $f$ and $(1-f)$, respectively.

Time integration of the conservative variables based on the convection terms in Eqs. (4.1)-(4.3) can be written in a discrete direction-split form similar to Eq. (4.12) as

$$\Delta\Omega \frac{\vec{U}^* - \vec{U}^n}{\Delta t} = \Delta_i \vec{F}_{U,i} \tag{4.14}$$

where $\Delta_i \vec{F}_{U,i}$ is the net flux in $i^{th}$ directions and the fluxes of $\vec{U}_l$ and $\vec{U}_g$ at the cell surfaces for the liquid and gas phases are

$$\vec{F}_{Ul,i} = f_a u_{f,i} \vec{U}_{a,i} S = \vec{U}_{a,i} F_{f,i}\,, \tag{4.15}$$

and

$$\vec{F}_{Ug,i} = (1-f_a) u_{f,i} \vec{U}_{a,i} S \tag{4.16}$$

respectively, where $\vec{U}_{a,i}$ is the value of the $i^{th}$ tracer to be advected across the cell surface. The value of the tracer on the upwinded side of the cell surface was used for $\vec{U}_{a,i}$. Linear reconstruction of $\vec{U}_{a,i}$ within the cell is based on the Bell-Colella-Glaz scheme (Bell *et al.*, 1989). For example, the conservative variables for liquid phase can be computed as (Fuster *et al.*, 2018)

$$\vec{U}_{a,i} = \begin{cases} \frac{U_j^n}{f_{j+i}^n} + \frac{1}{2}\min(1, 1-su_n) s \frac{\partial U_j^n}{\partial x_i} \Delta x_i, & \text{if } f_{j+i}^n > 0 \\ 0 & \text{otherwise,} \end{cases} \tag{4.17}$$

$$u_n = \frac{u_{f,i}\Delta t}{\Delta x}\,, i = -\frac{\text{sign}(u_n)+1}{2}\,, s = \text{sign}(u_n)\,, \tag{4.18}$$

where the slope $\frac{\partial U_j^n}{\partial x_i}$ is computed as follows,

$$\frac{\partial U_j^n}{\partial x_i} = \begin{cases} \frac{1}{\Delta x}\text{minmod}\left(\frac{U_{j-1}^n}{f_l}, \frac{U_j^n}{f_c}, \frac{U_{j+1}^n}{f_r}\right), & \text{if } f_l,\, f_c,\, f_r \geq 0.5 \\ \frac{1}{\Delta x}\left(\frac{U_{j+1}^n}{f_r} - \frac{U_j^n}{f_c}\right), & \text{if } f_c,\, f_r \geq 0.5,\, f_l < 0.5 \\ \frac{1}{\Delta x}\left(\frac{U_j^n}{f_c} - \frac{U_{j-1}^n}{f_l}\right), & \text{if } f_c \geq 0.5,\, f_l \geq 0.5 \\ 0, & \text{otherwise,} \end{cases} \tag{4.19}$$

where $f_l = f^n_{j-1}$, $f_c = f^n_j$ and $f_r = f^n_{j+1}$ represent the volume fractions of liquid in the left, center and right cells, and "minmod" represents the minmod slope limiter defined as

$$\text{minmod}(x_1, x_2, x_3) = \begin{cases} \min(\theta(x_2 - x_1), \frac{1}{2}(x_3 - x_1), \theta(x_2 - x_1)), & \text{if } x_1 < x_2 < x_3 \\ \max(\theta(x_2 - x_1), \frac{1}{2}(x_3 - x_1), \theta(x_2 - x_1)), & \text{if } x_1 > x_2 > x_3 \\ 0, & \text{otherwise,} \end{cases} \tag{4.20}$$

where $1 \leq \theta \leq 2$. For $\theta = 1$, the above expression reduces to the classic minmod limiter and for $\theta = 2$, it gives the superbee limiter.

After the advection, the conservative variables can be computed based on the tracers $\vec{U}_l$ and $\vec{U}_g$ as

$$\rho^* = (f\rho_l)^* + ((1-f)\rho_g)^*\,, \tag{4.21}$$

$$(\rho u_i)^* = (f\rho_l u_i)^* + ((1-f)\rho_g u_i)^*\,, \tag{4.22}$$

$$E^* = (fE_l)^* + ((1-f)E_g)^*\,. \tag{4.23}$$

### *4.3.3 Surface Tension and Viscous Stresses*

Explicit method is used in the time integration of the viscous terms in both the momentum and energy equations (Eqs. (4.2) and (4.3)),

$$\frac{(\rho u_i)^{**} - (\rho u_i)^*}{\Delta t} = \frac{\partial \tau_{ij}}{\partial x_i}\,. \tag{4.24}$$

$$\frac{E^{**} - E^*}{\Delta t} = \frac{\partial \tau_{ij} u_i}{\partial x_i}\,. \tag{4.25}$$

The central difference method is used to obtain the spatial discretization of $\frac{\partial \tau_{ij}}{\partial x_i}$ and $\frac{\partial \tau_{ij} u_i}{\partial x_i}$.

For surface tension, the curvature $\kappa$ is computed by the height-function method, the balanced-force discretization is used (Francois *et al.*, 2006; Popinet, 2009)

$$\frac{(\rho u_i)^{***} - (\rho u_i)^{**}}{\Delta t} = \sigma\kappa\frac{\partial f}{\partial x_i}\,, \tag{4.26}$$

$$\frac{E^{***} - E^{**}}{\Delta t} = \sigma\kappa\frac{\partial f}{\partial x_i}u_i\,. \tag{4.27}$$

### *4.3.4 Helmholtz-Poisson Equation for Pressure*

The internal energy equation can be written in terms of pressure as

$$\frac{1}{\rho c_{\text{eff}}^2}\left(\frac{\partial p}{\partial t}+u_i\frac{\partial p}{\partial x_i}\right)-\frac{\beta_T\Phi_\nu}{\rho c_p}=-\frac{\partial u_i}{\partial x_i}\,, \tag{4.28}$$

where

$$\frac{1}{\rho c_{\text{eff}}^2}=\frac{\gamma}{\rho c^2}-\frac{\beta_T^2 T}{\rho C_p}\,, \tag{4.29}$$

and $T$ is the temperature and $C_p$ is the specific heat for constant pressure. The thermal dilatation coefficient and the viscous dissipation are denoted by $\beta_T$ and $\Phi_\nu$, respectively. The detailed derivations for the pressure evolution equation can be found in Fuster *et al.* (2018). Since the dissipation is generally small compared to other terms, it is ignored in the present study. As a result, it can be approximated that

$$\frac{1}{\rho c_{\text{eff}}^2}\approx\frac{1}{\rho c^2}\,. \tag{4.30}$$

Equation (4.28) can be discretized as

$$\frac{p^{n+1}-p^n}{\Delta t}+u_i^n\frac{\partial p^n}{\partial x_i}=-(\rho c^2)^{n+1}\frac{\partial u_i^{n+1}}{\partial x_i}\,, \tag{4.31}$$

where the velocity at the new time step is computed based on the projection method,

$$u_i^{n+1}=u_i^{***}-\Delta t\left(\frac{1}{\rho}\frac{\partial p}{\partial x_i}\right)^{n+1}\,, \tag{4.32}$$

Substituting Eq. (4.32) into Eq. (4.31), we get the Poisson-Helmholtz equation for pressure,

$$\frac{1}{\rho c^2}\frac{p^{n+1}-p^*}{\Delta t}+\frac{\partial (u_i)^{***}}{\partial x_i}=\Delta t\frac{\partial}{\partial x_i}\left(\frac{1}{\rho}\frac{\partial p}{\partial x_i}\right)^{n+1}\,, \tag{4.33}$$

with $p^*$ is the provisional pressure,

$$p^*=p^n-\Delta t u_i^n\frac{\partial p^n}{\partial x_i}\,, \tag{4.34}$$

and $p^*$ can be computed based on the results after computing the convection, viscous, and surface tension terms, namely $\rho^{***}$, $(\rho u_i)^{***}$, $E^{***}$, using the Mie-Grüneisen EOS

$$p^*=\left(E^{***}-\frac{(\rho u_i u_i)^{***}}{2}\right)(\gamma-1)-\gamma\Pi_\infty\,. \tag{4.35}$$

For a cell with interfaces, $f$ is fractional, then the mixture rule is used

$$E = fE_l + (1-f)E_g\,, \tag{4.36}$$

$$\overline{\frac{1}{\gamma-1}} = \frac{f}{\gamma_l - 1} + \frac{1-f}{\gamma_g - 1}\,, \tag{4.37}$$

$$\overline{\frac{\gamma\Pi_\infty}{\gamma-1}} = \frac{f\Pi_{\infty,l}\gamma_l}{\gamma_l - 1} + \frac{(1-f)\Pi_{\infty,g}\gamma_g}{\gamma_g - 1}. \tag{4.38}$$

Then the provisional pressure at the interface cell is computed as

$$p^* = \frac{E^{***} - \frac{(\rho u_i u_i)^{***}}{2} - \overline{\frac{\gamma\Pi_\infty}{\gamma-1}}}{\overline{\frac{1}{\gamma-1}}}\,. \tag{4.39}$$

In the solution procedure, the provisional pressure ($p^*$) is first computed (Eq. (4.39)), which is then used in the Poisson-Helmholtz equation (Eq. (4.33)) to calculate the pressure $p^{n+1}$. After that, the velocity is corrected by the new pressure using Eq. (4.32). Finally, the total energy is also corrected as

$$E^{n+1} = E^{***} - \Delta t \left(\frac{\partial(pu_i)}{\partial x_i}\right)^{n+1}\,. \tag{4.40}$$

### *4.3.5 Numerical Diffusion Flux*

The advection scheme in the FP method induces numerical oscillations near the shocks and other discontinuities. The reason is that the flux calculation accounts for only one characteristic speed, *i.e.*, the fluid velocity. In regions away from the interface, it can be recognized that the expression in Eq. (4.15) is half-upwind and half-central. As a result, the numerical diffusion induced by the flux calculation is not sufficient to damp the numerical oscillations generated. In order to reduce the numerical oscillations, the KT method (Kurganov and Levy, 2002) is employed. The overall flux in the KT method can be decomposed to central difference part and the numerical diffusion part. Only the second part of the flux is used here, the expression of which in the $x$ direction is given as

$$\vec{H}_{j\pm\frac{1}{2}} = \frac{a^+_{j\pm\frac{1}{2}} a^-_{j\pm\frac{1}{2}}}{a^+_{j\pm\frac{1}{2}} - a^-_{j\pm\frac{1}{2}}}\left[\vec{U}^+_{j\pm\frac{1}{2}} - \vec{U}^-_{j\pm\frac{1}{2}}\right]. \tag{4.41}$$

The discrete equation to incorporate the numerical diffusion flux can be written as

$$\Delta\Omega\frac{\vec{U}'^{n+1} - \vec{U}^{n+1}}{\Delta t} = \Delta_i \vec{H}_i\,, \tag{4.42}$$

with

$$\Delta_i \vec{H}_i = (\vec{H}_{j+\frac{1}{2}} - \vec{H}_{j-\frac{1}{2}})S\,. \tag{4.43}$$

The quantities at the cell surface, *i.e.*, $\vec{U}^+_{j\pm1/2}$ and $\vec{U}^-_{j\pm1/2}$, are reconstructed using the same slope limiter described in Eq. (4.20). The maximum and minimum characteristic speeds are denoted as $a^+_{j+1/2}$ and $a^-_{j+1/2}$, which are calculated as

$$a^+_{j+\frac{1}{2}} = \max\left(\lambda_{max}\left(\frac{\partial \vec{F}_{U,i}}{\partial \vec{U}}(\vec{U}^-_{j+\frac{1}{2}})\right), \lambda_{max}\left(\frac{\partial \vec{F}_{U,i}}{\partial \vec{U}}(\vec{U}^+_{j+\frac{1}{2}})\right), 0\right) \tag{4.44}$$

$$a^-_{j+\frac{1}{2}} = \min\left(\lambda_{min}\left(\frac{\partial \vec{F}_{U,i}}{\partial \vec{U}}(\vec{U}^-_{j+\frac{1}{2}})\right), \lambda_{min}\left(\frac{\partial \vec{F}_{U,i}}{\partial \vec{U}}(\vec{U}^+_{j+\frac{1}{2}})\right), 0\right), \tag{4.45}$$

where $\lambda_{min}$ and $\lambda_{max}$ are the maximum and minimum eigenvalues of the Jacobian matrix $\partial \vec{F}_{U,i}/\partial \vec{U}$.

The algorithm for the present methods to simulate compressible multiphase flows is summarized in Algorithm 1.

## *4.4 Test Cases and Results*

A series of compressible interfacial multiphase flow problems are used to test the numerical methods described above. It is demonstrated that a sharp interface is obtained and the spurious oscillations near the shocks and discontinuities are suppressed efficiently.

### *4.4.1 Sod's Shock-Tube Problem*

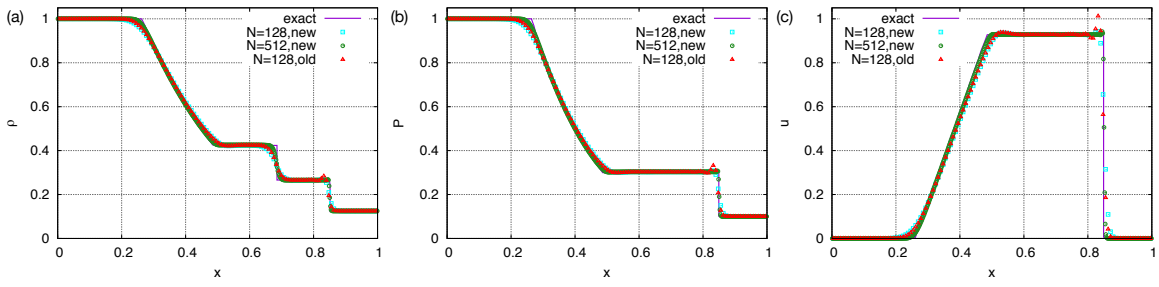


Figure 4.1. 1D shocktube problem using the present method (new) and the FP method (old) with two different mesh resolutions of $N = 128$ and $N = 512$ cells across the simulation domain at $t = 0.2$. The solid line represents the exact solution.

**Algorithm 1** Proposed algorithm to compute compressible multiphase flows.

**while** $t < t_{end}$ **do**
  Set time step $\Delta t$
  Initialize tracers as a list of conservative variables for liquid and gas phases, $\vec{U}_l$ and $\vec{U}_g$
  **for** every direction $x_i$ **do**
    Compute the gradient $\frac{\partial U_j^n}{\partial x_i}$ and reconstruct $\vec{U}_a$ (Eq. (4.18))
    Geometric reconstruction of the interface (PLIC)
    Compute VOF flux, $F_{f,i}$ (Eq. (4.13))
    Compute tracer fluxes,$F_{Ul,i}$ and $F_{Ug,i}$ (Eqs. (4.15) and (4.16))
    Update volume fraction $f^{n+1}$ (Eq. (4.12))
    Update tracers $\vec{U}^*$ (Eq. (4.14))
  **end for**
  Compute conservative variables $\rho^*, (\rho u_i)^*, E^*$ with the updated tracers $\vec{U}_l^*$ and $\vec{U}_g^*$ (Eqs. (4.21)-(4.23))
  **if** $\mu > 0$ **then**
    Solve viscous terms
    Update momentum $(\rho u_i)^{**}$ and energy $E^{**}$ (Eqs. (4.24) and (4.25))
  **end if**
  **if** $\sigma > 0$ **then**
    Compute curvature $\kappa$
    Update momentum $(\rho u_i)^{***}$ and energy $E^{***}$ (Eqs. (4.26) and (4.27))
  **end if**
  Compute $p^*$ using the Mie-Gruneison EOS (Eq. (4.35))
  Solve the Poisson-Helmholtz equation for $p^{n+1}$ (Eq. (4.33))
  Correct velocity and energy with pressure (Eqs. (4.32) and (4.40))
  **for** every direction $x_i$ **do**
    Compute right and left states of the conservative variables
    Compute local characteristic speeds (Eqs. (4.44) and (4.45))
    Compute numerical diffusion fluxes(Eq. (4.41))
    Obtain the final conservative variables $\rho^{n+1}, (\rho u_i)^{n+1}, E^{n+1}$
  **end for**
**end while**

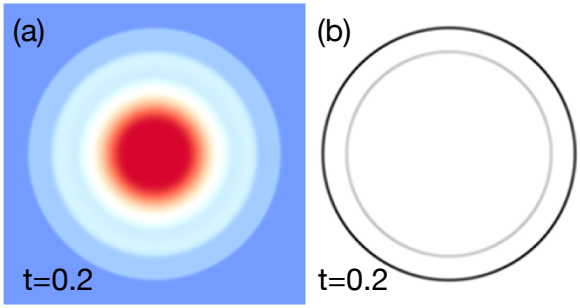


Figure 4.2. Density contour (a) and numerical Schlieren image (b) for the 2D cylindrical shocktube problem using the present method.

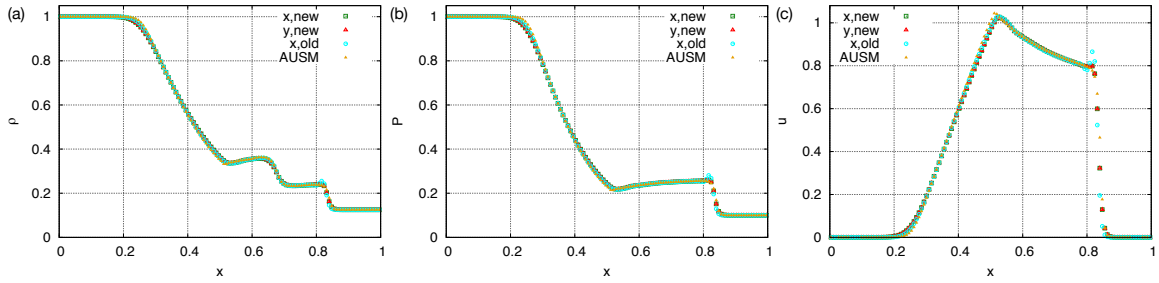


Figure 4.3. 2D shocktube problem using the present method (new) along $x$ and $y$ directions, the FP method (old) along $x$ direction and 1D advection upstream splitting method (AUSM) at $t = 0.2$.

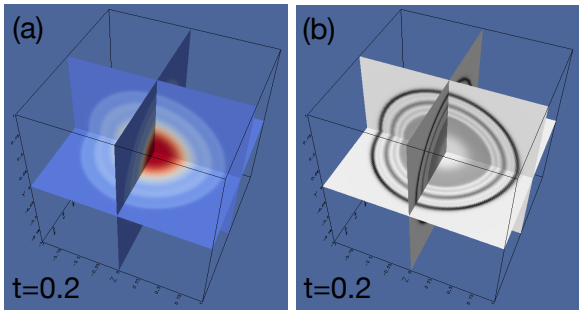


Figure 4.4. Density contour (a) and numerical Schlieren image (b) for the 3D spherical shocktube problem using the present method at $t = 0.2$.

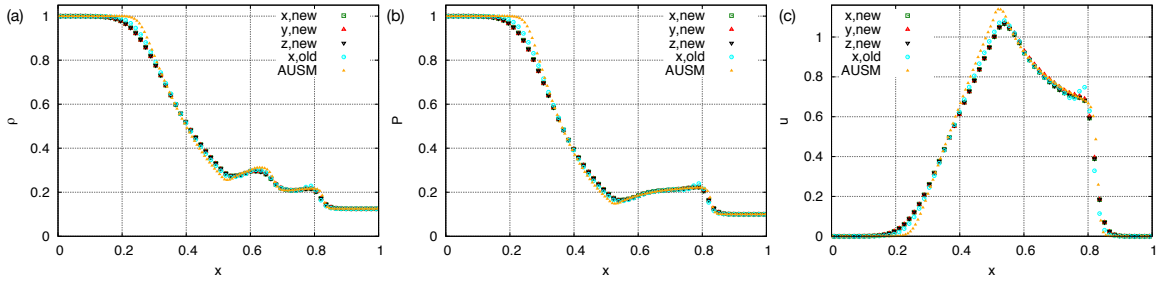


Figure 4.5. 3D shocktube problem using the present method (new) along $x$, $y$ and $z$ directions with $N = 64$, the FP method (old) along $x$ direction and 1D advection upstream splitting method (AUSM) with $N = 128$ at $t = 0.2$.

The 1D shocktube problem of Sod (Sod, 1978) is a classic benchmark case for numerical method validation. The high and low pressure air is initially separated with a diaphragm. The dimensionless fluid properties on the left and right of the diaphragm are given as

$$\{\rho, u, p, \gamma\} = \begin{cases} \{1.0, 0, 1.0, 1.4\} & 0 \leq x \leq 0.5, \\ \{0.125, 0, 0.1, 1.4\} & 0.5 \leq x \leq 1.0. \end{cases} \tag{4.46}$$

At $t = 0$, the diaphragm is removed and the shock wave, the contact surface, and the expansion fan are generated, see Fig. 4.1. The numerical results obtained by the present and the FP methods are in good agreement with the analytic solution for density, pressure and velocity. It is found that the speeds of the shock, the contact and the tail of the expansion fan are well captured. Whereas the spurious oscillations are generated at the locations of shocks for the FP method, the oscillations are effectively suppressed by the present scheme. With refining the grid, more accurate results are obtained.

To demonstrate the numerical methods are implemented properly in multi-dimension, the 2D cylindrical and 3D spherical shocktube problems are simulated. The initial conditions are identical to the 1D case (Eq. (4.46)). Figs. 4.2 and 4.4 show the representative density contours and numerical Schlieren images for the 2D and 3D shocktube problems. Similar to the 1D case, all the waves generated are well captured by the present method. Moreover, the oscillations observed near the shocks for the FP method are not seen in the results for the present method, see Fig. 4.3. The computed results in $x$ and $y$ directions (in $x, y, z$ for 3D) are identical, indicating the multi-dimensional implementation of the numerical methods are done properly. The numerical results are in good agreement with those obtained by a different code solving the one-dimensional axisymmetric and spherical symmetric Euler equations with the advection upstream splitting method (AUSM).

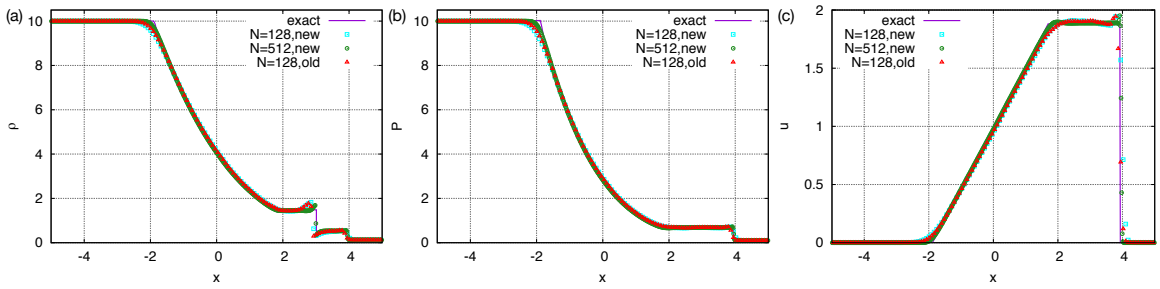


Figure 4.6. 1D shocktube problem for two gases using the present method (new) and the FP method (old) with two different mesh resolutions of $N = 128$ and $N = 512$ cells across the simulation domain at $t = 1.6$. The solid line represents the exact solution.

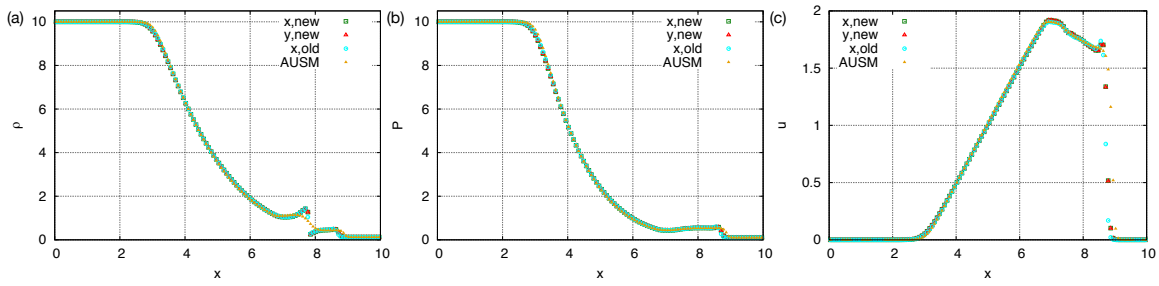


Figure 4.7. 2D shocktube problem for two gases using the present method (new) along $x$ and $y$ directions and the FP method (old) along $x$ direction and 1D advection upstream splitting method (AUSM) at $t = 1.6$.

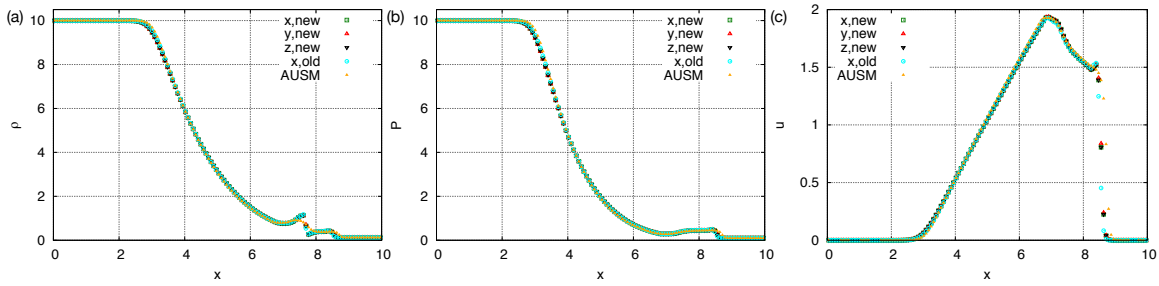


Figure 4.8. 3D shocktube problem for two gases using the present method (new) along $x$, $y$ and $z$ directions, the FP method (old) along $x$ direction and 1D advection upstream splitting method (AUSM) at $t = 1.6$.

### *4.4.2 Shock tube Problem with Two Different Gases*

The single-fluid shocktube problem of Sod is extended to that with two different gases. The two gases exhibit different $\gamma$ and both obey the ideal gas law ($\Pi_\infty = 0$). The volume fraction $f$ is used to distinguish the two gases, $f = 1$ and 0 for the gases initially on the left and right of the diaphragm, respectively. The initial conditions and fluid properties are given as

$$\{\rho, u, p, \gamma, f\} = \begin{cases} \{10, 0, 10, 1.4, 1\} & -5 \leq x \leq 0, \\ \{0.125, 0, 0.1, 1.2, 0\} & 0 \leq x \leq 5. \end{cases} \tag{4.47}$$

Fig. 4.6 shows that the interface separating the two gases is captured as a sharp surface (the thickness is the cell size). The spurious oscillations near the shocks are again, reduced by the present method. Small oscillations near the shocks are observed for both methods in the velocity plots. The numerical results for the present method are again in good agreement with the exact solution.

Similarly, 2D and 3D shocktube problems with two different gases are tested as well with identical initial conditions and fluid properties. As is seen in Fig. 4.7, the profiles of the density, pressure and velocity for the present method along $x$ and $y$ directions agree well with each other. Moreover, good agreement is achieved for the results using the present method and the 1D AUSM code. An interface is captured as a perfect discontinuity by the present method while the thickness of the interface in the AUSM results is diffused to multiple cells. Similar observations can be made for the 3D case. See Fig. 4.8.

### *4.4.3 Shock Tube Problem for Two Different Phases*

The shocktube problem is also extended to two phases to test the implementation of the equation of state. While the gas phase (air) obeys the ideal gas law, the liquid phase, water, follows the Mie-Grüneisen equation of state. This test has also been used in previous studies (Johnsen and Colonius, 2006) and was used to model

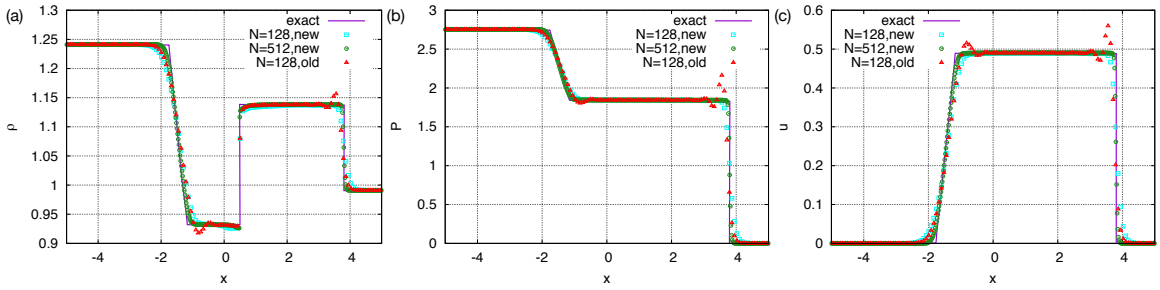


Figure 4.9. 1D gas-liquid shocktube problem using the present method (new) and the FP method (old) with two different mesh resolutions of $N = 128$ and $N = 512$ cells across the simulation domain at $t = 1.0$. The solid line represents the exact solution.

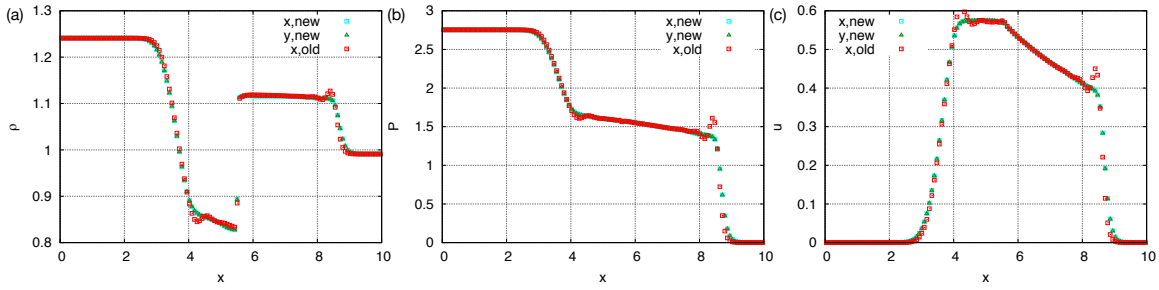


Figure 4.10. 2D gas-liquid shocktube problem using the present method (new) along $x$ and $y$ directions and the FP method (old) along $x$ direction at $t = 1.0$.

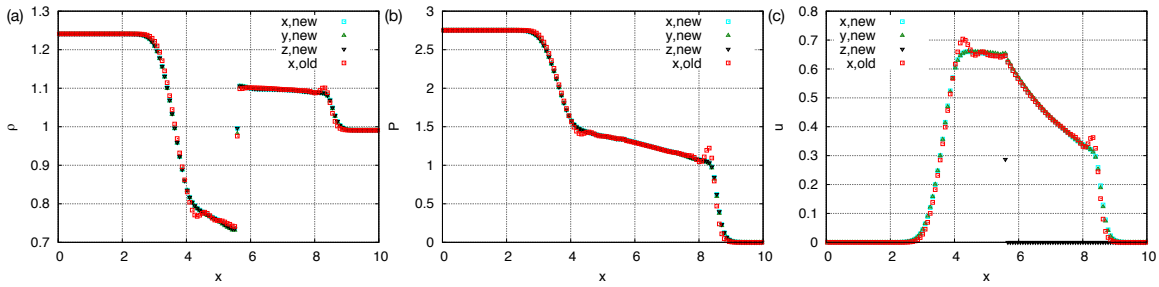


Figure 4.11. 3D gas-liquid shocktube problem using the present method (new) along $x$, $y$ and $z$ directions and the FP method (old) along $x$ direction at $t = 1.0$.

the underwater explosions. The initial conditions and fluid properties are given as

$$\{\rho, u, p, \gamma, \Pi_\infty, f\} = \begin{cases} \{1.241, 0, 2.753, 1.4, 0, 0\} & -5 \leq x \leq 0, \\ \{0.991, 0, 3.059 \times 10^{-4}, 5.5, 1.505, 1\} & 0 \leq x \leq 5. \end{cases} \tag{4.48}$$

Fig. 4.9 shows that both the shock, the interface, and the expansion fan are excellently captured by the present method, whereas the oscillations near the shock and the tail of the expansion fan are observed for the FP method. The results for the present method agree very well with the analytic solution. The numerical results converge toward the exact solution when the mesh is refined.

2D cylindrical and 3D spherical tests for the gas-liquid shocktube problem are also performed with identical initial conditions and fluid properties. Again, the shock and expansion fan are well captured by the present method, see Figs. 4.10 and 4.11. Oscillations near shocks and expansion fans appearing for the FP method are eliminated by the present method. The sharp interfaces are well resolved as in the 1D case.

### *4.4.4 Shock Interaction with a 2D Bubble*

The interaction between a planar shock wave and a cylindrical helium bubble is a classic test case to examine the capability of the numerical methods in capturing the interaction between shock and curved surface. The previous studies on this problem using experiment (Haas and Sturtevant, 1987) and simulation (Quirk and Karni, 1996; Terashima and Tryggvason, 2009; Aslani and Regele, 2018) can be used for comparison

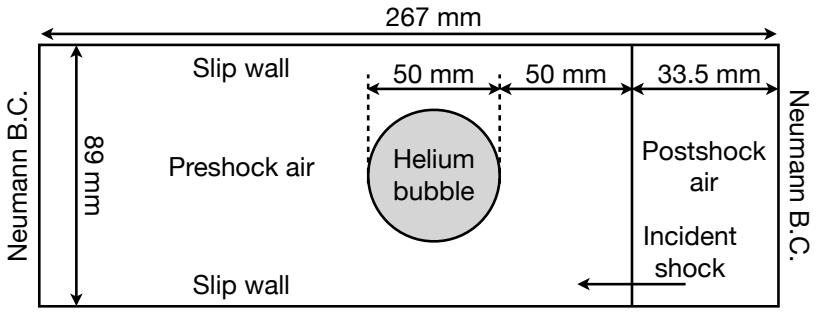


Figure 4.12. Schematic of the computational domain of the shock interaction with a 2D bubble.

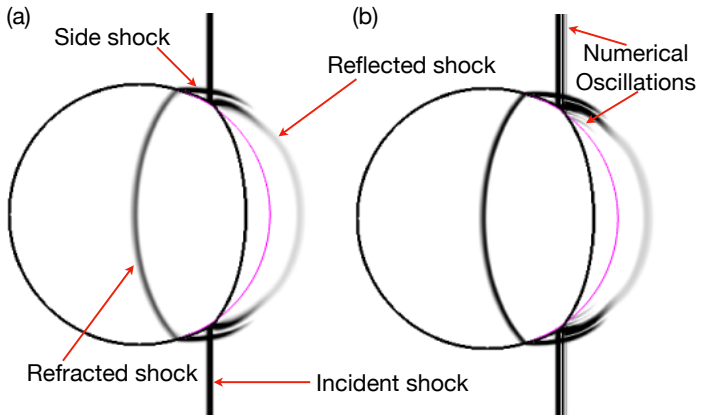


Figure 4.13. Numerical Schlieren images showing the wave structures during the shock-bubble interaction by (a) the present method and (b) the FP method at $t = 32$ $\mu$s. The pink circles represent the initial interface of the bubble.

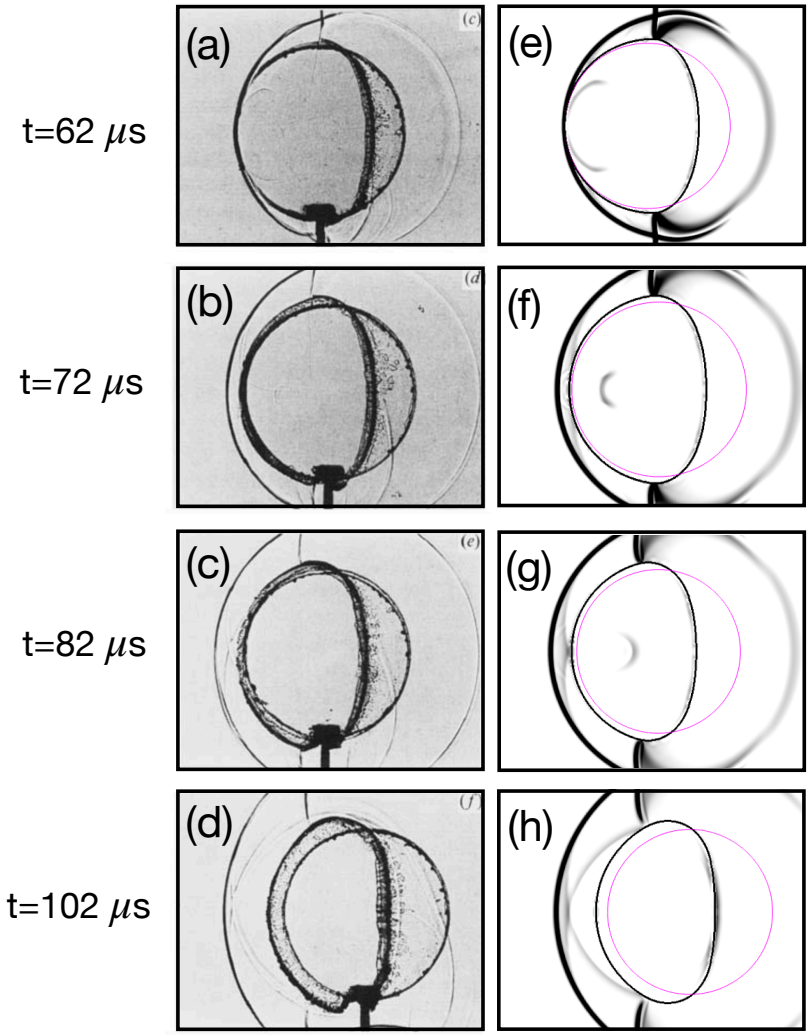


Figure 4.14. Comparison between experimental shadowgraphs (Haas and Sturtevant, 1987) (a-d) and numerical Schlieren images (e-h) using the present method.

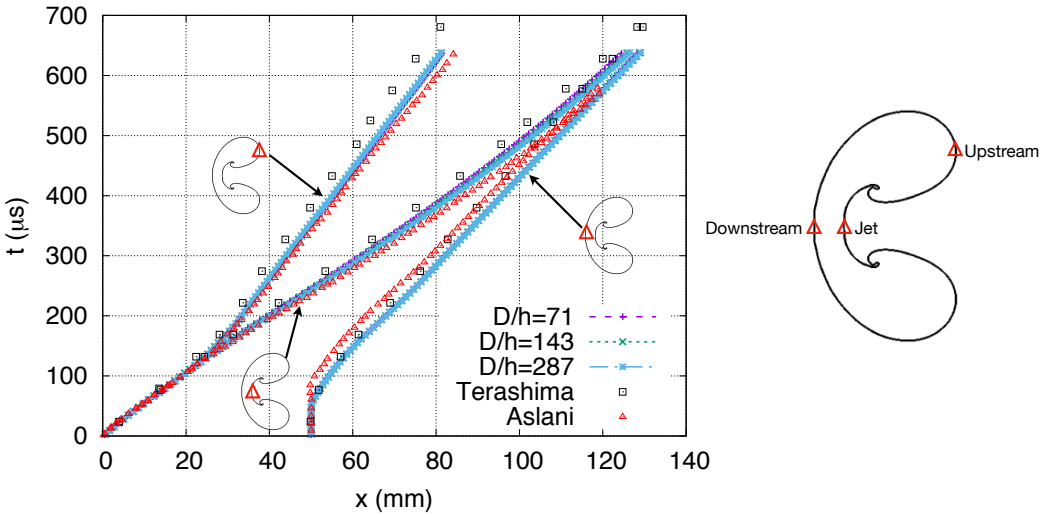


Figure 4.15. Comparisons of the temporal evolutions of the three characteristic points on the bubble i.e. the jet, upstream and downstream locations from the present simulation by varying the number of cells across the bubble diameter from 71 to 287 points with the numerical work (symbols) of Quirk and Karni (Quirk and Karni, 1996).

Table 4.1. Initial conditions for shock interaction with a 2D helium bubble.

| | $\rho$ (kg/m$^3$) | $u$ (m/s) | p (Pa) | $\gamma$ |
|---|---|---|---|---|
| Preshock air | 1.176 | 0 | 101325 | 1.4 |
| Postshock air | 1.618 | −115.81 | 159094 | 1.648 |
| Helium bubble | 0.219 | 0 | 101325 | 1.648 |

with the present results. In the experiment of Haas and Sturtevant (1987), the Mach number of the incident shock is 1.22 and the diameter of the cylindrical helium bubble is 50 mm and the channel height is 89 mm. In the present simulation, the height of the computational domain is the same as that in the experiment and the domain length is three times of the domain height, which is sufficiently long for the time of interest here.

To be consistent with former studies, inviscid simulation is performed with viscosity and surface tension ignored. The left and right boundaries are prescribed as Neumann boundary conditions for all conservative variables with the top and bottom boundaries set as slip walls. Grid refinement studies were carried out with the bubble diameter being initially resolved with 71, 143 and 287 grid points. The initial conditions are given in SI units in Table 4.1. The computational domain and

boundary conditions are presented in Fig. 4.12. The bubble is initially stationary and located at the center of the domain. The incident shock moves from the right to the left and is initially one diameter away from the bubble center.

The results obtained by the present and the FP methods are compared in Fig. 4.13, which demonstrates that the present scheme is capable of capturing the complex wave structures induced by shock-bubble interaction. Since the shock speed in helium is larger than air, the transmitted shock is diverging. Furthermore, as the shock impedance of helium is slightly larger than that of air, the reflected wave generated is a weak shock wave. The oscillations are observed in the results for the FP method as indicated in Fig. 4.13 (b). These numerical oscillations are successfully eliminated by the present method.

The numerical results are compared with the experimental shadowgraphs at different times in Fig. 4.14 . The wave structures captured in simulation, including the incident shock, the reflected shock, the refracted shock, and the intersection point among the three shocks, agree well with the experimental results. As time elapses, the bubble deforms and moves downstream. The agreement between the simulation and experimental results for the bubble surface is excellent.

Fig. 4.15 shows the temporal evolutions of three characteristic length on the bubble, i.e. the air-jet penetration length into the bubble, the upstream and downstream locations, for the present method with different mesh resolution, compared with the results by Terashima and Tryggvason (Terashima and Tryggvason, 2009) and Aslani and Regele (Aslani and Regele, 2018). It is shown that the convergent results for the present method are achieved. The present results generally agree well with those by Terashima and Tryggvason (Terashima and Tryggvason, 2009) and Aslani and Regele (Aslani and Regele, 2018). The trajectories of the upstream location and the air-jet penetration length of the present simulation results lie between the corresponding results in Refs. (Terashima and Tryggvason, 2009) and (Aslani and Regele, 2018), while the trajectory of the downstream location shifts downstream.

Table 4.2. Initial conditions for shock interaction with a 2D water drop.

| | $\rho$ (kg/m$^3$) | $u$ (m/s) | p (Pa) | $\gamma$ | $\Pi_\infty(Pa)$ |
|---|---|---|---|---|---|
| Preshock air | 1.203 | 0 | 101178 | 1.4 | 0 |
| Postshock air | 2.176 | $-225.79$ | 238293 | 1.4 | 0 |
| Water droplet | 988.367 | 0 | 101178 | 5.5 | $3.43 \times 10^8$ |

The discrepancy arises from effect of domain size on the simulation results, where the reflected waves can influence the bubble dynamics. A shorter channel height and length compared to that of Ref. (Aslani and Regele, 2018) and a shorter channel length compared to that of Ref. (Terashima and Tryggvason, 2009) are adopted in the present simulation.

### *4.4.5 Shock Interaction with a 2D Water Drop*

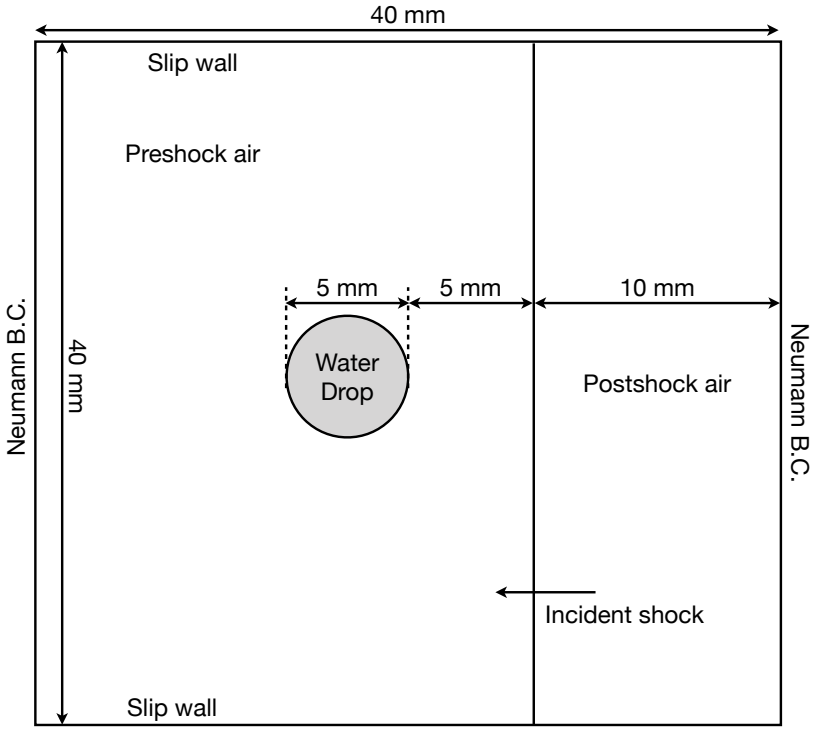


Figure 4.16. Schematic of the computational domain of the shock interaction with a 2D water drop.

The interaction between the shock wave in air with a 2D water drop is simulated to test the capability of the present method in capturing the interaction between a shock wave and an interface separating two phases with significantly different fluid

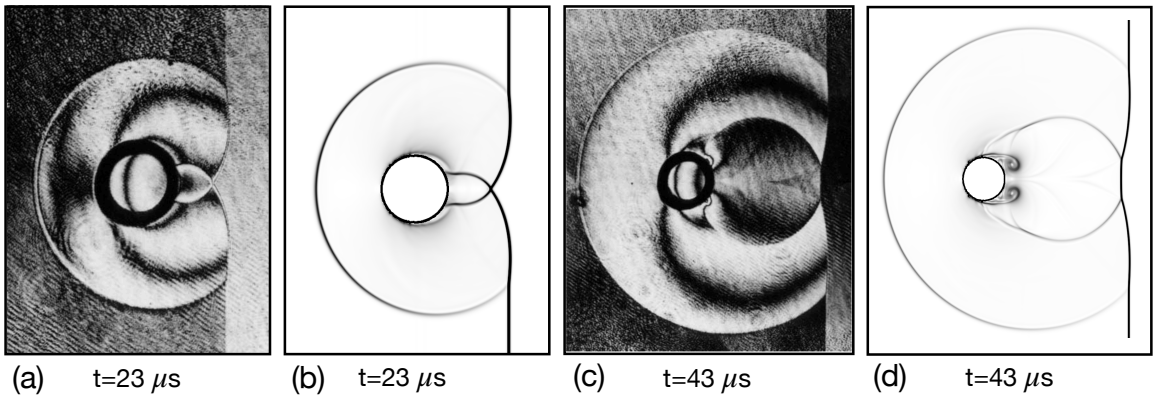


Figure 4.17. Comparisons of the experimental (a,c) and numerical (b,d) Schlieren images from the holographic interferograms of Igra and Takayama (Igra and Takayama, 2001) and the present simulation, respectively.

Table 4.3. Initial conditions for shock interaction with a 3D water drop.

| | $\rho$ (kg/m$^3$) | $u$ (m/s) | p (Pa) | $\gamma$ | $\Pi_\infty(Pa)$ |
|---|---|---|---|---|---|
| Preshock air | 1.203 | 0 | 101178 | 1.4 | 0 |
| Postshock air | 2.176 | $-225.79$ | 238293 | 1.4 | 0 |
| Water droplet | 1000 | 0 | 101178 | 6.12 | $4.921 \times 10^8$ |

properties. The initial conditions and fluid properties in SI units are given in Table 4.2. The computational domain and boundary conditions are presented in Fig. 4.16. Since the time simulated is significantly smaller than the capillary and viscous time scales, the viscous and capillary effects are negligible. There exist previous numerical studies (Igra and Takayama, 2001; Aslani and Regele, 2018; Meng and Colonius, 2015) on this test case.

As shown in Fig. 4.17, the reflected shock and transmitted shock are well captured by the present method, which agrees very well with the experimental images obtained by Igra and Takayama (Igra and Takayama, 2001). The wake vortical structures behind the water cylinder are shown in Fig. 4.18. As time evolves, due to the interaction with the shock, the instabilities developed on the drop surface, resulting in significant deformation and breakup of the drop. The ligaments are formed at the periphery of the water cylinder and disintegrate to small drops.

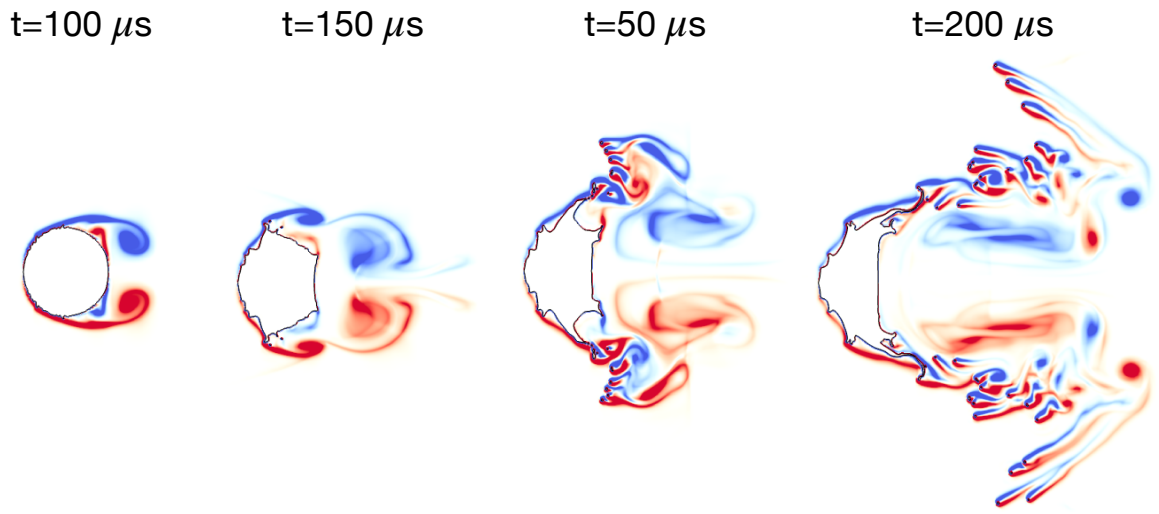


Figure 4.18. Temporal evolutions of the vorticities in the vicinity of the drop.

### *4.4.6 Shock Interaction with a 3D Water Drop*

Finally, the 3D shock-drop interaction is simulated by the present method. Similar to the 2D case, the capillary and viscous effects are negligible in the short term. The initial conditions and fluid properties are given in Table 4.3. The computational domain and boundary conditions are similar to that for a 2D water cylinder, see Fig. 4.16. The incident shock moves from right to left in the simulation domain. The drop diameter is $D_0$ and the domain size is $8D_0$. A uniform mesh ($256 \times 256 \times 256$) is used. The mesh resolution is equivalent to 32 cells across the initial drop diameter ($D_0/\Delta x = 32$). Following former studies (Meng and Colonius, 2018), the time, the center-of-mass (COM) drift of the drop, the drop's COM streamvise velocity and acceleration are nondimensionalized as $t^* = t\frac{u_{ps}}{D_0}\sqrt{\frac{\rho_{ps}}{\rho_l}}$, $\Delta x^* = \Delta x/D_0$, $u^* = u/u_{ps}$ and $a^* = aD_0/u_{ps}^2$, where $\rho_{ps}$ and $u_{ps}$ are the postshock gas density and velocity, respectively.

The temporal evolution of the drop shape is shown in Fig. 4.19. The present results generally agree well with the experimental results of Theofanous *et al.* (Theofanous *et al.*, 2012) and the simulation results of Meng and Colonius (Meng and Colonius, 2018). The discrepancy compared to the results of Meng and Colonius (Meng and Colonius, 2018) is mainly due to the relatively low mesh resolution used

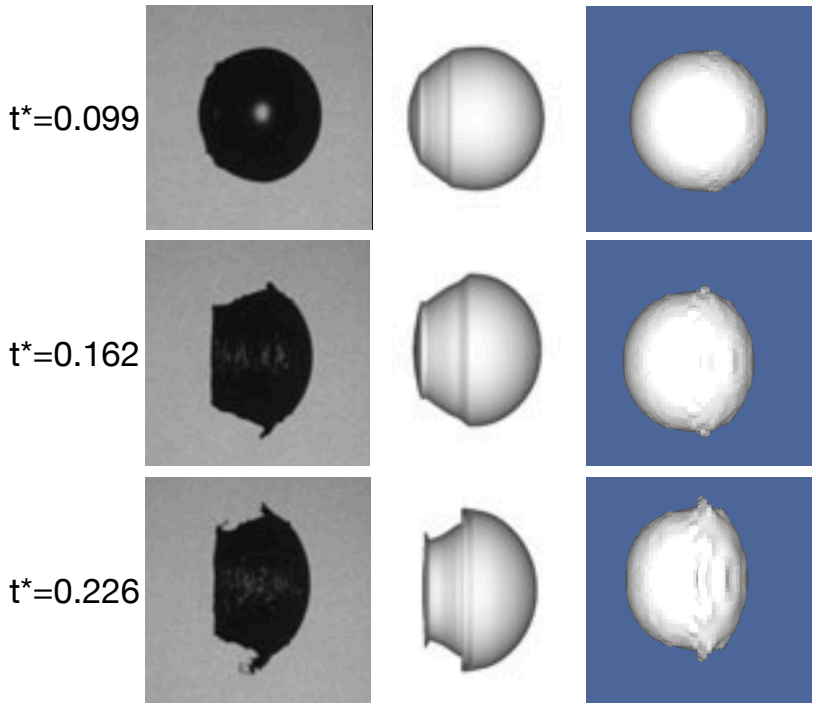


Figure 4.19. Comparisons of the temporal evolution of the aerobreakup of a water drop for the present method (right column) with Theofanous *et al.*'s experimental (Theofanous *et al.*, 2012) (left column) and Meng and Colunius' numerical (Meng and Colonius, 2018) (middle column) results.

in the present simulation. Nonetheless the overall deformation of the drop during the interaction with shock wave is reasonably captured. The downstream side of the drop is flattened as the shock passes through the drop and a liquid sheet is formed near the drop equator due to the stronger shear flow caused by the shock. The drop gradually deform to a muffin-like shape. In experiment, it is observed that the shear instabilities develop into thin liquid sheets and the liquid sheet starts disintegrating into liquid mist. Yet a very high mesh resolution is required to capture the interfacial instabilities, which is out of the scope of the present study.

Figure 4.20 shows the streamwise COM drift, velocity and acceleration of the drop obtained by the present simulation. The present results agree well with the simulation results by Meng and Colonius (Meng and Colonius, 2018) until about $t^* = 0.2$. The deviation developed after $t^* \sim 0.2$ are due to the small domain and simple boundary conditions used here. The shocks reflected from the domain

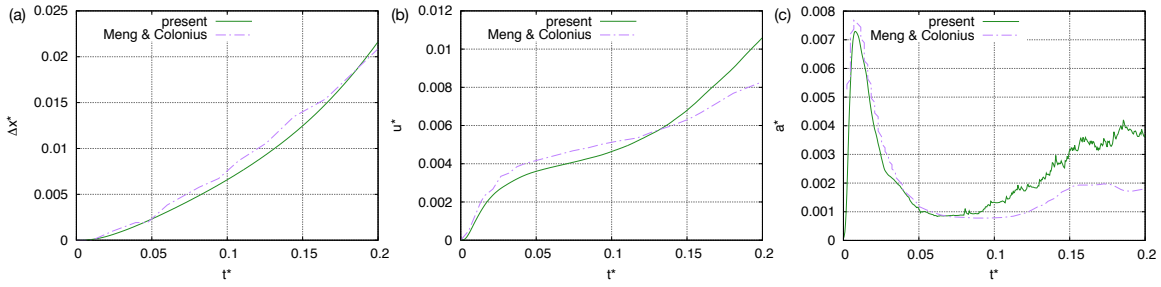


Figure 4.20. Comparisons of the drop streamwise COM drift (a), velocity (b) and acceleration (c) between the present simulation and that of Meng and Colunius (Meng and Colonius, 2018).

boundaries will influence the dynamics of the drop. Nevertheless, the good agreement at early term is sufficient to validate the present method. In particular, the short-term peak of the acceleration that is induced by the passage of the shock through the drop agrees very well with the high-resolution simulation results of Meng and Colonius (Meng and Colonius, 2018).

## *4.5 Conclusions*

A novel numerical method has been developed to simulate liquid atomization in a compressible multiphase flow, in which the one-fluid approach is adopted and the geometrical volume-of-fluid (VOF) method is used to capture the interface. The compressible Navier-Stokes equations with surface tension is solved along with the Mie-Grüneisen equations of state (EOS). The spatial discretization is based on the finite volume approach. Since the conservative variables are advected as tracers associated with the volume fraction function, the calculation of the fluxes for the conservative variables are consistent with that for the VOF flux. Since the VOF flux calculation accounts for only one characteristic speed i.e. the fluid speed, the FP method is half-upwind and half-central in regions away from the interface. The numerical diffusion, therefore, induced by the flux calculation itself, is not sufficient to suppress the numerical oscillations generated by the discontinuities in the flow field. Therefore, additional numerical diffusion is introduced based on the Kurganov-Tadmor method and is only applied in the region away from the interface. The viscous and capil-

lary effects are also included. The balanced-force continuum force formulation and height-function curvature model are utilized to calculate the surface tension force.

The as-developed numerical method is validated against a number of compressible multiphase flow problems. The classic 1D Sod's shock tube problem is simulated. The speed of the shock, the contact and the tail of expansion fan all agree well with the analytic solution. The spurious oscillations observed in the original FP method are effectively suppressed by the present method. The 2D cylindrical and 3D spherical shock tube problems are also tested. The present results agree well with a separate code that uses the advection upstream splitting method (AUSM), demonstrating that the present method is implemented properly in multi-dimension. The single-fluid shock tube problem of Sod is extended to those involving two different gases and two different phases in 1D, 2D and 3D. The Mie-Grüneisen equation of state (EOS) is used for the liquid phase and the simulation results are found to agree well with analytical solution for 1D or the AUSM simulation results for 2D and 3D. The sharp interfaces separating different fluids or phases are captured as a discontinuity (the interface thickness is the cell size). The interaction between a planar shock with a 2D helium bubble, a 2D water drop, and a 3D water drop are simulated to verify the capability of the present method in capturing the shock interaction with 2D and 3D curved interfaces. The complex wave structures induced by the shock-bubble and shock-droplet interactions, including the reflected shock, side shock, refracted shock and transmitted shock are accurately captured, and the numerical results agree very well with the experimental shadowgraphs. Quantitative validations are made by comparing numerical results for the temporal evolutions of three characteristic lengths on the bubble and the droplet centroid with the experimental data and good agreement is achieved for all cases tested.

# CHAPTER FIVE

## Conclusions and Outlook

The overarching goal of this dissertation is to investigate liquid atomization in both quiescent environment and high-speed gas flows. The high-fidelity simulation approach is adopted, where the Naiver-Stokes equations are directly solved without any explicit physical models. The geometric volume-of-fluid method has been used to capture the interface. The height-function method was used to calculate the curvature and the balanced force approach was employed for surface tension calculation. Fine mesh resolutions have been used in all simulations (except the 3D test case in Chapter 4) to guarantee the high-fidelity interfacial multiphase flow details are faithfully captured.

The dissertation starts with a canonical 2D axisymmetric simulation of droplet formation in the dripping regime (Chapter two). Then the study has been extended toward a 3D simulation of the atomization of gasoline surrogate jet with practical engine operation conditions (Chapter three). Finally, novel numerical methods have been developed to simulate liquid atomization in supersonic flows (Chapter four). The key findings in these three chapters are summarized as follows.

In Chapter two, numerical simulations have been performed to study the short-term transient falling dynamics of a dripping water drop with a low inflow rate in the dripping regime. The focus is on the short-term behavior with a time range covering about eight dominant second-mode oscillations of the drop. The simulation results are validated against experiments under the same conditions. A nonlinear oscillation is triggered by the post-formation state of the drop. The overall process of the drop growth, breakup and fall is studied so as to rigorously account for the effect of drop formation on oscillation. Complex oscillation dynamics and transient flow surrounding the drop is induced by the interaction between the oscillation and

falling motion of the drop. As for the drop formation, it is shown that the relation between drop height and volume is in good agreement with that of the pendant drop theory, which demonstrates that the quasi-static drop growth can be fully depicted by the static theory. The simulation and experimental results for the drop contours at different times match perfectly. The shifting of the minimum radius of the two ends of the liquid bridge and the interface overturning before pinch-off are rigorously captured in the simulation. The initial inertial regime and its transition to the viscous regime can be clearly identified in the temporal evolution of the liquid bridge minimum radius. The initial amplitudes of the spherical harmonic modes of the initial drop shape are found to be finite. The pinching dynamics of the drop influences the higher-order modes (modes number larger than two). It is found that the initial kinetic energy plays a role to amplify the initial oscillation amplitude and induce a phase shift of all the oscillation modes. A linear model for a free drop oscillation is found to yield good predictions for the second and third modes. Nonlinear effects such as asymmetry in oscillation amplitude and interaction between distinct modes are identified and higher-order modes ($n \geq 4$) exhibit stronger nonlinear effects. In the frequency spectra of the Fourier-Legendre coefficients for different modes, it is observed that the primary frequency for a given mode agrees with the Lamb frequency, and secondary frequencies corresponding to different modes also arise. The mode coupling effect is strongest for the fourth mode since there exists a commensurate relation between the second and fourth modes. The effect of the fall on the oscillation frequency is little for the time range considered. The strengthened upward shift in oscillation amplitude for the high-order even modes is induced by the increased shear stress due to the falling motion. The damping of oscillation amplitude is slowed down as the drop falling motion feeds energy to oscillations. Complicated transient flows around the drop are induced due to the interaction between the drop nonlinear shape oscillation and the external flow. A saddle point is generated inside the drop and two counterrotating vortices are observed. Though the potential flow directions

vary following the dominant second-mode oscillation, the rotating directions of the vortices remain the same. The wake vortices are influenced by the drop oscillation. The vortices inside the drop are stretched and split. A tracer function is used in the simulation to investigate scalar transport within the drop due to shape oscillations. It is revealed that stretching and folding of the tracer field are related to the vortex motion inside the drop which is in turn induced by the interaction between the drop falling motion and shape oscillations.

In Chapter three, the injection and atomization of a gasoline surrogate jet are investigated through high-fidelity modeling and simulation. The injection conditions are similar to the Engine Combustion Network (ECN) Spray G operating conditions. A nonzero injection angle is specified at the inlet to model the effect of the internal flow in the injector on the jet dynamics and a parametric study by varying the injection angle is carried out. The injection angle that best represents the Spray G conditions is identified by comparing the simulation results for different injection angles with the experimental measurements for the jet penetration length and jet deflection angle. The momentum-conserving VOF method was used for the simulation. The present simulation method is shown to be effective in resolving both the macro-scale and micro-scale breakup features. The shear-induced interfacial waves on the jet column and the formation of liquid lobes and fingers are asymmetric due to the azimuthally varying velocity within the liquid jet, which is in turn induced by the nonzero injection angle. Furthermore, the longitudinal wavelengths along the jet top are significantly smaller than those on the lateral sides. Likewise, the nonuniform velocity influences the deformation and breakup of the jet head. The jet head tilts in the streamwise direction and the upper part of the jet breaks earlier and mores violently compared to the lower part, which is ascribed to the higher velocity in the upper part of the jet. As a consequence of the asymmetric breakup dynamics, two different scaling laws for the total droplet number at the early and later times arise. The short- and long-terms scaling laws correspond to the smaller droplets created from the violent breakup of

the upper part of the jet head at early time, and the mild breakup of the lower part of the jet head at later time, respectively. The droplet number distribution over the volume-based droplet diameter is derived as a function of time and azimuthal angle. The probability density functions (PDF) for different azimuthal angle collapse to a self-similar profile, which is fitted with both the lognormal and gamma distribution functions. Even though a fine mesh was used in the simulation, there are still droplets that are under resolved. Nevertheless, the size-distributions of resolved droplets for the refinement level 11 and 12 match well with each other and both agree well with the lognormal function. This observation indicates that the size distribution of resolved droplets are not influenced by the under-resolved tiny droplets and the mesh resolution is fine enough to capture the micro-scale breakup features such as the interfacial waves and the jet head deformation. The mass of the under-resolved droplets in simulation with mesh refinement level 12 is estimated to be about 3.1% of the total mass of all the droplets generated. A hyperbolic tangent function can well represent the PDF of the azimuthal angle. It is shown that both the PDFs of diameter and azimuthal angle vary little over time at later time. A theoretical model is proposed to predict the droplet number for an arbitrary droplet diameter and azimuthal angle at later time of the primary breakup in terms of the self-similar PDF, which agrees well with the simulation results.

In Chapter four, a novel numerical method is developed to simulate liquid atomization in a supersonic flow. The one-fluid approach is adopted and the sharp interface is captured by the geometrical volume-of-fluid (VOF) method. The compressible Navier-Stokes equations with surface tension are solved along with the Mie-Grüneisen equations of state (EOS). The spatial discretization is based on the finite volume approach. The conservative variables, including density, momentum, and energy, are advected as tracers associated with the volume fraction function of corresponding phase. As a result, the calculation of the fluxes for the convective variables are consistent with that for the VOF flux. Since the VOF flux calculation accounts

for only one characteristic speed i.e. the fluid speed, the FP method is half-upwind and half-central in regions away from the interface. The numerical diffusion, therefore, induced by the flux calculation itself, is not sufficient to suppress the numerical oscillations generated by the discontinuities in the flow field. Therefore, additional numerical diffusion is introduced based on the Kurganov-Tadmor method. This additional numerical diffusion is only applied in the region away from the interface. The viscous and capillary effects are also included. The balanced-force continuum force formulation and height-function curvature model are utilized to calculate the surface tension force. A number of compressible multiphase flow problems have been used to test the as-developed numerical method. The classic 1D Sod's shock tube problem is simulated. The speed of the shock, the contact and the tail of expansion fan all agree well with the analytic solution. The spurious oscillations observed in the original FP method are effectively suppressed by the present method. The 2D cylindrical and 3D spherical shock tube problems are also tested. The present results agree well with a separate code that uses the advection upstream splitting method (AUSM), demonstrating that the present method is implemented properly in multi-dimension. The single-fluid shock tube problem of Sod is extended to those involving two different gases and two different phases in 1D, 2D and 3D. The Mie-Grüneisen equation of state (EOS) is used for the liquid phase and the simulation results are found to agree well with analytical solution for 1D or the AUSM simulation results for 2D and 3D. The sharp interfaces separating different fluids or phases are captured as a discontinuity (the interface thickness is the cell size). The interaction between a planar shock with a 2D helium bubble, a 2D water drop, and a 3D water drop are simulated to verify the capability of the present method in capturing the shock interaction with 2D and 3D curved interface. The complex wave structures induced by the shock-bubble and shock-droplet interactions, including the reflected shock, side shock, refracted shock and transmitted shock are accurately captured, and the numerical results agree very well with the experimental shadowgraphs. Quantitative validations are made by com-

paring numerical results for the temporal evolutions of three characteristic lengths on the bubble and the droplet centroid with the experimental data and good agreement is achieved for all cases tested.

There are several opportunities to extend the research works reported in this dissertation in the future. First, there have been some preliminary data on the chaotic transport of the tracer particles inside a falling drop with oscillation, which plays a key role in the mixing of materials in the industrial and medical applications. A more detailed parametric study can be done in the future to investigate the chaotic mixing in oscillating drops.

Secondly, a parametric study is of interest to systematically study the impact of the drop formation on the dynamics of the falling drop for different Weber and Ohnesorge numbers.

Third, further investigation on the azimuthal variance of the longitudinal interfacial wavelength for the injection of a liquid jet with nonzero injection angle can be taken in the future. Due to the existence of the localized variation of the wavelength, a wavelet transform of the spatial evolution of the wave amplitude can be performed to study the interfacial instability development for liquid jet with non-zero injection angles.

Last but not the least, the numerical methods developed in this dissertation can be used to simulate the atomization of a liquid jet issuing normally into a supersonic gaseous crossflow and to provide the crucial insights required to improve fuel injection in supersonic propulsion systems.

# APPENDICES

# APPENDIX A

## Pendant Drop Theory

The shape of a static pendant drop can be calculated based on the equilibrium equation (Padday and Pitt, 1973)

$$\sigma\left(\frac{1}{\mathcal{R}_1}+\frac{1}{\mathcal{R}_2}\right)=2\sigma\kappa_b-(\rho_l-\rho_g)gz'\,, \tag{A.1}$$

where $\rho_l$ and $\rho_g$ are the water and air densities respectively and $\kappa_b$ is the curvature at the bottom of the pendant drop. The two principal radii of curvature, $\mathcal{R}_1$ and $\mathcal{R}_2$, can be calculated as

$$\frac{1}{\mathcal{R}_1}=\frac{\partial\phi}{\partial s}\,,\frac{1}{\mathcal{R}_2}=\frac{\sin\phi}{x'}, \tag{A.2}$$

where $s$ is the curvilinear coordinate starting from the bottom of the drop, see figure 2.4. Then Eq. (A.1) can be written as

$$\frac{\partial\phi}{\partial s}=2\kappa_b-\frac{(\rho_l-\rho_g)gz'}{\sigma}-\frac{\sin\phi}{x'}. \tag{A.3}$$

It can also be shown from geometry that

$$\frac{\partial x'}{\partial s}=\cos\phi\,, \tag{A.4}$$

$$\frac{\partial z'}{\partial s}=\sin\phi\,. \tag{A.5}$$

At the end the ODE system, Eqs. (A.3), (A.4), and (A.5), can be solved numerically to yield the contour of the static pendant drop.

# APPENDIX B

## Grid Independence Study for the Evolution of the Amplitude of Spherical Harmonic Modes

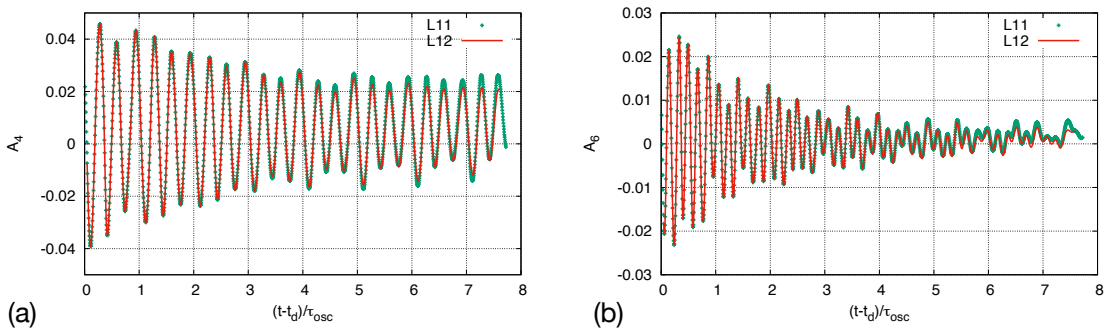


Figure B.1. Temporal evolutions of the Fourier-Legendre coefficients for the (a) $n = 4$ and (b) $n = 6$ modes for different mesh resolutions.

To fully confirm the results of Fourier-Legendre coefficients shown in Fig. 2.11 are grid independent, a simulation with an additional refinement level $L = 12$ has been performed. The results for the $n = 4$ and 6 modes are shown in Fig. B.1, confirming that the important conclusions made related to the effect of drop formation, nonlinear dynamics, and falling motion on the drop oscillation are independent of the grid resolution.

# BIBLIOGRAPHY


Agarwal, A. and M. F. Trujillo (2020). The effect of nozzle internal flow on spray atomization. *Int. J. Engine Res. 21*, 55–72.

Agbaglah, G., R. Chiodi, and O. Desjardins (2017). Numerical simulation of the initial destabilization of an air-blasted liquid layer. *J. Fluid Mech. 812*, 1024–1038.

Agrawal, M., A. R. Premlata, M. K. Tripathi, B. Karri, and K. C. Sahu (2017). Nonspherical liquid droplet falling in air. *Phys. Rev. E 95*, 033111.

Aguerre, H. J. and N. M. Nigro (2019). Implementation and validation of a lagrangian spray model using experimental data of the ECN Spray G injector. *Comput. Fluids 190*, 30–48.

Aleiferis, P. G., J. Serras-Pereira, Z. Van Romunde, J. Caine, and M. Wirth (2010). Mechanisms of spray formation and combustion from a multi-hole injector with E85 and gasoline. *Combust. Flame 157*, 735–756.

Ambravaneswaran, B., E. D. Wilkes, and O. A. Basaran (2002). Drop formation from a capillary tube: Comparison of one-dimensional and two-dimensional analyses and occurrence of satellite drops. *Phys. Fluids 14*, 2606–2621.

Andreopoulos, J. and W. Rodi (1984). Experimental investigation of jets in a cross-flow. *J. Fluid Mech. 138*, 93127.

Angilella, J. R. and J. P. Brancher (2003). Note on chaotic advection in an oscillating drop. *Phys. Fluids 15*, 261–264.

Aniszewski, W. (2016). Improvements, testing and development of the ADM-$\tau$ subgrid surface tension model for two-phase LES. *J. Comput. Phys. 327*, 389–415.

Aref, H. and S. Balachandar (1986). Chaotic advection in a Stokes flow. *Phys. Fluids 29*, 3515–3521.

Aslani, M. and J. D. Regele (2018). A localized artificial diffusivity method to simulate compressible multiphase flows using the stiffened gas equation of state. *Int. J. Numer. Meth. Fluids 88*(9), 413–433.

Aulisa, E., S. Manservisi, R. Scardovelli, and S. Zaleski (2007). Interface reconstruction with least-squares fit and split advection in three-dimensional cartesian geometry. *J. Comput. Phys. 225*, 2301–2319.

Basaran, O. A. (1992). Nonlinear oscillations of viscous liquid drops. *J. Fluid Mech. 241*, 169–198.

Basaran, O. A., H. Gao, and P. P. Bhat (2013). Nonstandard inkjets. *Annu. Rev. Fluid Mech. 45*, 85–113.

Beale, J. C. and R. D. Reitz (1999). Modeling spray atomization with the Kelvin-Helmholtz/Rayleigh-Taylor hybrid model. *Atomization Spray 9*, 623–650.

Becker, E., W. J. Hiller, and T. A. Kowalewski (1991). Experimental and theoretical investigation of large-amplitude oscillations of liquid droplets. *J. Fluid Mech. 231*, 189–210.

Becker, E., W. J. Hiller, and T. A. Kowalewski (1994). Nonlinear dynamics of viscous droplets. *J. Fluid Mech. 258*, 191–216.

Befrui, B., A. Aye, A. Bossi, L. E. Markle, and D. L. Varble (2016). Ecn gdi spray g: Coupled les jet primary breakup-lagrangian spray simulation and comparison with data. In *ILASS Americas 28th Annual Conference*.

Behzad, M., N. Ashgriz, and B. W. Karney (2016). Surface breakup of a non-turbulent liquid jet injected into a high pressure gaseous crossflow. *Int. J. Multiphase Flow 80*, 100–117.

Bell, J. B., P. Colella, and H. M. Glaz (1989). A second-order projection method for the incompressible Navier-Stokes equations. *J. Comput. Phys. 85*, 257–283.

Bergeles, K., Y. Hardalupas, and A. M. K. P. Taylor (2018). On the transient flow inside and around a deforming millimetre class oil droplet falling under the action of gravity in stagnant air. *Phys. Fluids 30*, 013305.

Bo, W., X. Liu, J. Glimm, and X. Li (2011). A robust front tracking method: verification and application to simulation of the primary breakup of a liquid jet. *SIAM J. Sci. Comput. 33*, 1505–1524.

Boeck, T. and S. Zaleski (2005). Viscous versus inviscid instability of two-phase mixing layers with continuous velocity profile. *Phys. Fluids 17*, 032106.

Borthakur, M. P., G. Biswas, and D. Bandyopadhyay (2017). Formation of liquid drops at an orifice and dynamics of pinch-off in liquid jets. *Phys. Rev. E 96*, 013115.

Castrejón-Pita, J. R., A. A. Castrejón-Pita, E. J. Hinch, J. R. Lister, and I. M. Hutchings (2012). Self-similar breakup of near-inviscid liquids. *Phys. Rev. E 86*, 015301.

Castrejón-Pita, J. R., A. A. Castrejón-Pita, S. S. Thete, K. Sambath, I. M. Hutchings, J. Hinch, J. R. Lister, and O. A. Basaran (2015). Plethora of transitions during breakup of liquid filaments. *Proc. Natl. Acad. Sci. U.S.A. 112*, 4582–4587.

Chakraborty, P., S. Balachandar, and R. J. Adrian (2005). On the relationships between local vortex identification schemes. *J. Fluid Mech. 535*, 189–214.

Chauhan, A., C. Maldarelli, D. T. Papageorgiou, and D. S. Rumschitzki (2006). The absolute instability of an inviscid compound jet. *J. Fluid Mech. 549*, 81.

Chen, A. U., P. K. Notz, and O. A. Basaran (2002). Computational and experimental analysis of pinch-off and scaling. *Phys. Rev. Lett. 88*, 174501.

Chung, S. K. and E. H. Trinh (2000). Internal flow of an electrostatically levitated droplet undergoing resonant shape oscillation. *Phys. Fluids 12*, 249–251.

Clanet, C. and J. C. Lasheras (1999). Transition from dripping to jetting. *J. Fluid Mech. 383*, 307–326.

Coralic, V. and T. Colonius (2014). Finite-volume weno scheme for viscous compressible multicomponent flows. *J. Comput. Phys. 274*, 95–121.

Corot, T., P. Hoch, and E. Labourasse (2020). Surface tension for compressible fluids in ale framework. *J. Comput. Phys.*, 109247.

Coullet, P., L. Mahadevan, and C. S. Riera (2005). Hydrodynamical models for the chaotic dripping faucet. *J. Fluid Mech. 526*, 1–17.

Day, R. F., E. J. Hinch, and J. R. Lister (1998). Self-similar capillary pinchoff of an inviscid fluid. *Phys. Rev. Lett. 80*, 704.

Deka, H., B. Ray, G. Biswas, A. Dalal, P.-H. Tsai, and A.-B. Wang (2017). The regime of large bubble entrapment during a single drop impact on a liquid pool. *Phys. Fluids 29*, 092101.

Desjardins, O. and H. Pitsch (2010). Detailed numerical investigation of turbulent atomization of liquid jets. *Atomization Spray 20*, 311—336.

Di-Ilio, G., V. K. Krastev, and G. Falcucci (2019). Evaluation of a scale-resolving methodology for the multidimensional simulation of GDI sprays. *Energies 12*, 2699.

Doshi, P., I. Cohen, W. W. Zhang, M. Siegel, P. Howell, O. A. Basaran, and S. R. Nagel (2003). Persistence of memory in drop breakup: The breakdown of universality. *Science 302*, 1185–1188.

Duke, D. J., A. L. Kastengren, K. E. Matusik, A. B. Swantek, C. F. Powell, R. Payri, D. Vaquerizo, L. Itani, G. Bruneaux, and R. O. Grover Jr (2017). Internal and near nozzle measurements of engine combustion network "Spray G" gasoline direct injectors. *Exp. Therm Fluid Sci. 88*, 608–621.

Dukowicz, J. K. (1980). A particle-fluid numerical model for liquid sprays. *J. Comput. Phys. 35*, 229–253.

Duret, B., J. Reveillon, T. Menard, and F. X. Demoulin (2013). Improving primary atomization modeling through DNS of two-phase flows. *Int. J. Multiphase Flow 55*, 130–137.

Eggers, J. (1993). Universal pinching of 3D axisymmetric free-surface flow. *Phys. Rev. Lett. 71*, 3458.

Eggers, J. and T. F. Dupont (1994). Drop formation in a one-dimensional approximation of the navier–stokes equation. *J. Fluid Mech. 262*, 205–221.

Ern, P., F. Risso, D. Fabre, and J. Magnaudet (2012). Wake-induced oscillatory paths of bodies freely rising or falling in fluids. *Annu. Rev. Fluid Mech. 44*, 97–121.

Feng, J. Q. (2010). A deformable liquid drop falling through a quiescent gas at terminal velocity. *J. Fluid Mech. 658*, 438–462.

Feng, J. Q. and K. V. Beard (1991). A perturbation model of raindrop oscillation characteristics with aerodynamic effects. *J. Atmospheric Sci. 48*, 1856–1868.

Francois, M. M., S. J. Cummins, E. D. Dendy, D. B. Kothe, J. M. Sicilian, and M. W. Williams (2006). A balanced-force algorithm for continuous and sharp interfacial surface tension models within a volume tracking framework. *J. Comput. Phys. 213*, 141–173.

Fuster, D., T. Arrufat, M. Crialesi-Esposito, Y. Ling, L. Malan, S. Pal, R. Scardovelli, G. Tryggvason, and S. Zaleski (2018). A momentum-conserving, consistent, volume-of-fluid method for incompressible flow on staggered grids. *arXiv:1811.12327*.

Fuster, D., A. Bagué, T. Boeck, L. Le Moyne, A. Leboissetier, S. Popinet, P. Ray, R. Scardovelli, and S. Zaleski (2009). Simulation of primary atomization with an octree adaptive mesh refinement and VOF method. *Int. J. Multiphase Flow 35*, 550–565.

Fuster, D., J. P. Matas, S. Marty, S. Popinet, H. J., A. Cartellier, and S. Zaleski (2013). Instability regimes in the primary breakup region of planar coflowing sheets. *J. Fluid Mech 736*, 150–176.

Fuster, D. and S. Popinet (2019). An all-mach method for the simulation of bubble dynamics problems in the presence of surface tension. under review by J. Comput. Phys.

Ganesan, S., G. Matthies, and L. Tobiska (2007). On spurious velocities in incompressible flow problems with interfaces. *Comput. Methods Appl. Mech. Eng. 196*, 1193–1202.

Garrick, D. P., W. A. Hagen, and J. D. Regele (2017). An interface capturing scheme for modeling atomization in compressible flows. *J. Comput. Phys. 344*, 260–280.

Garrick, D. P., M. Owkes, and J. D. Regele (2017). A finite-volume hllc-based scheme for compressible interfacial flows with surface tension. *J. Comput. Phys. 339*, 46–67.

Godunov, S. K. (1959). A difference method for numerical calculation of discontinuous solutions of the equations of hydrodynamics. *Mat. Sb. 89*(3), 271–306.

Gorokhovski, M. and M. Herrmann (2008). Modeling primary atomization. *Annu. Rev. Fluid Mech. 40*, 343–366.

Gueyffier, D., J. Li, A. Nadim, R. Scardovelli, and S. Zaleski (1999). Volume-of-fluid interface tracking with smoothed surface stress methods for three-dimensional flows. *J. Comput. Phys. 152*, 423–456.

Guildenbecher, D. R., C. López-Rivera, and P. E. Sojka (2009). Secondary atomization. *Exp. Fluids 46*, 371.

Gunn, D. J. (1978). Transfer of heat or mass to particles in fixed and fluidised beds. *Int. J. Heat Mass Transfer 21*(4), 467–476.

Gunn, R. and G. D. Kinzer (1949). The terminal velocity of fall for water droplets in stagnant air. *J. Meteorol. 6*, 243–248.

Haas, J. F. and B. Sturtevant (1987). Interaction of weak shock waves with cylindrical and spherical gas inhomogeneities. *J. Fluid Mech. 181*, 41–76.

Harten, A. and P. D. Lax (1981). A random choice finite difference scheme for hyperbolic conservation laws. *SIAM J. Numer. Anal. 18*(2), 289–315.

Hasslberger, J., S. Ketterl, M. Klein, and N. Chakraborty (2019). Flow topologies in primary atomization of liquid jets: a direct numerical simulation analysis. *J. Fluid Mech. 859*, 819–838.

Heindel, T. (2018). X-ray imaging techniques to quantify spray characteristics in the near field. *Atomization Sprays 28*(11).

Helenbrook, B. T. and C. F. Edwards (2002). Quasi-steady deformation and drag of uncontaminated liquid drops. *Int. J. Multiphase Flow 28*, 1631–1657.

Hill, M. J. M. (1894). On a spherical vortex. *Phil. Trans. R. Soc. A 185*, 213–245.

Hirt, C. W. and B. D. Nichols (1981). Volume of fluid (vof) method for the dynamics of free boundaries. *J. Comput. Phys. 39*(1), 201–225.

Hoepffner, J. and G. Paré (2013). Recoil of a liquid filament: escape from pinch-off through creation of a vortex ring. *J. Fluid Mech. 734*, 183–197.

Hoyas, S., A. Gil, X. Margot, D. Khuong-Anh, and F. Ravet (2013). Evaluation of the eulerian–lagrangian spray atomization (elsa) model in spray simulations: 2d cases. *Math. Comput. Model. 57*, 1686–1693.

Hoyt, J. W. and J. J. Taylor (1977). Waves on water jets. *J. Fluid Mech. 83*, 119–127.

Hu, H. H., N. A. Patankar, and M. Y. Zhu (2001). Direct numerical simulations of fluid-solid systems using the arbitrary Lagrangian-Eulerian technique. *J. Comput. Phys. 169*, 427–462.

Hysing, S.-R., S. Turek, D. Kuzmin, N. Parolini, E. Burman, S. Ganesan, and L. Tobiska (2009). Quantitative benchmark computations of two-dimensional bubble dynamics. *Int. J. Numer. Meth. Fluids 60*, 1259–1288.

Igra, D. and K. Takayama (2001). Numerical simulation of shock wave interaction with a water column. *Shock Waves 11*(3), 219–228.

Jarrahbashi, D. and W. A. Sirignano (2014). Vorticity dynamics for transient high-pressure liquid injection a. *Phys. Fluids 26*, 73.

Jarrahbashi, D., W. A. Sirignano, P. P. Popov, and F. Hussain (2016). Early spray development at high gas density: hole, ligament and bridge formations. *J. Fluid Mech. 792*, 186–231.

Jeong, J. and F. Hussain (1995). On the identification of a vortex. *J. Fluid Mech. 285*, 69–94.

Jiang, D. and Y. Ling (2019). Destabilization of a planar liquid stream by a co-flowing turbulent gas stream. *Int. J. Multiphase Flow 122*, 103121.

John, V. and G. Matthies (2004). MooNMD–a program package based on mapped finite element methods. *Search Results Featured snippet from the web Comput. Visual. Sci. 6*, 163–170.

Johnsen, E. and T. Colonius (2006). Implementation of WENO schemes in compressible multicomponent flow problems. *J. Comput. Phys. 219*, 715–732.

Josserand, C., P. Ray, and S. Zaleski (2016). Droplet impact on a thin liquid film: anatomy of the splash. *J. Fluid Mech. 802*, 775–805.

Keshavarz, B., E. C. Houze, . R. Moore, M. R. Koerner, and G. H. McKinley (2016). Ligament mediated fragmentation of viscoelastic liquids. *Phys. Rev. Lett. 117*, 154502.

Khan, M. M., J. Helie, M. Gorokhovski, and N. A. Sheikh (2017). Air entrainment in high pressure multihole gasoline direct injection sprays. *J. Appl. Fluid Mech. 10*, 1223–1234.

Kurganov, A. and D. Levy (2002). Central-upwind schemes for the saint-venant system. *ESAIM Math. Model. Numer. Anal. 36*, 397–425.

Kurganov, A., S. Noelle, and G. Petrova (2001). Semidiscrete central-upwind schemes for hyperbolic conservation laws and hamilton–jacobi equations. *SIAM J. Sci. Comput. 23*, 707–740.

Kurganov, A. and E. Tadmor (2000). New high-resolution central schemes for nonlinear conservation laws and convection–diffusion equations. *J. Comput. Phys. 160*, 241–282.

Lafaurie, B., C. Nardone, R. Scardovelli, S. Zaleski, and G. Zanetti (1994). Modelling merging and fragmentation in multiphase flows with SURFER. *J. Comput. Phys. 113*, 134–147.

Lakehal, D., M. Labois, and C. Narayanan (2012). Advances in the Large-Eddy and interface simulation (LEIS) of interfacial multiphase flows in pipes. *Prog. Comput. Fluid Dyn. 12*, 153–163.

Lalanne, B., S. Tanguy, and F. Risso (2013). Effect of rising motion on the damped shape oscillations of drops and bubbles. *Phys. Fluids 25*, 112107.

Lamb, H. (1932). *Hydrodynamics*. Cambridge University Press.

Lasheras, J. C. and E. J. Hopfinger (2000). Liquid jet instability and atomization in a coaxial gas stream. *Annu. Rev. Fluid Mech. 32*, 275–308.

Lasheras, J. C., E. Villermaux, and E. J. Hopfinger (1998). Break-up and atomization of a round water jet by a high-speed annular air jet. *J. Fluid Mech. 357*, 351–379.

Lebas, R., T. Menard, P. A. Beau, A. Berlemont, and F.-X. Demoulin (2009). Numerical simulation of primary break-up and atomization: DNS and modelling study. *Int. J. Multiphase Flow 35*, 247–260.

Leclaire, S., M. Reggio, and J. Trépanier (2013). Progress and investigation on lattice boltzmann modeling of multiple immiscible fluids or components with variable density and viscosity ratios. *J. Comput. Phys. 246*, 318–342.

Lee, T. and L. Liu (2010). Lattice boltzmann simulations of micron-scale drop impact on dry surfaces. *J. Comput. Phys. 229*(20), 8045–8063.

Lefebvre, A. H. (1980). Airblast atomization. *Prog. Energ. Combust. Sci. 6*, 233–261.

Lefebvre, A. H. and V. G. McDonell (2017). *Atomization and sprays*. CRC press.

Leib, S. J. and M. E. Goldstein (1986). Convective and absolute instability of a viscous liquid jet. *Phys. Fluids 29*(4), 952–954.

LeVeque, R. J. (2002). *Finite volume methods for hyperbolic problems*, Volume 31. Cambridge University Press.

Li, C., C. Li, F. Xiao, Q. Li, and Y. Zhu (2019). Experimental study of spray characteristics of liquid jets in supersonic crossflow. *Aerosp. Sci. Technol. 95*, 105426.

Li, P., Z. Wang, M. Sun, and H. Wang (2017). Numerical simulation of the gas-liquid interaction of a liquid jet in supersonic crossflow. *Acta Astronaut. 134*, 333–344.

Li, X. and M. C. Soteriou (2016). High fidelity simulation and analysis of liquid jet atomization in a gaseous crossflow at intermediate weber numbers. *Phys. Fluids 28*, 082101.

Lin, S. P. (2003). *Breakup of liquid sheets and jets*. Cambridge press.

Lin, S. P. and R. D. Reitz (1998). Drop and spray formation from a liquid jet. *Annu. Rev. Fluid Mech. 30*, 85–105.

Ling, Y., S. Balachandar, and M. Parmar (2016). Inter-phase heat transfer and energy coupling in turbulent dispersed multiphase flows. *Phys. Fluids 28*, 033304.

Ling, Y., J.-M. Fullana, S. Popinet, and C. Josserand (2016). Droplet migration in a Hele–Shaw cell: Effect of the lubrication film on the droplet dynamics. *Phys. Fluids 28*, 062001.

Ling, Y., D. Fuster, G. Tryggvasson, and S. Zaleski (2019). A two-phase mixing layer between parallel gas and liquid streams: multiphase turbulence statistics and influence of interfacial instability. *J. Fluid Mech. 859*, 268–307.

Ling, Y., D. Fuster, S. Zaleski, and G. Tryggvason (2017). Spray formation in a quasi-planar gas-liquid mixing layer at moderate density ratios: A numerical closeup. *Phys. Rev. Fluids 2*, 014005.

Liu, H., A. J. Valocchi, Y. Zhang, and Q. Kang (2014). Lattice boltzmann phase-field modeling of thermocapillary flows in a confined microchannel. *J. Comput. Phys. 256*, 334–356.

Liu, X., S. Osher, and T. Chan (1994). Weighted essentially non-oscillatory schemes. *J. Comput. Phys. 115*(1), 200–212.

López-Herrera, J., A. Gañán-Calvo, S. Popinet, and M. Herrada (2015). Electrokinetic effects in the breakup of electrified jets: A volume-of-fluid numerical study. *Int. J. Multiphase Flow 71*, 14–22.

Luo, H., J. D. Baum, and R. Löhner (2004). On the computation of multi-material flows using ale formulation. *J. Comput. Phys. 194*(1), 304–328.

Marmottant, P. and E. Villermaux (2004). On spray formation. *J. Fluid Mech. 498*, 73–111.

Marsh, S. P. (1980). *LASL shock Hugoniot data*, Volume 5. University of California Press.

Maxey, M. R. and J. J. Riley (1983). Equation of motion for a small rigid sphere in a nonuniform flow. *Phys. Fluids 26*, 883–889.

Ménard, T., S. Tanguy, and A. Berlemont (2007). Coupling level set/VOF/ghost fluid methods: Validation and application to 3D simulation of the primary break-up of a liquid jet. *Int. J. Multiphase Flow 33*, 510–524.

Meng, J. C. and T. Colonius (2015). Numerical simulations of the early stages of high-speed droplet breakup. *Shock Waves 25*, 399–414.

Meng, J. C. and T. Colonius (2018). Numerical simulation of the aerobreakup of a water droplet. *J. Fluid Mech. 835*, 1108–1135.

Michaelides, E. E. and Z. Feng (1994). Heat transfer from a rigid sphere in a nonuniform flow and temperature field. *Int. J. Heat Mass Transfer 37*, 2069–2076.

Miller, C. A. and L. E. Scriven (1968). The oscillations of a fluid droplet immersed in another fluid. *J. Fluid Mech. 32*, 417–435.

Mitroglou, N., J. M. Nouri, M. Gavaises, and C. Arcoumanis (2006). Spray characteristics of a multi-hole injector for direct-injection gasoline engines. *Int. J. Engine Res. 7*(3), 255–270.

Natarajan, R. and R. A. Brown (1987). Third-order resonance effects and the nonlinear stability of drop oscillations. *J. Fluid Mech. 183*, 95–121.

Navarro-Martinez, S., G. Tretola, M. R. Yosri, R. L. Gordon, and K. Vogiatzaki (2020). An investigation on the impact of small-scale models in gasoline direct injection sprays (ECN Spray G). *Int. J. Engine Res. 21*, 217–225.

Osher, S. and R. P. Fedkiw (2001). Level set methods: an overview and some recent results. *J. Comput. Phys. 169*, 463–502.

Osher, S. and J. A. Sethian (1988). Fronts propagating with curvature-dependent speed: algorithms based on hamilton-jacobi formulations. *J. Comput. Phys. 79*(1), 12–49.

Otto, T., M. Rossi, and T. Boeck (2013). Viscous instability of a sheared liquid-gas interface: Dependence on fluid properties and basic velocity profile. *Phys. Fluids 25*, 032103.

Padday, J. F. and A. R. Pitt (1973). The stability of axisymmetric menisci. *Phil. Trans. R. Soc. A 275*, 489–528.

Papageorgiou, D. T. (1995). On the breakup of viscous liquid threads. *Phys. Fluids 7*, 1529–1544.

Paredi, D., T. Lucchini, G. D'Errico, A. Onorati, L. Pickett, and J. Lacey. *Int. J. Engine Res.* (1), 199–216.

Payri, R., J. Gimeno, P. Marti-Aldaravi, and D. Vaquerizo (2016). Internal flow characterization on an ecn gdi injector. *Atomization Spray 26*, 889–919.

Payri, R., F. J. Salvador, P. Marti-Aldaravi, and D. Vaquerizo (2017). ECN Spray G external spray visualization and spray collapse description through penetration and morphology analysis. *Appl. Therm. Eng. 112*, 304–316.

Piazzullo, D., M. Costa, L. Allocca, A. Montanaro, and V. Rocco (2018). Schlieren and Mie scattering techniques for the ECN "spray G" characterization and 3d cfd model validation. *Int. J. Numer. Methods Heat Fluid Flow 28*, 498–515.

Pope, S. B. (2000). *Turbulent flows*. Cambridge Univ Press.

Popinet, S. The basilisk code. Available from http://basilisk.fr/.

Popinet, S. (2003). Gerris: a tree-based adaptive solver for the incompressible euler equations in complex geometries. *J. Comput. Phys. 190*, 572–600.

Popinet, S. (2009). An accurate adaptive solver for surface-tension-driven interfacial flows. *J. Comput. Phys. 228*(16), 5838–5866.

Popinet, S. (2018). Numerical models of surface tension. *Annu. Rev. Fluid Mech. 50*, 1–28.

Prosperetti, A. (1980). Normal-mode analysis for the oscillations of a viscous-liquid drop in an immiscible liquid. *J. Mec. 19*, 149–182.

Quirk, J. J. and S. Karni (1996). On the dynamics of a shock-bubble interaction. *J. Fluid Mech. 318*, 129–163.

Rangel, R. H. and W. A. Sirignano (1988). Nonlinear growth of Kelvin–Helmholtz instability: effect of surface tension and density ratio. *Phys. Fluids 31*, 1845–1855.

Rayleigh, L. (1879). On the capillary phenomena of jets. *Proc. R. Soc. Lond. 29*, 71–97.

Reed, H. L., W. S. Saric, and D. Arnal (1996). Linear stability theory applied to boundary layers. *Annu. Rev. Fluid Mech. 28*(1), 389–428.

Reid, W. H. (1960). The oscillations of a viscous liquid drop. *Q. Appl. Maths 18*, 86–89.

Reitz, R. D. and F. V. Bracco (1982). Mechanism of atomization of a liquid jet. *Phys. Fluids 25*, 1730–1742.

Roe, P. L. (1981). Approximate Riemann solver, parameter vectors, and difference schemes. *J. Comput. Phys. 43*, 357–372.

Sallam, K. A., C. Aalburg, and G. M. Faeth (2004). Breakup of round nonturbulent liquid jets in gaseous crossflow. *AIAA J. 42*, 2529–2540.

Scardovelli, R. and S. Zaleski (1999). Direct numerical simulation of free-surface and interfacial flow. *Annu. Rev. Fluid Mech. 31*, 567–603.

Scardovelli, R. and S. Zaleski (2000). Analytical relations connecting linear interfaces and volume fractions in rectangular grids. *J. Comput. Phys. 164*(1), 228–237.

Schetz, J. A., E. A. Kush Jr, and P. B. Joshi (1980). Wave phenomena in liquid jet breakup in a supersonic crossflow. *AIAA J. 18*(7), 774–778.

Schmidmayer, K., F. Petitpas, E. Daniel, N. Favrie, and S. Gavrilyuk (2017). A model and numerical method for compressible flows with capillary effects. *J. Comput. Phys. 334*, 468–496.

Schulkes, R. M. S. M. (1994). The evolution and bifurcation of a pendant drop. *J. Fluid Mech. 278*, 83–100.

Sethian, J. A. and P. Smereka (2003). Level set methods for fluid interfaces. *Annu. Rev. Fluid Mech. 35*(1), 341–372.

Shao, C., K. Luo, Y. Yang, and J. Fan (2017). Detailed numerical simulation of swirling primary atomization using a mass conservative level set method. *Int. J. Multiphase Flow 89*, 57–68.

Shinjo, J. and A. Umemura (2010). Simulation of liquid jet primary breakup: Dynamics of ligament and droplet formation. *Int. J. Multiphase Flow 36*, 513–532.

Shyue, K. (1998). An efficient shock-capturing algorithm for compressible multicomponent problems. *J. Comput. Phys. 142*(1), 208–242.

Sod, G. A. (1978). A survey of several finite difference methods for systems of nonlinear hyperbolic conservation laws. *J. Comput. Phys. 27*(1), 1–31.

Sotolongo-Costa, O., Y. Moreno-Vega, J. J. Lloveras-González, and J. C. Antoranz (1996). Criticality in droplet fragmentation. *Phys. Rev. Lett.*, 42–45.

Sparacino, S., F. Berni, A. d'Adamo, V. K. Krastev, A. Cavicchi, and L. Postrioti (2019). Impact of the primary break-up strategy on the morphology of GDI sprays in 3D-CFD simulations of multi-hole injectors. *Energies 12*, 2890.

Sphicas, P., L. M. Pickett, S. Skeen, J. Frank, T. Lucchini, D. Sinoir, G. D'Errico, K. Saha, and S. Som (2017). A comparison of experimental and modeled velocity in gasoline direct-injection sprays with plume interaction and collapse. *SAE Int. J. Fuels Lubr. 10*, 184–201.

Sphicas, P., L. M. Pickett, S. A. Skeen, and J. H. Frank (2018). Inter-plume aerodynamics for gasoline spray collapse. *Int. J. Engine Res. 19*(10), 1048–1067.

Squire, H. B. (1953). Investigation of the instability of a moving liquid film. *Br. J. Appl. Phys. 4*(6), 167.

Staat, H. J. J., A. van der Bos, M. van den Berg, H. Reinten, H. Wijshoff, M. Versluis, and D. Lohse (2017). Ultrafast imaging method to measure surface tension and viscosity of inkjet-printed droplets in flight. *Exp. Fluids 58*(1), 2.

Sumesh, P. T. and R. Govindarajan (2010). The possible equilibrium shapes of static pendant drops. *J. Chem. Phys. 133*, 144707.

Terashima, H. and G. Tryggvason (2009). A front-tracking/ghost-fluid method for fluid interfaces in compressible flows. *J. Comput. Phys. 228*(11), 4012–4037.

Theofanous, T. G., V. V. Mitkin, C. L. Ng, C. H. Chang, X. Deng, and S. Sushchikh (2012). The physics of aerobreakup. ii. viscous liquids. *Phys. Fluids 24*, 022104.

Toro, E. F. (2001). *Shock-capturing methods for free-surface shallow flows*. John Wiley.

Toro, E. F., M. Spruce, and W. Speares (1994). Restoration of the contact surface in the hll-riemann solver. *Shock Waves 4*(1), 25–34.

Tripathi, M. K., K. C. Sahu, and R. Govindarajan (2014). Why a falling drop does not in general behave like a rising bubble. *Sci. Rep. 4*, 4771.

Tryggvason, G., B. Bunner, A. Esmaeeli, D. Juric, N. Al-Rawahi, W. Tauber, J. Han, S. Nas, and Y. J. Jan (2001). A front-tracking method for the computations of multiphase flow. *J. Comput. Phys. 169*, 708–759.

Tryggvason, G., R. Scardovelli, and S. Zaleski (2011). *Direct numerical simulations of gas-liquid multiphase flows*. Cambridge University Press.

Tsamopoulos, J. A. and R. A. Brown (1983). Nonlinear oscillations of inviscid drops and bubbles. *J. Fluid Mech. 127*, 519–537.

Umemura, A. (2014). Model for the initiation of atomization in a high-speed laminar liquid jet. *J. Fluid Mech. 757*, 665700.

Unverdi, S. O. and G. Tryggvason (1992). A front-tracking method for viscous, incompressible, multi-fluid flows. *J. Comput. Phys. 100*(1), 25–37.

Vallet, A. and R. Borghi (1999). An Eulerian model of atomization of a liquid jet. *C. R. Acad. Sci. Paris, série II b 327*, 1015–1020.

van der Bos, A., M.-J. van der Meulen, T. Driessen, M. van den Berg, H. Reinten, H. Wijshoff, M. Versluis, and D. Lohse (2014). Velocity profile inside piezoacoustic inkjet droplets in flight: comparison between experiment and numerical simulation. *Phys. Rev. Appl. 1*, 014004.

van Hooft, J. A., S. Popinet, C. C. van Heerwaarden, S. J. A. van der Linden, S. R. de Roode, and B. J. H. van de Wiel (2018). Towards adaptive grids for atmospheric boundary-layer simulations. *Bound.-Layer Meteor. 167*, 421–443.

Vaudor, G., T. Ménard, W. Aniszewski, M. Doring, and A. Berlemont (2017). A consistent mass and momentum flux computation method for two phase flows. application to atomization process. *Comput. Fluids 152*, 204–216.

Villermaux, E., P. Marmottant, and J. Duplat (2004). Ligament-mediated spray formation. *Phys. Rev. Lett. 92*, 074501.

Wang, Z., A. Swantek, R. Scarcelli, D. Duke, A. Kastengren, C. F. Powell, S. Som, R. Reese, K. Freeman, and Y. Zhu (2015). LES of diesel and gasoline sprays with validation against X-ray radiography data. *SAE Int. J. Fuels Lubr. 8*, 147–159.

Weymouth, G. D. and D. K.-P. Yue (2010). Conservative volume-of-fluid method for free-surface simulations on cartesian-grids. *J. Comput. Phys. 229*(8), 2853–2865.

Wilkes, E. D., S. D. Phillips, and O. A. Basaran (1999). Computational and experimental analysis of dynamics of drop formation. *Phys. Fluids 11*, 3577–3598.

Wu, L., Z.-g. Wang, Q. Li, and J. Zhang (2015). Investigations on the droplet distributions in the atomization of kerosene jets in supersonic crossflows. *Appl. Phys. Lett. 107*(10), 104103.

Xiao, F., Z. G. Wang, M. B. Sun, J. H. Liang, and N. Liu (2016). Large eddy simulation of liquid jet primary breakup in supersonic air crossflow. *Int. J. Multiphase Flow 87*, 229–240.

Yang, S., P. Yi, and C. Habchi (2020). Real-fluid injection modeling and les simulation of the ecn spray a injector using a fully compressible two-phase flow approach. *Int. J. Multiphase Flow 122*, 103145.

Yih, C.-S. (1967). Instability due to viscosity stratification. *J. Fluid Mech. 27*, 337–352.

Yue, Z., M. Battistoni, and S. Som (2020). Spray characterization for engine combustion network Spray G injector using high-fidelity simulation with detailed injector geometry. *Int. J. Engine Res. 21*, 226–238.

Zandian, A., W. A. Sirignano, and F. Hussain (2018). Understanding liquid-jet atomization cascades via vortex dynamics. *J. Fluid Mech. 843*, 293–354.

Zandian, A., W. A. Sirignano, and F. Hussain (2019). Vorticity dynamics in a spatially developing liquid jet inside a co-flowing gas. *J. Fluid Mech. 877*, 429–470.

Zeff, B. W., B. Kleber, J. Fineberg, and D. P. Lathrop (2000). Singularity dynamics in curvature collapse and jet eruption on a fluid surface. *Nature 403*, 401.

Zhang, B., Y. Ling, P. Tsai, A. Wang, S. Popinet, and S. Zaleski (2019). Short-term oscillation and falling dynamics for a water drop dripping in quiescent air. *Physical Review Fluids 4*(12), 123604.

Zhang, B., S. Popinet, and Y. Ling (2020). Modeling and detailed numerical simulation of the primary breakup of a gasoline surrogate jet under non-evaporative operating conditions. *Int. J. Multiphase Flow 130*, 103362.

Zhang, X. (1999a). Dynamics of drop formation in viscous flows. *Chem. Eng. Sci. 54*, 1759–1774.

Zhang, X. (1999b). Dynamics of growth and breakup of viscous pendant drops into air. *J. Colloid Interface Sci. 212*, 107–122.

Zhang, X. and O. A. Basaran (1995). An experimental study of dynamics of drop formation. *Phys. Fluids 7*, 1184–1203.

Zhao, F., M.-C. Lai, and D. L. Harrington (1999). Automotive spark-ignited direct-injection gasoline engines. *Prog. Energ. Combust. Sci. 25*, 437–562.

Zhou, J., R. J. Adrian, B. S., and T. M. Kendall (1999). Mechanisms for generating coherent packets of hairpin vortices in channel flow. *J. Fluid Mech. 387*, 353–396.

Zhu, Y. H., F. Xiao, Q. L. Li, R. Mo, C. Li, and S. Lin (2019). Les of primary breakup of pulsed liquid jet in supersonic crossflow. *Acta Astronaut. 154*, 119–132.